Measurement of the $W^{\pm}$ Boson Cross Section in the Electron Decay Channel at $\sqrt{s} = 7$ TeV with the ATLAS Detector

Thesis submitted in accordance with the requirements of the University of Liverpool for the degree of Doctor in Philosophy

by

Bozydar Adam Wrona

The University of Liverpool
Department of Physics

January 2012

This thesis is the result of my own work. The material contained in the thesis has not been presented, nor is currently being presented, either wholly or in part for any other degree or other qualification. The research was carried out in the Department of Physics, Faculty of Science and Engineering, and at CERN, Geneva, Switzerland. All work presented was performed by the candidate.

Abstract

At the LHC, the process $pp \to W^{\pm}X$ followed by the leptonic decays $W^- \to e^-\bar{\nu}$ and $W^+ \to e^+\nu$ is investigated to test the Standard Model in a completely new kinematic range. This thesis describes $W^{\pm}$ cross-section measurements using pp collisions recorded by the ATLAS detector in 2010. The charge dependence is measured both integrated and differentially in lepton pseudorapidity η; and analysis of the systematic uncertainties is presented. The results are compared with a recent publication by ATLAS which uses different reconstruction and background estimations. The cross-sections are also compared with theoretical predictions based on recent PDF sets determined recently by the CTEQ, MSTW, ABKM, HERAPDF and JR groups. The values of the $W^{\pm}$ cross-sections and their respective uncertainties, for 35.1 pb^{-1} at 7 TeV centre of mass energy, determined by this analysis, are:

$$\sigma^{fid}_{W^+} \times \mathbf{BR}(W \to e^+\nu_e) = 2.907 \pm 0.015_{(stat.)} \pm 0.113_{(syst.)} \pm 0.099_{(lumi.)}\ [\mathbf{nb}]$$

$$\sigma^{fid}_{W^-} \times \mathbf{BR}(W \to e^-\bar{\nu}_e) = 1.913 \pm 0.012_{(stat.)} \pm 0.077_{(syst.)} \pm 0.065_{(lumi.)}\ [\mathbf{nb}]$$

Contents

Acknowledgements

I would like to begin by thanking my supervisor, Professor Max Klein, for his patience and advice over the years. The completion of the thesis would not have been possible without endless support from Dr Jan Kretzschmar. His expertise has guided me on numerous occasions. I would also like to thank the Science and Technology Facilities Council for their financial support throughout my studies, - as well as Professor Phil Allport, my secondary supervisor, who has led the Liverpool high energy physics group while I've been here.

Many people have made my time at Liverpool more productive and more enjoyable. There are too many to be listed. Therefore I would just name one, closest to my heart, my beloved Sylwia.

Thank you for giving birth to my lovely son Nathaniel Oliver (☆1.10.2010☆), for substituting me in parental responsibilities, for sharing the dreams and for providing financial support towards the end of my PhD. For all this and much, much, more. Thank you.

Finally to those who shared with me the joys of life, since the beginning, my Parents. Thank you for reminding me that

```
...we form just a simple set of very primitive tools...
```

Chapter 1

Introduction

The inexplicable belief in the possibility to unveil the nature of *Physis* has been the driving force behind our journey into the unknown, throughout the entire history of science. The remarkable precision of predictions derived, notably within the framework of particle physics, helped to prove the assumption as not being completely unmotivated. This was possible due to the amazing progress made in the development of the *Standard Model of Particle Physics* (SM) both in terms of theoretical apparatus and experimental discoveries. The new ideas developed in quantum field theories for the description of strong, weak and electromagnetic interactions created an elegant model, where the building blocks of nature are depicted as excitations of quantum fields, with three fundamental forces being mediated between twelve elementary particles. Among numerous successful predictions, - it is important to mention W and Z bosons discovered by the UA1 [1–3] and UA2 [4–6] experiments at $\sqrt{s} = 0.63$ TeV at the CERN $Sp\bar{p}S$ in 1982 and studied by the CDF [7–9] and D0 [10–12] experiments at $\sqrt{s} = 1.9$ TeV and $\sqrt{s} = 1.96$ TeV respectively, at the Fermilab Tevatron proton-antiproton colliders. However, despite the unquestionable success of the SM, the quest does not end here. The questions regarding the unification of forces above a certain energy threshold, the inclusion of gravity as a quantum field, an explanation for the observed hierarchy of particle' masses, possible candidates for dark matter and the discovery of the Higgs Boson, remain still open.

To provide an insight into shortcomings of the model, the world's most powerful particle accelerator, the Large Hadron Collider (LHC), was introduced, colliding two proton beams at the center-of-mass energy of $\sqrt{s} = 7$ TeV, with major particle detectors: ATLAS, CMS, LHCb and ALICE, situated at four collision points of the ring.

Since it is a natural prerequisite for any discovery, first to test the SM at the new energy frontier, therefore, due to a relatively high event rate and simple decay signatures W and Z production was one of the first milestones in the physics program for early LHC data. The theoretical calculations of the inclusive W and Z cross sections have been carried out at next-to-leading order (NLO) [13–15] and next-to-next-to-leading order ($NNLO$) [16–20] in perturbative Quantum Chromodynamics ($pQCD$), within a few percent uncertainty. Therefore, a precise measurement of these parameters provides a stringent test of the QCD calculations, and constrains on parametrization for the momentum distribution of the partons, the Parton Density Functions (PDFs). The LHC operates in the kinematic regime mostly not accessible by previous experiments, therefore the proton substructure is accessed experimentally in the new region, providing vital information on the proton initial states in pp collisions at $\sqrt{s} = 7$ TeV. Along with a better understanding of strong interactions and a correct description of the proton structure, also the detailed assessment of the detector performance is central for the accuracy of the measurements performed. These are both challenging from the experimental point of view, and crucial for the early analyses performed at the LHC.

The measurement of the inclusive W production cross section in the electron decay channel, presented in this thesis, was conducted according to the above strategy. The study constitutes a complementary cross-check for the ATLAS published result [21]. The data used for the analysis were collected by the ATLAS detector over a period of 2010 operation, and correspond to roughly 78% of the

total integrated luminosity.

Amid strong physics motivation for exploring channels with electrons in the final state and understanding how to detect the presence of neutrinos, $W \rightarrow e\nu_e$ differential cross section measurement as a function of lepton pseudorapidity proves to be a sensitive probe for the studies of proton structure, thus enhancing the discovery prospects of the LHC. Moreover being an important background to both the SM, e.g. $H \rightarrow W^+W^-$, and beyond the SM physics with large missing transverse energy signatures, the accurate measurement could provide direct feedback for potential discovery channels.

The thesis describes the methodology of the total and differential, inclusive W boson, cross section measurement in the electron channel, i.e. $pp \rightarrow W^{\pm}X$ with the decays $W^+ \rightarrow e^+\nu_e$ and $W^- \rightarrow e^-\bar{\nu}_e$. This study is conducted with an integrated luminosity of $35.1 \pm 1.2 pb^{-1}$ recorded during 2010 with the ATLAS detector at the LHC for a proton beam energy of $E_p = 3.5$ TeV.

The W production cross section measurement, presented in the thesis, is organized into chapters, where each of the constituents essential for the derivation of the final result is discussed separately. It begins with a theoretical outline of the physics relevant for the W boson production at the LHC (Chapter 2), where the *Drell-Yan* process phenomenology is briefly introduced along with the *Quark Parton Model* (QPM). Moreover the kinematic characteristics of the W boson events are detailed with predictions for the measurement cross section at the LHC. This is followed by a brief description of the ATLAS detector in Chapter 3 with the emphasis on the detector components most crucial for the cross section measurement, i.e the inner tracking detector and calorimeters. Chapter 4 presents the Monte Carlo event generators and the samples used in the analysis. Event reconstruction and selection strategy are presented in detail in Chapter 5. Moreover, the data driven method, central for the estimate of the measurement efficiencies is presented, with the example of electron trigger efficiency evalua-

tion. In Chapter 6 the main background contributions are discussed, including a method used to estimate the contribution from hadronic di-jet events directly from the data and several tests to validate it. Chapter 7 starts from the comparison between various distributions of selected W boson data events and respective Monte Carlo estimates. This is followed by the evaluation of the inclusive $W^{\pm}$ production cross sections times electron branching ratios, $\sigma_{W^{\pm}} \times BR(W \rightarrow e\nu_e)$. The cross section values are presented integrated over the fiducial region of the analysis, $\sigma^{fid}_{W^{\pm}}$, and extrapolated to the full kinematic range, $\sigma^{tot}_{W^{\pm}}$. The measurement is also reported differentially, as a function of electron pseudorapidity, η. Both integrated and differential, results are compared with most recent ATLAS result [21] and QCD predictions based on recent determinations of the parton distribution functions of the proton. Final chapters of the thesis are dedicated to systematic cross section uncertainties (see Chapter ??) and conclusion of the work (see Chapter 8).

Chapter 2

Drell-Yan Production of Vector Bosons

2.1 Introduction

[1] Drell-Yan (DY) scattering [23] is a suitable testing ground for perturbative Quantum Chromodynamics ($pQCD$) because it can be calculated to high orders in perturbative QCD [15, 17, 20], where up to next-to-next-to leading order ($NNLO$) has been achieved.

W boson production in the DY process (see Figure 2.1) is characterised by the energy scale of the hard scattering process, Q^2, which in DY scattering is determined by the mass squared of the W boson, and by the rapidity y_W of the boson. Q^2 is directly related to the sum of four momenta of W decay particles, therefore at LO :

$$Q^2 = (x_{q1} \cdot P + x_{q2} \cdot P)^2 = s x_{q1} x_{q2} = M_W^2 = (p_e + p_\nu)^2$$

where Bjorken x represents the fraction of proton momentum, P, carried by the interacting partons, i.e $x \epsilon (0, 1)$. The mass and rapidity fully determine x of the interacting quarks as:

$$x_{1,2} = M_W e^{\pm y_W} / \sqrt{s} \tag{2.1}$$

[1] The subsequent discussion of the DY phenomenology and its relation to PDFs follows the internal ATLAS note [22]

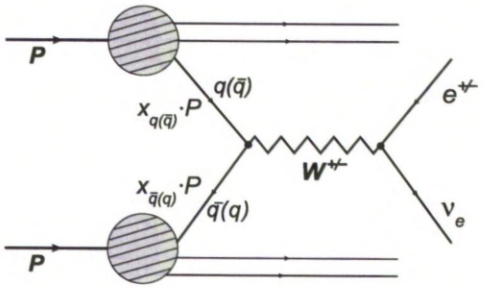

Figure 2.1: Drell-Yan production for $W^{\pm}$ boson in the electron decay channel.

where $s = 4E_p^2$ is the centre-of-momentum system (cms) energy squared. One may therefore represent the kinematic ranges of deep inelastic scattering experiments and DY measurements in a common $\{x, Q^2\}$ plot as is illustrated in Figure 2.2. The kinematic range of the W measurements from the Tevatron is extended towards lower x by the LHC due to the increase of beam energy.

The minimum rapidity y_W is observed for limiting case of $x = 1$ and equal to $y_W = -\ln(2E_p/M_W) = -4.47$ for $M_W = 80.42\,\text{GeV}$ and beam energy of 3.5 TeV. The center of the rapidity distribution, $y_W = 0$, corresponds to Bjorken x values of $x = M/2E_p = 0.011$, for W production.

The x range accessed, see Figure 2.2, is covered by the measurements of PDFs from H1 and ZEUS [24]. However the prediction of the W cross sections in the rapidity plateau region at the LHC requires an extrapolation of the PDF determinations based on $HERA$ by about two orders of magnitude in Q^2. Accurate LHC measurements of the charged current (CC) processes, $pp \to W^{+(-)}X \to e^{+(-)}\nu_e(\overline{\nu})X$, will thus primarily test the validity of the QCD evolution into the region of high Q^2 at small x. They may also be expected to provide constraints on the flavour contributions to the CC cross sections, as is discussed below.

Experimentally, the signatures of DY W boson production and leptonic decay are unique and thus permit a test and the development of measurement and calibration techniques of ATLAS. The corresponding event rates are sizable as is

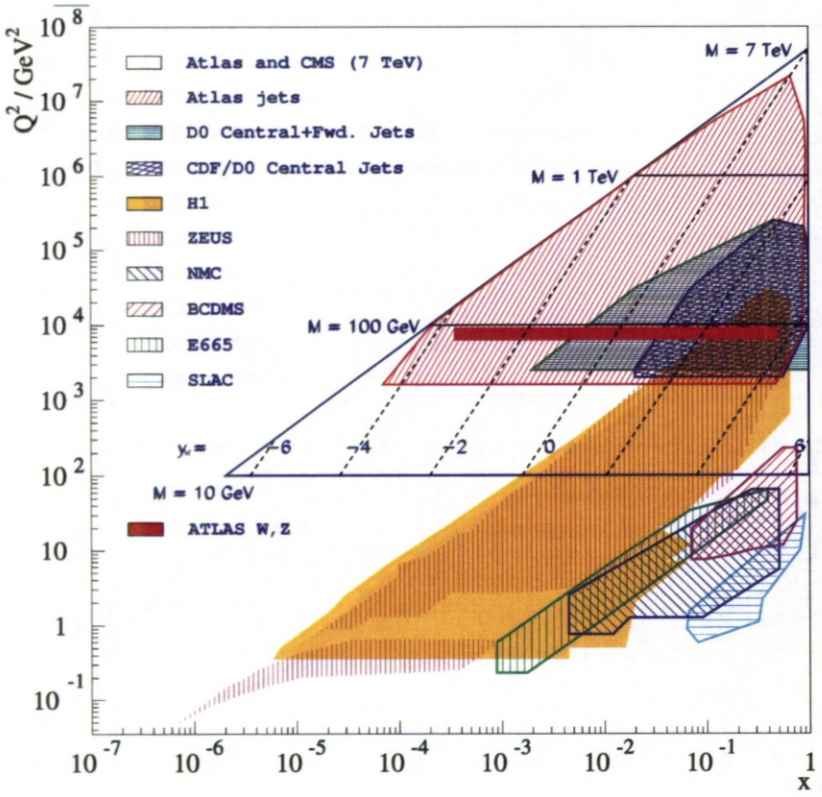

Figure 2.2: Kinematic plane of deep inelastic scattering (DIS), in $\{Q^2, x\}$, at HERA and for fixed target experiments and their equivalent in Drell-Yan scattering, in $\{M^2, y_W\}$, at the Tevatron and the LHC *(for 7 TeV=2E_p).*

illustrated in Figure 2.3. The W cross sections may be of some use also for monitoring the time development or eventually determining the absolute luminosity.

2.2 Drell-Yan Scattering in the Quark Parton Model

To leading order, the double differential Drell-Yan scattering cross section [15] for the charged current reaction, $pp \to W^{+(-)}X \to e^{+(-)}\nu_e(\overline{\nu})X$, can be written as

$$\frac{d^2\sigma}{dMdy_W} = \frac{4\pi\alpha^2(M)}{9} \cdot 2M \cdot P(M) \cdot \Phi(x_1, x_2, M^2) \ . \tag{2.2}$$

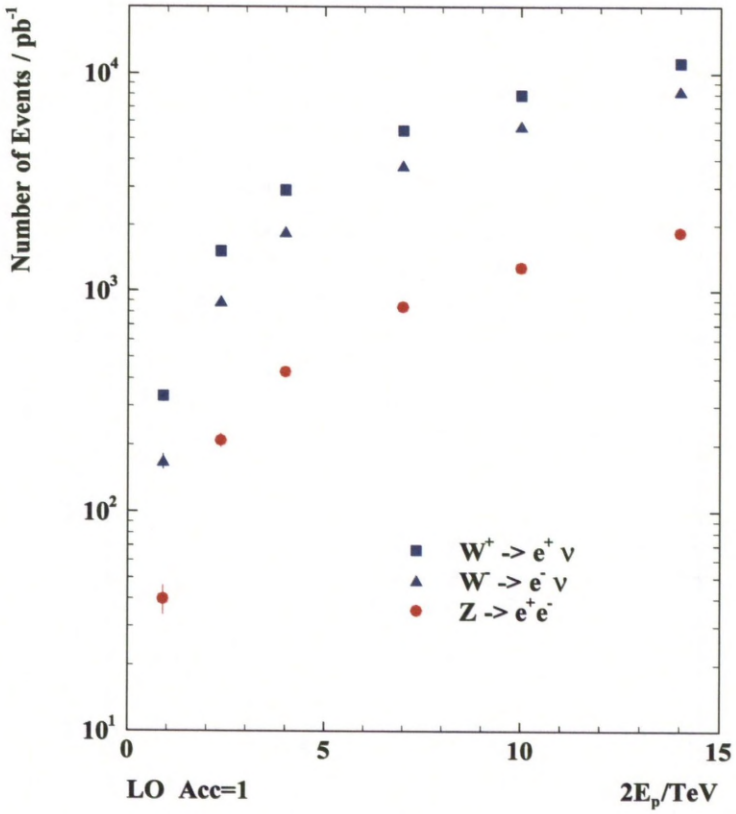

Figure 2.3: (from [22]) Number of events per pb^{-1} of integrated luminosity as a function of the cms energy $\sqrt{s} = 2E_p$, calculated using the H1PDF2009 parton distribution set [25] with the leading order (LO) formulae as quoted in the text and assuming full efficiency (Acc = 1) and a boson rapidity range of $|y_W| < 2.5$. Note that this dependence is essentially linear with $\sqrt{s}$. The first point corresponds to the LHC injection energy of 450 GeV, the second one to the maximum energy reached in December 2009 of $E_p = 1.18$ TeV. The number of events available for analysis may be smaller by a factor of about 4, depending on the electron reconstruction efficiency and further kinematic constraints. Higher order QCD terms enhance the cross section as compared to LO by about 20%.

Here M is the mass of the $e^+\nu$ and $e^-\bar{\nu}$ system and y_W is the boson rapidity, where the propagator term $P(M)$ is expressed as:

$$P_W = \frac{\kappa_W^2}{(M^2 - M_W^2)^2 + (\Gamma_W M_W)^2} \tag{2.3}$$

with $\kappa_W = 1/(4\sin^2\Theta)$ where Θ is the weak mixing angle, $\cos\Theta = \frac{M_W}{M_Z}$ (M_Z = 91.19 GeV is the Z boson mass).

The parton distribution term Φ is given by:

$$\Phi_{W^+} =$$

$$= x_1 x_2 [U_{ud}^2(u_1\bar{d}_2 + u_2\bar{d}_1) + U_{cs}^2(c_1\bar{s}_2 + c_2\bar{s}_1) + U_{us}^2(u_1\bar{s}_2 + u_2\bar{s}_1) + U_{cd}^2(c_1\bar{d}_2 + c_2\bar{d}_1)] \tag{2.4}$$

$$\Phi_{W^-} =$$

$$= x_1 x_2 [U_{ud}^2(\bar{u}_1 d_2 + \bar{u}_2 d_1) + U_{cs}^2(\bar{c}_1 s_2 + \bar{c}_2 s_1) + U_{us}^2(\bar{u}_1 s_2 + \bar{u}_2 s_1) + U_{cd}^2(\bar{c}_1 d_2 + \bar{c}_2 d_1)] \tag{2.5}$$

with $q_i = q_i(x, M^2)$. Here U_{ik} are the usual CKM matrix elements describing the mixing of quark flavour i with k such that the transitions in the same family are favored, $U_{ud} \simeq U_{cs} \simeq 0.97$, while transitions between different families are suppressed, $U_{us} \simeq U_{cd} \simeq 0.23$. Figure 2.4 shows the W production as a function of boson rapidity, y_W, decomposed into different flavour of partonic contributions, predicted from CTEQ6.6 [26] and HERAPDF1.0 [24] PDF sets.

In W production the boson rapidity is not directly accessible but may be approximated at large transverse momentum by the pseudo-rapidity η_e of the W decay electron, see below. The η_e distributions, integrated over M_W, which result from the expressions above are illustrated in Figure 2.5(b) using various sets of PDF parametrization and two different Monte Carlo generators PYTHIA [27] and MC@NLO [28–30]. Due to the higher probability of producing the up-quark than the down-quark (possibly apart from very low x) the W^+ cross section, being dominated by the $u\bar{d}$ contribution, is expected to exceed the W^- cross section,which is dominated by the $\bar{u}d$ part.

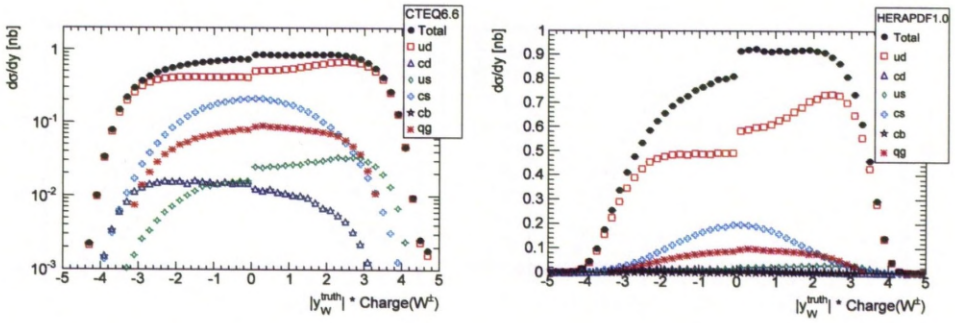

Figure 2.4: Parton decomposition of W^+ and W^- production as a function of boson rapidity, y_W, derived from NLO CTEQ6.6 *and* HERAPDF1.0 *PDF sets. Different sensitivity of W^+ compared to W^-can be traced back to flavour contributions. W boson production dominated by $u\bar{d} \to W^+$ and $\bar{u}d \to W^-$. Also visible beyond leading order $q(\bar{q})g$ production channels.*

2.3 Kinematic Variables

Figure 2.5 shows the expected kinematic distributions of the $W^{\pm}$ boson decaying into electron and neutrino, obtained from generated $q\bar{q} \to W \to e\nu_e$ events without considering the detector reconstruction effects. The predictions shown in Figure 2.5 are all normalised to the same total cross section value of $10.46\,nb$ obtained in $NNLO$ using the $MSTW08$ PDF [32]. The distributions are observed to then behave very similar in shape for the three PDFs and different MC generator programs used here. The visible difference in ratios of $Pythia/MC@NLO$ for both NLO PDFs used, is an early indication for the scale of the acceptance uncertainty, however no conclusion is possible at this stage since plotted kinematical distributions do not include the requirements for the fiducial acceptance of the final measurement. The assessment of the acceptance effects is discussed later in Chapter 7. Figure 2.5(a) shows the distribution for the electron pseudorapidity, η, which is defined by the polar angle θ of a particle relative to the beam axis of the ATLAS detector[2], $\eta = -\ln\tan(\theta/2)$. The electrons from $W^{\pm}$

[2] ATLAS uses a right-handed coordinate system with the origin at the nominal interaction point (IP) in the center of the detector and the Z-axis along the beam pipe. The horizontal x-axis points from the IP to the center of the LHC ring and y-axis vertically upwards. Cylindrical

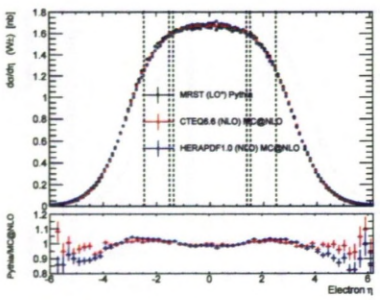

(a) η_e with fiducial regions

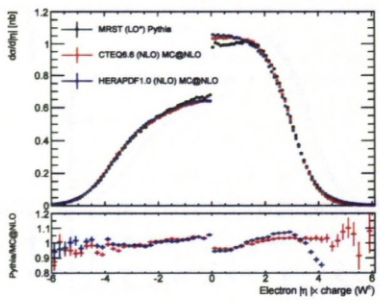

(b) $|\eta|_e$ differentiated in charge

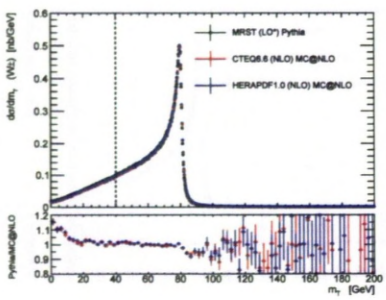

(c) m_{T} for $W^{\pm}$

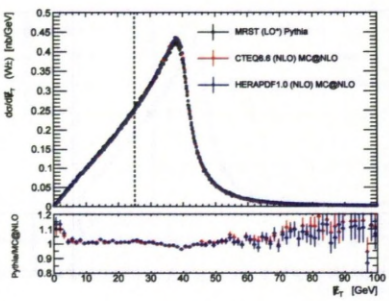

(d) generated $\not{E}_{\mathrm{T}}$ of a neutrino from $W^{\pm}$

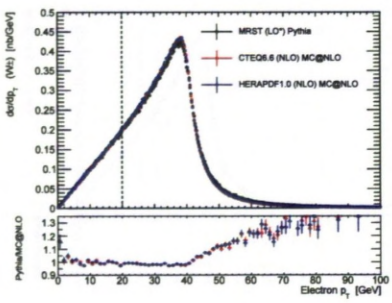

(e) E_{T} of an electron from $W^{\pm}$

Figure 2.5: Pure generator level distributions (i.e. no selection cuts applied) for measurement observables in $W \to e\nu_e$ channel, shown for PDFs from MRST (LO) [31] used by Pythia generator, together with CTEQ6.6 [26] (NLO) and HERAPDF1.0 [24] (NLO) both as inputs to MC@NLO. The ratios of Pythia/MC@NLO for both NLO PDFs are also shown. The vertical lines denote the acceptance limits for this analysis (fiducial regions). $W^{\pm}$ cross-section was normalized to MSTW08 value calculated at (NNLO), ($\sigma^{NNLO}_{W^{\pm}} = 10.46\,nb$).*

are produced abundantly in a spectrum of angles $\theta \epsilon (15°, 165°)$, therefore η distribution exhibits a broad plateau in the central pseudorapidity range and falls sharply elsewhere, because $x \to 1$ at the rapidity limits and the PDFs vanishing correspondingly. Figure 2.5(d) and Figure 2.5(e) display generator level distributions for missing transverse energy of the neutrino, $\not{E}_{\mathrm{T}}$, and transverse energy of the electron, E_{T}, respectively. Since the neutrino cannot be directly measured, thus $\not{E}_{\mathrm{T}}$ needs to be reconstructed from the energy imbalance in the transverse plane of the detector. This is based on the assumption that the colliding protons are collinear with the beam direction i.e. do not posses transverse component of momentum. In contrast the electron transverse energy deposited in a calorimeter component is fully measured and characterised by a maximum around 40 GeV, approximately half of the central value of the W boson invariant mass. At the reconstruction stage E_{T} is evaluated as a combination of electron cluster energy deposit, E^{clus}, with the track matching the cluster position, η^{track}, taken in terms of pseudo-rapidity, as follows:

$$E_{\mathrm{T}} = \frac{E^{\mathrm{clus}}}{\cosh(\eta^{track})} \tag{2.6}$$

Figure 2.5(c) shows the generated transverese mass, m_{T}, of the W boson. In terms of the proposed notation for the kinematical variables, m_{T} can be expressed as:

$$m_{\mathrm{T}} = \sqrt{2E_{\mathrm{T}} \cdot \not{E}_{\mathrm{T}}(1 - \cos\phi^{e\nu})} \tag{2.7}$$

here $\phi^{e\nu} = \phi^{e} - \phi^{\nu}$ is the azimuthal angle between electron and neutrino transverse momenta. The quantity m_{T} was introduced in the W boson discovery [1] and is a replacement for the usual invariant mass, only using transverse plane components.

The measurements presented in this thesis are performed at full as well as at the fiducial phase space, where the fiducial volume is defined in terms of generated variables by:

coordinates (r, ϕ) are used in the transverse plane, ϕ being the azimuthal angle around the beam pipe. Radial distances are denoted as $\Delta R = \sqrt{\Delta\eta^2 + \Delta\phi^2}$.

- $|\eta| < 2.47$ excluding $1.37 < |\eta| < 1.52$
- $p_{T,e} > 20\,\text{GeV}$
- $p_{T,\nu} > 25\,\text{GeV}$
- $m_T > 40\,\text{GeV}$

This selection is referred as fiducial volume cuts in the remaining part of the thesis.

2.4 W Boson and charged lepton rapidity distributions

Measurement of the cross sections in the $W \to e\nu_e$ channel has to rely on the electron or positron variables, as the boson is not fully reconstructed. Thus, the straight forward LO relation between the boson rapidity $y_W = \frac{1}{2}\ln\left(\frac{E+p_z}{E-p_z}\right)$ and the parton momentum fractions x_1, x_2 according to Equation 2.1

$$\frac{1}{2}\ln\frac{x_1}{x_2} = y_W\,, \tag{2.8}$$

is of little practical use to interpret the results in terms of PDFs measurements.

In Figure 2.6 the relation between W boson rapidity y_W and the decay electron η_e are shown as predicted by the PYTHIA generator. The correlation between the two is very strong in the central region, while it is nearly completely lost for very forward rapidities $|\eta_e| > 3$. Also, there is a significant difference in the correlation for W^+ and W^- at forward rapidities. Furthermore, Figure 2.6 shows that the correlation gets significantly stronger, once a set of fiducial volume cuts was demanded, in particular a relatively large electron p_{T} greater than 20 GeV. The details in the relation between y_W and η_e can be understood in terms of its dependence on electroweak and kinematic effects as discussed in [22, 33].

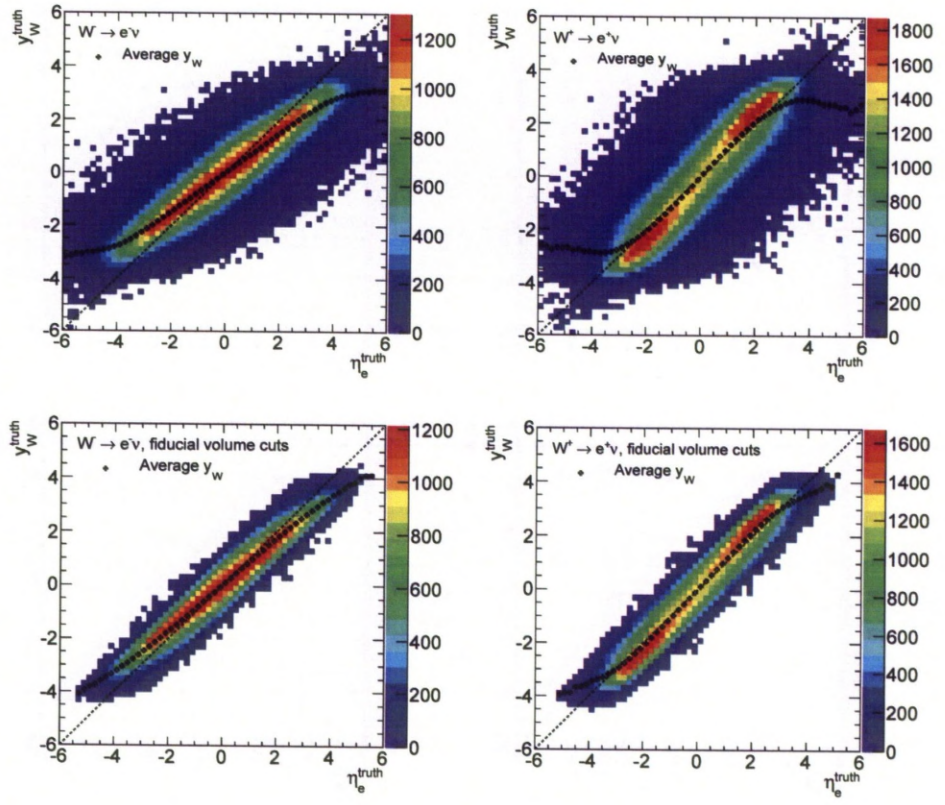

Figure 2.6: Relation between $W^{\pm}$ boson rapidity y_W and the decay electron η_e as generated by Pythia at $\sqrt{s} = 7\,\text{TeV}$. Overlaid are the average y_W values in slices of η_e, and the dashed line corresponds to $y_W = \eta_e$. No selection cuts are applied to the samples in the top row, while for the lower row fiducial volume cuts (except η_e) were required. It is seen that this primarily removes events where little information on y_W is contained in η_e and thus restores the $y_W - \eta_e$ correlation at larger absolute values of η_e.

Chapter 3

Atlas Detector at the LHC

This chapter contains some background information about the Large Hadron Collider (LHC) at CERN. The main components of the ATLAS detector are introduced and summarised, with particular attention concentrated on Tracking and Calorimeter Systems. The ATLAS detector physics run conditions in 2010 are briefly described, including basic information about the Trigger System and Luminosity measurement.

3.1 The Large Hadron Collider

An underground, 27 km long circular tunnel is the home for the largest and most powerful particle accelerator in human history - the Large Hadron Collider (LHC). Located at the European Organization for Nuclear Research (CERN), LHCis mainly designed to accelerate and collide opposing proton beams[1] at a centre of mass energy of 14 TeV and a luminosity of $10^{34}\,cm^{-2}s^{-1}$. On the 30^{th} of March 2010 proton beams collided for the first time at the energy of 3.5 TeV per beam, setting a new record for high-energy collisions and officially starting the LHC research program. LHC will continue to operate at the reduced centre of mass energy of 7 TeV until the end of 2012 (with a short technical stop during

[1]LHC is capable to collide heavy ions (lead nuclei) at energy of up to 2.8 TeV per nucleon. Physics run with lead nuclei has taken place between 8^{th} of November and 6^{th} of December 2010.

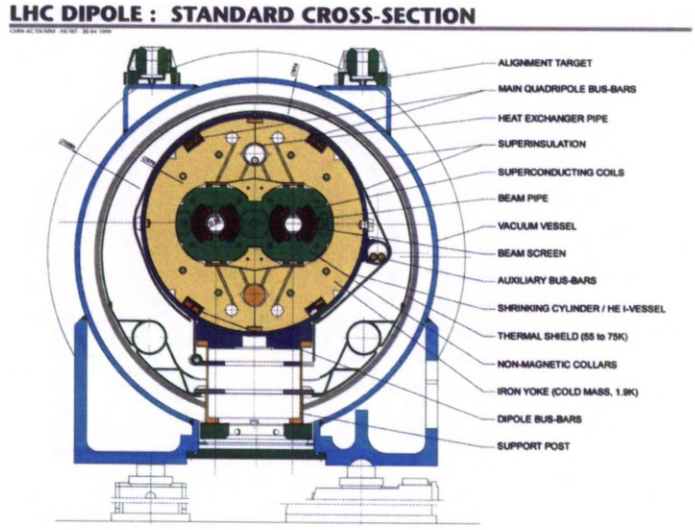

Figure 3.1: Section of the LHC *dipole magnets with clearly visible two apertures for the beam text.*

winter 2011), when it will go into a long shutdown, allowing preparation for an upgrade to run at the design energy of 7 TeV per proton beam in 2014 [34]. The LHC tunnel, previously occupied by the Large Electron-Positron Collider (LEP), now contains two adjacent parallel proton beam pipes that intersect at four interaction points, where the main experiments are located: ALICE, ATLAS, CMS, LHCb. Two general-purpose detectors ATLAS and CMS are designed for precision measurements of the Standard Model parameters, searches for the Higgs Boson and physics beyond the Standard Model. The LHCb detector dedicated to a study of CP violation, mainly through the decay of B mesons, while ALICE concentrates on studying the quark gluon plasma, using heavy ion collisions. In order to obtain the highly energetic LHC proton beams, a large magnetic field is required. A combination of dipole (ensuring the beam has a circular path) and quadrupole (keeping the beam focused) superconducting magnets is used, all cooled to 1.9K with liquid helium. Figure 3.1 shows a cross-section of an LHC dipole.

3.2 The Atlas Detector

The ATLAS (A Toroidal LHC ApparatuS) detector, designed as a multi-purpose detector is able to measure broad range of signals and fulfil a complex physics program. The main goals of the ATLAS detector are: confirmation and improve measurements of known Standard Model parameters, searches for the Higgs boson and investigation of theories beyond the Standard Model. The design challenge was to build a detector enabling high precision measurements in the experimental conditions of the LHC. The design aims can be summarised as [35]:

- High detector granularity with fast, radiation-hard electronics and sensor elements.
- Large acceptance in pseudorapidity, and almost full azimuthal coverage.
- Good momentum resolution, track reconstruction efficiency and vertex identification.
- Very good electromagnetic calorimetry (electron and photon identification and measurements) and full coverage hadronic calorimetry (jet and missing transverse energy measurements).
- Good muon identification (including charge determination) and momentum resolution over a wide range of momenta.
- Extremely efficient trigger system.

In accordance with main design objectives a cylindrical detector enclosing the interaction point was build. Four main sub-detectors can be distinguished, starting from the innermost: the Inner Detector, the electromagnetic and hadronic calorimeters, and the muon spectrometer. An overview of the ATLAS detector, its sub-detectors and the magnet system (a superconducting solenoid surrounding the Inner Detector and large superconducting toroid magnets enclosing the

calorimeters) is presented in Figure 3.2. The following sections contain a general description of the main ATLAS detector sub-components, where the Inner Detector and the calorimeters are the most relevant to the analysis presented in this thesis.

3.2.1 The Inner Detector

The principal function of the Inner Detector (ID) [35] is to provide a comprehensive tracking information, by a precise and efficient track reconstruction within $|\eta| < 2.5$ and $p_{\mathrm{T}} > 0.5$ GeV. A superconducting solenoid surrounding the ID produces an axial magnetic field[2] of 2 T, which bends charged particles, allowing their momenta to be measured. In addition to providing tracking and charge information the ID is used for primary and secondary vertex measurements. To achieve its high performance the Inner Detector comprises three independent but complementary sub-detectors (illustrated schematically on Figure 3.3): the Pixel Detector, the Semiconductor Tracker (SCT) and the Transition Radiation Tracker (TRT).

The Pixel Detector

Lying closest to the beam pipe the silicon Pixel Detector is composed of three layers (the innermost referred to as the b-layer) and three disks on each end-cap, providing the highest granularity. With a total of 1744 modules and approximately 80.4 million read-out channels, the Pixel detector provides excellent position resolution, allowing vertex location within the ID. Each track typically crosses three pixel layers.

[2]The central solenoid magnet system is in fact 80 cm shorter than the ID itself, leading to an inhomogeneous magnetic field. 2 T is the field strength in the central part of the ID, while near the ends of the ID cavity it drops to about 0.5 T. Therefore a precise knowledge of the field distribution is a prerequisite for momentum measurements.

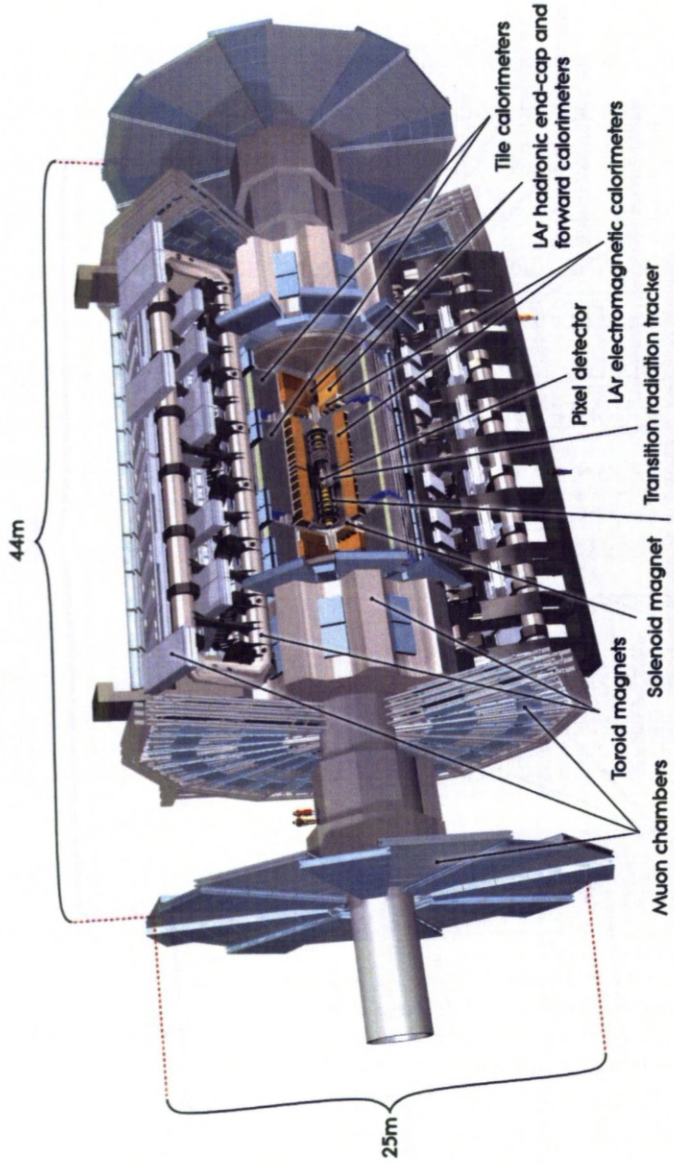

Figure 3.2: Cut-away view of the ATLAS *detector, showing the positions of the various subdetectors*

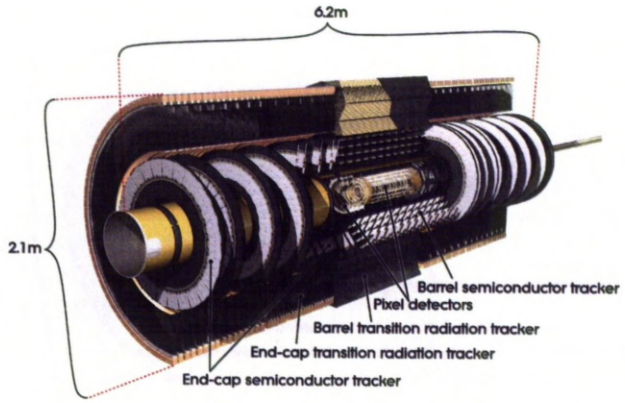

Figure 3.3: Cut-away view of the ATLAS Inner Detector with three main sub-detectors: Pixel, SCT *and* TRT *shown.*

The Semiconductor Tracker

The Semiconductor Tracker (SCT) is located in the middle part of the ID and is composed of four concentric barrels and nine disks in each end-cap, having approximately 6.3 million readout channels. SCT is similar to the Pixel Detector, but in order to cover a larger area, uses long, narrow strips rather than small pixels. Each track crosses eight SCT strip layers (four space points).

The Transition Radiation Tracker

The outermost component of the inner detector, the Transition Radiation Tracker (TRT), uses a combination of a straw tracker and a transition radiation detector. The TRT covers the large volume and has transition radiation detection capability, but is less precise in its determination of the track position and has a reduced eta coverage of $|\eta| < 2.0$. The number of TRT readout channels is approximately 351,000. Typically 36 hits per track are provided by the straw tubes.

3.2.2 The Calorimeters

Located just outside the ID's solenoid magnet, the calorimeter system [36, 37] is composed of the electromagnetic (EM) calorimeter and the hadronic calorime-

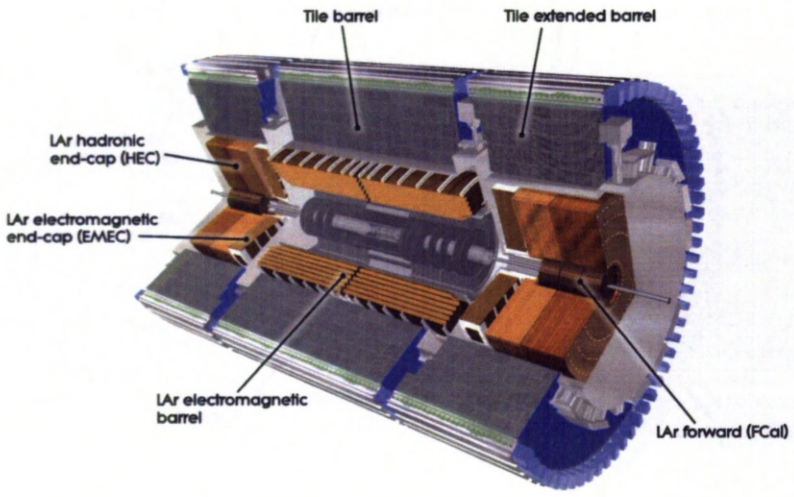

Figure 3.4: Cut-away view of the main components of the ATLAS calorimeter system.

ter, providing accurate energy and position measurements by sampling the energy deposition within $|\eta| < 4.9$. A general overview of the calorimeter system is illustrated on Figure 3.4 The fine granularity of the EM calorimeter enables precise measurements of electrons and photons (over the $|\eta|$ region matching the ID), while the coarser granularity of the rest of the calorimeter is sufficient for reconstruction of the jets and $\not{E}_{\mathrm{T}}$ measurements.

The Electromagnetic Calorimeter

The electromagnetic calorimeter (EM) is composed of the barrel ($|\eta| < 1.475$) and two end-cap regions ($1.375 < |\eta| < 3.2$). The EM uses liquid argon (LAr) as the sampling material and lead plates as an energy absorber. The EM calorimeter is longitudinally segmented, allowing measurement of the particle shower shape evolution within its depth. Over the η region matched to the ID ($|\eta| < 2.5$), which is dedicated to precision measurements of electrons and photons, the EM calorimeter is segmented in three sections in depth and characterised by a high granularity (see Figure 3.5). For the remaining $|\eta|$ acceptance ($2.5 < |\eta| < 3.2$)

Table 3.1: ATLAS *design performance requirements, from [35]. The Muon spectrometer performance is quoted for a muon with* $p_{\mathrm{T}} = 1$ TeV/c, *measured in stand-alone mode, independently of the Inner Detector.*

		η coverage	
Detector component	Required resolution	Measurement	L1 Trigger
Tracking	$\frac{\sigma_{p_{\mathrm{T}}}}{p_{\mathrm{T}}} = 0.05\%\ p_{\mathrm{T}} \oplus 1\%$	± 2.5	–
EM calorimetry	$\frac{\sigma_E}{E} = \frac{10\%}{\sqrt{E}} \oplus 0.7\%$	± 3.2	± 2.5
Hadronic calorimetry			
barrel and endcap	$\frac{\sigma_E}{E} = \frac{50\%}{\sqrt{E}} \oplus 3\%$	± 3.2	± 3.2
forward	$\frac{\sigma_E}{E} = \frac{100\%}{\sqrt{E}} \oplus 10\%$	$3.1 < \lvert\eta\rvert < 4.9$	$3.1 < \lvert\eta\rvert < 4.9$
Muon spectrometer	$\frac{\sigma_{p_{\mathrm{T}}}}{p_{\mathrm{T}}} = 10\%$	± 2.7	± 2.4

the calorimeter has a coarser lateral granularity and only two longitudinal layers. In the region of $|\eta| < 1.8$ an additional layer of LAr is incorporated, which acts as a pre-sampler, used to correct for the energy loss in the ID, the solenoid and the cryostat wall. The region of $1.37 < |\eta| < 1.52$, corresponding to a transition between barrel and end-cap sections, is assumed to have reduced performance (due to a large amount of material in front of the first active calorimeter layer) and excluded in the analysis presented in this thesis.

The Hadronic Calorimeters

The hadronic calorimeters comprise the tile calorimeter, the liquid-argon hadronic end-cap calorimeter (HEC) and the liquid-argon forward calorimeter (FCal). The hadronic calorimeters are dedicated to the identification, reconstruction and energy measurement of particle jets (resulting from hadronization of quarks and gluons) and the measurement of the missing transverse energy in an event. Furthermore the hadronic calorimeters stop and absorb all strongly interacting particles produced in the collisions, preventing hadronic punch-through into the muon system. The tile calorimeter is a sampling detector, which employs scintillating

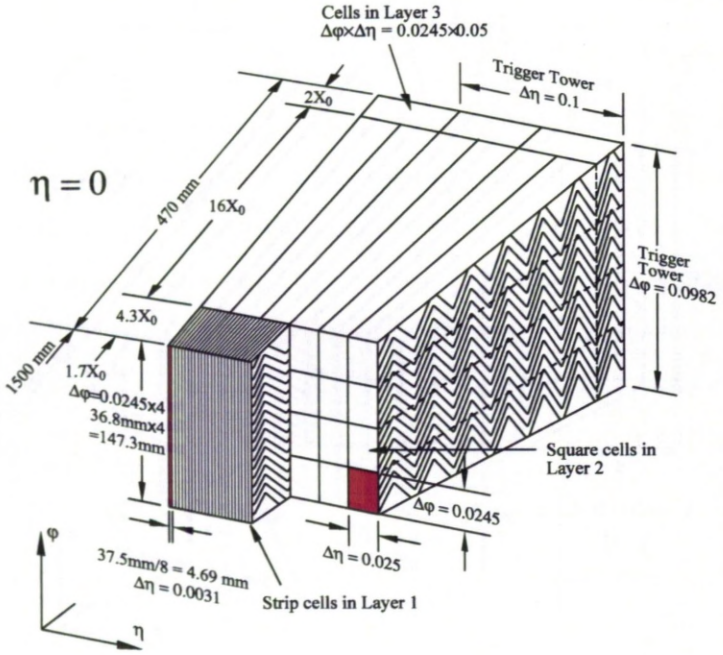

Figure 3.5: Schematic of a section of the barrel LAr *calorimeter. The accordian structure is visible, as well as the different granularity of the cells in η and ϕ for each of three layers and trigger tower. [35].*

tiles as the active material and steel as the absorber, providing acceptance in $|\eta| < 1.7$. The liquid-argon hadronic end-cap calorimeter (HEC) matching the outer $|\eta|$ limits of end-cap electromagnetic calorimeter ($|\eta| < 3.2$). The liquid-argon forward calorimeter (FCal) covers the $|\eta|$ region up to 4.9. The FCal provides both electromagnetic and hadronic energy measurements.

3.2.3 The Muon Spectrometer

The Muon Spectrometer (MS) is the outermost component of the ATLAS Detector, and is designed to measure the trajectories of muons in a magnetic field, supplied by a large superconducting air-core toroid magnet system (a long barrel and two end-cap magnets) in the pseudorapidity range $|\eta| < 2.7$. The MS is instrumented with three layers (stations) of high-precision tracking chambers and a separate trigger system. Two types of tracking chambers are used: Monitored Drift Tubes (MDTs) provide a precision measurement over most of the available $|\eta|$ range and at large pseudorapidities ($2.0 < |\eta| < 2.7$), while Cathode Strip Chambers (CSCs) are used in the inner station. The muon trigger system contains combination of Resistive Plate Chambers (RPCs) in the barrel and Thin Gap Chambers (TGCs) in the end-caps regions, covering the $|\eta| < 2.4$.

3.3 The ATLAS Trigger System

At the LHC design luminosity of $10^{34} cm^{-2} s^{-1}$, a 40 MHz bunch crossing rate combined with an average of 25 interactions per bunch crossing, results in a tremendous amount of data, which is impossible to store permanently. The ATLAS detector trigger system [35, 38, 39] is designed for online selection of interesting events, reducing the output rate to approximately 200 Hz. The trigger system has three levels: Level 1 ($L1$), Level 2 ($L2$), and the Event Filter (EF). The Level 2 and Event Filter form so-called High Level Trigger (HLT). Each trigger level refines the decisions made at the previous level and if an event fails

(at any stage) a given trigger selection criteria, it is rejected and not processed to the next level (or recorded in case of failing the EF).

3.3.1 Level 1 Trigger

The Level 1 ($L1$) is a hardware based trigger designed to reduce the output event rate to a maximum of 75 kHz in less than 2.5 μs. Short decision time is obtained by using only coarse granularity information from the calorimeter and the muon spectrometer. The $L1$ not only performs the first selection step, but also defines so-called Regions of Interest (RoIs). RoIs are defined in terms of so-called trigger towers i.e. sections of central EM calorimeter of dimensions $\Delta\eta\Delta\phi = 0.1 \times 0.1$. The RoI consists of four trigger towers arranged in a 2×2 square, with an associated isolation region surrounding these. The RoI and the corresponding extension it the hadronic calorimeters is shown in Figure ?? RoIs are regions within the detector (represented in η and ϕ coordinates), where $L1$ selection process has identified an interesting object (i.e. energy deposits above certain trigger threshold). Identified RoIs are further investigated by the HLT.

3.3.2 High Level Trigger

The High Level Trigger (HLT) consists of Level 2 ($L2$) and Event Filter (EF), and is software-based system using information from the entire detector. The $L2$ reduces the output rate to approximately 3 kHz with an average processing time of 40 ms/event. The EF carries out the final event selection, by using the offline analysis procedures. The EF reduces the output rate to about 200 Hz with an average processing time of 4 s/event. Finally events accepted by the EF are written to mass storage.

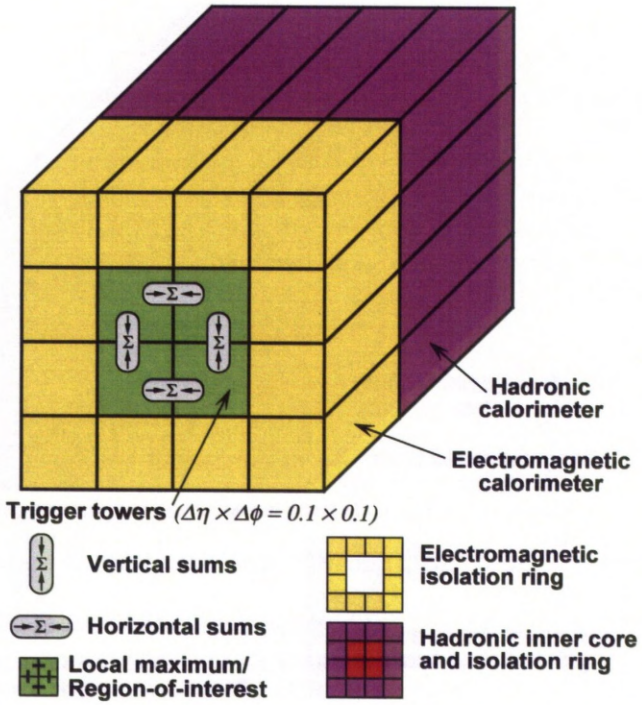

Figure 3.6: Clusters used for e/γ and τ triggers, showing the relative position of the central and the three isolation regions. Figure taken from [35]

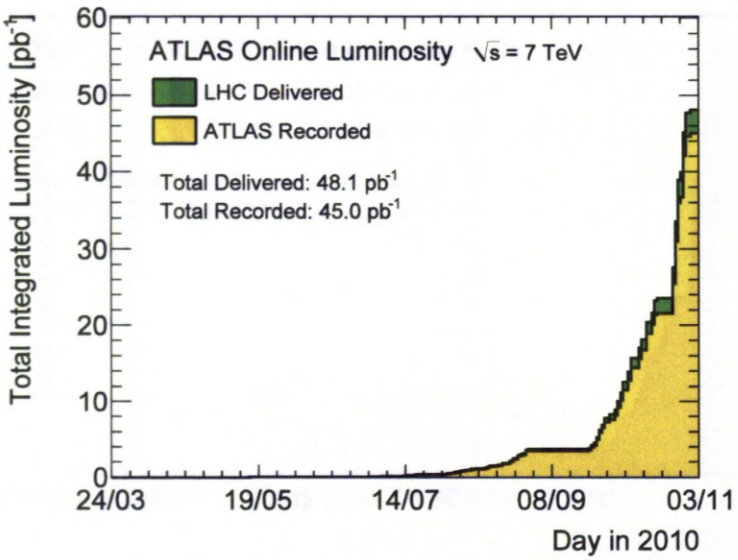

Figure 3.7: The integrated luminosity in days of 2010, delivered (green) and recorded by ATLAS *(yellow) during the stable beam runs with 7 TeV centre of mass energy [40].*

3.4 Data Taking in 2010

The luminosity for the 2010 data has been determined from so-called Van der Meer (or beam separation) scans, where the two beams are scanned against each other in the horizontal and vertical planes to measure their overlap function. The accuracy of the luminosity measurement is estimated to be 3.4 % which is dominated by the 3.1 % uncertainty in the beam current product [41, 42]. As shown on Figure 3.7 the integrated luminosity recorded by ATLAS from March to October 2010, without any additional requirements regarding the run conditions, approached $45\,pb^{-1}$ reaching 93.6% in terms of overall efficiency.

The 2010 data set was divided into periods and sub-periods defined such that they represent run ranges with a consistent configuration of the detector and the trigger. Any significant changes to either the detector configuration/calibration or to the trigger starts a new period. Table 3.2 shows the integrated luminosity

Data period	Sub-period	Run range	Integrated luminosity (nb^{-1})
A	-	152166-153200	0.4
B	B1-B2	153565-155160	9
C	C1-C2	155228-156682	9.5
D	D1-D6	158045-159224	320
E	E1-E7	160387-161948	1118
F	F1-F2	162347-162882	1980
G	G1-G6	165591-166383	9070
H	H1-H2	166466-166964	9300
I	I1-I2	167575-167844	23000
A-I	-	152166-167844	44806.9

Table 3.2: Table showing the data periods and sub-periods in 2010. Luminosity values without any good run list applied. Specific run conditions for each sub-period are reported in [43]

for each data period in 2010.

It was essential however for the analysis presented in this thesis to require data when all relevant components of the detector operated. This is specified by an introduction of so-called good run list [44] (GRL)[3] which are lists of the luminosity blocks (shorter periods of data-taking) where the sub detectors crucial for the e.g. electron analysis are in nominal conditions therefore flagged as good by the data quality flags (DQ). Since DQ flags reflect the overall quality status of the recorded data, per each ATLAS sub-detector, for the periods when there are problems (e.g. sub-detector is of) the data will be lost. In a particular case of the presented analysis the events were required to be included in the standard e/γ (GRL). This specific selection of runs results in $35.1 \pm 1.2\, pb^{-1}$ of available data.

3.4.1 Trigger Selection

ATLAS data acquisition is performed in several so-called streams. The streams differ from each other in terms predefined sets of triggers which need to be satisfied. There are following steams available: muon, $e/gamma$, jet, τ, minimum

[3] *eg_standard_7TeV*

Trigger	Period
L1_EM14	A,B,C,D,E1 - E3
EF_e15_medium	E4 - E7,F,G,H,I

Table 3.3: Electron triggers used during different data taking periods for the W boson inclusive cross section measurement on the full 2010 data.

bias, L1Calo. The *e/gamma* stream is used for the majority of data presented in this analysis and is characterized by events selected by the electron or photon triggers. Several different streams are available depending on the specific requirements of a given analysis. The *e/gamma* stream is used e.g. in the electron channels of Z and W analysis, muon stream in muon for muon decay channels of Z and W etc. The trigger stream used for the initial period of data taking (period A-D) was the L1Calo stream, it was followed by the e/γ stream (for data period E-I). The events in the data period A-E3 (about 2% of the total integrated luminosity), are required to pass `L1_EM14`. This is a Level 1 trigger, which triggers upon an EM cluster with a transverse energy of at least 14 GeV. This trigger became pre-scaled as the instantaneous luminosity of the LHC rapidly increased and the trigger used for the period E4-I was change to `EF_e15_medium`. `EF_e15_medium` triggers upon an electron with transverse energy of above 15 GeV and passing requirements, similar to the offline $Medium\ ID$ but slightly looser, at Event Filter level. `EF_e15_medium` remained un-prescaled throughout the 2010 data-taking.

Chapter 4

Monte Carlo Simulation

The generation of physics processes and the simulation of the response of a high energy detector, - such as ATLAS, are essential prerequisites for understanding the measured data in high energy physics. Since the physical processes take place on a probabilistic basis proportional to the cross section for a given process, Monte Carlo event generators, MC, were used to produce finite numbers of events as they are predicted to occur in the experiment. A number of different MC generators was used to produce samples for signal and background processes relevant to various stages of the analysis presented in this thesis. In particular, Monte Carlo generated event samples were used to extrapolate from the $W \rightarrow e\nu_e$ cross section measured within the detector fiducial acceptance to the total cross section.

4.1 Monte Carlo Generators

In order to model the proton-proton collisions at the LHC, the MC generators must describe the structure of hadrons, parton showers, the hard scattering process and hadronization. The approximations used for the calculations differ between generators and therefore the theoretical predictions rely to a certain extent on the choice of MC generator. The following MC generators were relevant to this thesis:

Pythia6.4

PYTHIAis a general purpose event generator, which is commonly used in high energy physics due to its ease of handling and relatively large predictive power. It can simulate lepton-lepton, lepton-hadron and hadron-hadron interactions within a broad field of theoretical models. The hard scattering process, however, is calculated in leading order approximation (LO) and the higher order corrections are approximated with a parton shower approach, which has limited accuracy for predicting events with higher jet multiplicity. PYTHIA is interfaced with PHOTOS (see below) for the calculations of QED bremsstrahlung, while decays of τ leptons are calculate with the TAUOLA [45–49] package.

Herwig6.5

HERWIG Hadron Emission Reactions With Interfering Gluons is an additional general purpose event generator, similar to PYTHIA. The main differences are the modeling of the parton shower and the hadronization process. PHOTOS and TAUOLA are used for final-state photon radiation and τ decays respectively, exactly as with PYTHIA.

Mc@Nlo3.4

MC@NLO includes the full NLO calculation of rates for QCD processes during the hard scattering. The higher order approximations of the parton showers and the hadronization-step, are calculated by the HERWIG event generator, while the underlying event is modeled using JIMMY4.1 [50]. PHOTOS is used for final state photon radiation.

PHOTOS

The main application of the PHOTOS [51–55] algorithm is the generation of QED radiative corrections to particle decays. It can be used in conjunction with a host of Monte Carlo generators. The algorithm is universal since it requires only the

information about the four-vectors of particles taking part in the process, and the topology of the process, filled in by the host generator. The information is available in the standard event record. PHOTOS intervenes at every event decay branching and generates, with internally calculated probability, bremsstrahlung photons. These are subsequently added to the fraction of already existing events in the event record, independent of the physics process generated. Kinematic configurations are then appropriately modified and energy-momentum conservation is assured. In order to avoid double counting the host generator should not take into account the effects of QED as in the case of e.g. $HERWIG$ where lepton QED radiation is not implemented. When interfaced with PYTHIA the internal PYTHIA parameter `PARJ(90)` [56] representing the threshold in GeV below which leptons do not radiate, should be set to $2 \cdot 10^4$ thus preventing any lepton radiation generated by PYTHIA.

4.2 Analysis Samples

The $W \to e\nu_e$ signal

The primary signal sample used for this thesis consists of $W \to e\nu_e$ events simulated using PYTHIA. There was no additional event filter applied. In order to provide the theory predictions up to next-to-leading order the MC@NLO generator was used with CTEQ6.6 [26] and HERAPDF1.0 [24] NLO parton distribution functions (PDFs).

Electroweak backgrounds

Electroweak backgrounds arise from W and Z production (excluding $t\bar{t}$ and $W \to e\nu_e$). Only certain decay modes have been produced with PYTHIA: $W \to \tau\nu_\tau$, $Z/\gamma^* \to e^+e^-$, $Z/\gamma^* \to \tau^+\tau^-$. Tau leptons are included because they can decay to electrons or produce hadrons (e.g. $\tau^\pm = \pi^\pm\nu_\tau$) which can be eventually misidentified as electrons. Di-boson decays are simulated in HERWIG with the

filter on the final state particles selecting leptonic (electrons and muons only) decay modes. For the Z samples an additional lower mass limit of 60 GeV is imposed on the mass of the boson to remove the low mass Drell-Yan component. In the di-boson samples there is an additional filter on the final state particle kinematics - decay leptons are constrained to $|\eta| < 2.8$ and a minimum value of $p_{\mathrm{T}} = 10$ GeV.

Top quark production

Top quark production forms an important background to $W \to e\nu_e$ events, due to a large $t\bar{t}$ cross section at the LHC and the presence of decay modes involving real W bosons. Decays of top quark can be divided into pure hadronic ($t \to bW \to bq\bar{q}'$) and those involving leptons ($t \to bW \to bl\nu, l = e, \mu, \tau$) in the final state. $t\bar{t}$ events have been generated using MC@NLO with the event filter requiring the event to contain at least one charged lepton from W boson decay (which should originate from the top quark). Events that do not contain $t\bar{t}$ quarks are rejected. Events where both W bosons decay hadronically are not expected to contribute significantly to $W \to e\nu_e$.

4.2.1 JF17

QCD jet events are the major source of fake electrons - the dominant background to $W \to e\nu_e$ channel (see Chapter 6). The QCD di-jet sample used in this thesis was generated with the PYTHIA LO event generator at a centre of mass energy of 7 TeV. The sample contains all QCD processes where the $\hat{p_{\mathrm{T}}}$ of the hard scatter is greater than 15 GeV. The following final states were included according to their respective cross-sections: qq, $q\bar{q}$, gg, qg, $Q\bar{Q}$, $q\gamma$, $g\gamma$, where q denote u, d, s, c, b quarks and $Q = t$. It also contains genuine W and Z boson production. Since the sample is not a pure QCD sample, the events with genuine isolated electrons are not taken into account, as will be described in Chapter 6. The majority of jets produced in QCD events will have too low energy or too large a conical spread

to fake high p_{T} electrons. Therefore an event-level filter, called the jet filter JF, is applied before the simulation stage with GEANT4, in order to select only those events where jets faking the electrons are most likely to occur and hence reduce overall simulation time. The JF filter requires the summed transverse momentum of all generated stable particles (excluding muons and neutrinos) in the window of $\Delta\eta \times \Delta\phi = 0.12 \times 0.12$, within central $|\eta| < 2.7$, to be larger that 17 GeV. The sample is therefore referred as $JF17$. The choice of the window size is based on the observation that genuine electrons produce narrow showers in the electromagnetic calorimeter. The large jet cross section means that the resulting 10 million events correspond only to a very small integrated luminosity of $0.1\,pb^{-1}$ when compared to signal and other background samples. Therefore the data driven method is proposed to improve modeling of the background from jets faking the electrons and the $JF17$ sample is used for the proof of concept and the method development (see Chapter 6).

An overview of the signal and background processes considered- and the generators used for the simulation is given in Table 4.1. All signal and background samples were generated at $\sqrt{s} = 7TeV$ then processed with the GEANT4 [57] simulation of the ATLAS detector [58], reconstructed and passed through the same analysis chain as the data. For the comparison to data, all cross sections, except the $JF17$ cross section, are normalised- to the results of higher order QCD calculations. Predictions for the production cross sections of W and Z bosons, were calculated at $NNLO$ in QCD [21] using the $FEWZ$ [59–61] program. The uncertainties on cross sections arise from the choice of PDF and were derived using the $MSTW08$ $NNLO$ PDF error eigenvectors, including the uncertainty on the strong coupling constant α_s, and variations of renormalisation and factorisation scales [62]. The estimated overall uncertainty of the $NNLO$ W and Z boson cross sections is of the order of $\pm 5\%$ [63] and was propagated to the

normalization of the Monte Carlo samples (see Table 4.1). The $t\bar{t}$ production cross section is given at NLO including the effect of soft-gluon resummation[1] at the next-to-next-leading-logarithmic level ($NNLL$), the uncertainty of 6% is assumed [63] and a 7% uncertainty for di-boson samples. For the QCD background, no reliable prediction can be obtained- from a leading order Monte-Carlo simulation. For the comparisons of differential distributions to data this background is normalised to data. However, for the final cross-section measurement, data-driven methods are used to determine the residual contributions of the QCD background to the final W cross section. All data distributions in this thesis are shown with statistical uncertainties only, based on Poisson statistics [66], unless otherwise stated.

[1]The resummation is one of the methods used to include corrections to all orders in α_S- Leading logarithmic terms are considered to all orders in α_S by algebraic rearrangement e.g. in an exponential function as discussed in [64, 65]

Physics process	Data Set	Generator	σ_{raw}	$\sigma \cdot BR \cdot \varepsilon_{filter}$ [nb]	
$W^+ \to e^+\nu_e$	106081	MC@NLO [28–30]	5.84	6.16 ± 0.31	NNLO [17, 20, 59, 60]
$W^- \to e^-\bar{\nu}_e$	106082	MC@NLO [28–30]	3.96	4.30 ± 0.21	NNLO [17, 20, 59, 60]
$W \to e\nu_e$	106043	PYTHIA [67]	8.94	10.46 ± 0.52	NNLO [17, 20, 59, 60]
$W \to \tau\nu_\tau$	107054	PYTHIA [67]	8.93	10.46 ± 0.52	NNLO [17, 20, 59, 60]
$Z/\gamma^* \to e^+e^-(m_{ee} > 60$ GeV)	106046	PYTHIA [67]	0.86	0.989 ± 0.05	NNLO [17, 20, 59, 60]
$Z/\gamma^* \to \tau^+\tau^-(m_{\tau\tau} > 60$ GeV)	106052	PYTHIA [67]	0.85	0.989 ± 0.05	NNLO [17, 20, 59, 60]
$t\bar{t}$	105200	MC@NLO [28–30]	0.14	$(0.16 \pm 0.01) \cdot 0.56$	NLO + NNLL [68–70]
WW	105985	HERWIG [71]	0.030	$(0.045 \pm 0.003) \cdot 0.388$	NLO
WZ	105987	HERWIG [71]	0.012	$(0.0185 \pm 0.0009) \cdot 0.310$	NLO
ZZ	105986	HERWIG [71]	0.006	$(0.0060 \pm 0.0003) \cdot 0.212$	NLO
$JF17$ ($\hat{p}_T > 15$ GeV)	105802	PYTHIA [67]	1.1×10^6	$1.2 \times 10^6 \cdot 0.1$	LO [67]

Table 4.1: Summary of the Monte Carlo samples used in this thesis. The columns list signal and background distributions as well as the generators used in the production. Data Set number denote the process with specific settings of a given generator. For each sample the cross section output by generator, σ_{raw}, and also the cross section times the branching ratio to which the estimates are normalized multiplied by the efficiency of filter (if exists) applied on the final state particles, $\sigma \cdot BR \cdot \varepsilon_{filter}$, are quoted. See the text for a description of the filters and physics content of each sample. The electroweak W and Z cross sections are calculated at NNLO in QCD, the $t\bar{t}$ is given at NLO including the effect of soft-gluon resummation at the next-to-next-to-leading-logarithmic level (NNLL) and dibosons at NLO in QCD. The cross section for the $JF17$ sample is given at leading order (LO). The sample is generated with requirement on the transverse momentum of the partons involved in the hard-scattering process, $\hat{p}_T$.

4.3 Vertex reconstruction and pile-up reweighting

The determination of the actual position where the proton-proton collision occurred (i.e primary vertex position) is important for the precise measurement of the four-momenta of charged particles. It is also important to distinguish between particles originating from the signal event and particles produced in secondary collisions. For the measurement of primary vertex position the innermost pixel detector layer called the b-layer is used.

As detailed in [72] there are two main steps in the reconstruction of the primary vertex:

- the vertex finding which associates tracks to vertex candidates,
- the vertex fitting which determines the vertex position and its uncertainties,

In the vertex-finding step an iterative approach is used to find the vertex seeds by looking at the local maximum in the distribution of the z coordinate of the track candidates. Next in order to improve the precision of the track parameters the vertex fitting- performs a refitting of the associated tracks. The vertex position is determined using the so-called adaptive vertex fitting (χ^2-based fitting algorithm) [72] which takes as an input the seed position and the tracks around it. The outlying tracks are not rejected but their respective contributions are down-weighted. Tracks which are incompatible with the vertex by more than about seven standard deviations are used to seed a new vertex. In order to define the signal primary vertex the list of vertices ordered according to the sum of transverse momenta squared of associated tracks is produced. In the measurement presented here each primary vertex is required to have at least 3 associated tracks. The choice ensures that the vertex position is uniquely defined.

As was expected, the high instantaneous luminosity of the LHC generates additional collisions in the same bunch crossing (in-time pile-up) and also, due

to the small spacing between bunches, additional collisions in the neighboring bunch crossings (out-of-time pile-up). Both these effects are modeled in MC by overlaying simulations of the hard interaction with the simulation of soft inelastic scattering (minimum bias events). The simulation may be further corrected to data by reweighting the number of primary vertices. MC events with a given vertex multiplicity are reweighted by the scale factor derived from the ratio between the vertex multiplicity in data to the one modeled by MC.

During the period these data were recorded, the average pile-up varied from zero to about two-extra interactions per event with most of the data being recorded with roughly one extra interaction per event. To account for this, the $W \rightarrow l\nu_l$, and QCD-dijet Monte-Carlo samples were generated with an average of two extra primary interactions and then weighted to the primary vertex multiplicity distribution observed in the data (see Figure 4.1).

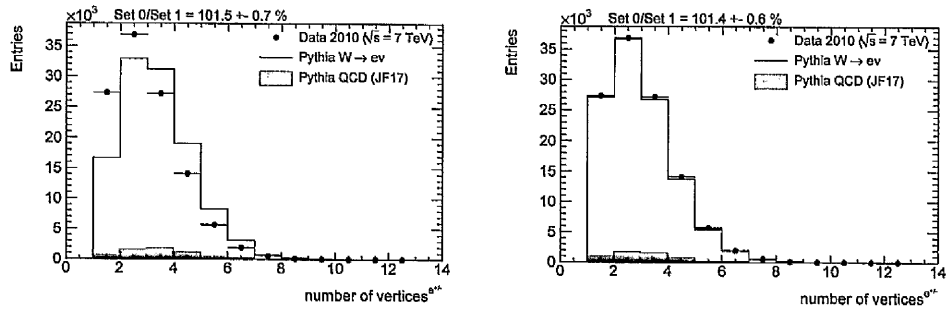

(a) without pile-up reweighting (b) with pile-up reweighting

Figure 4.1: Distributions of the measured and expected number of vertices per event, for the final $W \rightarrow e\nu_e$ selection, (a) before and (b) after vertex reweighting.

Chapter 5

Event Selection and Efficiency

The following chapter describes the selection of W boson specific events and the determination of the data driven electron efficiency. First the reconstruction and identification procedures applied to discriminate potential W candidate events are discussed with a brief overview of the standard ATLAS energy sampling algorithm used to reconstruct clusters from the energy depositions within the electromagnetic calorimeter. Next the analysis-specific selection criteria are introduced together with the efficiency assessment. The data driven methodology for the efficiency estimation is detailed, based on the example of trigger efficiency evaluation, since the components form a vital input for the final measurement of $W^{\pm}$ production with 2010 7 TeV data.

The data and Monte Carlo samples, used for obtaining the results including only part of the 2010 data, are consistently produced using Athena release 15.

5.1 Electron Reconstruction and Identification

The ATLAS standard electron reconstruction and identification algorithm [73] is designed to provide various levels of background rejection optimized for high identification efficiencies, providing coverage over the full acceptance of the inner-detector system. As briefly mentioned in the Chapter 3, the electron reconstruction begins with an identification of a suitable energy deposits (cluster seeds)

of $E_{\mathrm{T}} > 2.5$ GeV in the second layer of the precision region ($|\eta| < 2.5$) of the EM calorimeter. A matching track, extrapolated to the middle EM calorimeter layer, is searched for in a broad window of $\Delta\eta \times \Delta\phi = 0.05 \times 0.1$ amongst all reconstructed tracks with $p_{\mathrm{T}} > 0.5$ GeV. The closest-matched track to the cluster barycenter of this layers is kept as that belonging to the electron candidate. The final electron candidates have cluster sizes of $\Delta\eta \times \Delta\phi = 0.075 \times 0.175$ (3×7 cells) in the barrel calorimeter and 0.125×0.125 (5×5 cells) in the end-cap. The tracks are reconstructed within $|\eta| < 2.5$ using a pattern recognition algorithm with full ϕ coverage that starts from pixel and SCT silicon hits and adds hits from the TRT. The resulting track candidates with transverse momenta above 100 MeV are recorded. Additionally, a second pattern-recognition algorithm is adopted starting from the TRT and searching for hits inwards in the detector, with the exclusion of tracks already used in step one. In this step, tracks from secondary interactions, such as photon conversions and long-lived hadron decays, with $p_{\mathrm{T}} > 300$ MeV are recorded.

The following baseline electron identification selection criteria [73] combines calorimeter and tracker information with the granularity optimized in 10 bins in η and 11 bins in E_{T}. Three reference sets of requirements (*Loose*, *Medium*, and *Tight*) are available, providing progressively stronger jet rejection at the expense of some identification efficiency loss. Each set adds additional constraints to the previous requirements:

- *Loose*: basic selection relies on EM shower shape information from the second sampling of the EM calorimeter (lateral containment and width) and energy leakage into the hadronic calorimeters as discriminant variables. This set of requirements provides high and uniform identification efficiency but a low background rejection;
- *Medium*: selection provides additional hadronic rejection by evaluating the energy deposit patterns in the first layer of the EM calorimeter (the shower

width and the ratio of the energy difference associated with the largest and second largest energy deposit over the sum of these energies), track quality variables (number of hits in the pixel and silicon trackers, the transverse impact parameter defined as the distance of the closest approach of the track to the reconstructed primary vertex point, measured in the transverse plane of the track) and a cluster-track matching variable ($\delta\eta$ between the cluster and the track extrapolated to the first layer of the EM calorimeter);

- *Tight*: this selection further rejects charged hadrons and secondary electrons from conversions by fully exploiting the electron identification potential of the ATLAS detector. It makes requirements on the ratio of cluster energy to track momentum, on the number of hits in the TRT, and on the ratio of high-threshold to the total number of hits in the TRT. Electrons from conversions are rejected by requiring at least one hit in the first layer of the pixel detector (alias b-layer). A conversion-flagging algorithm is also used to further reduce this contribution. The impact-parameter requirement applied in the medium selection is further tightened at this level.

Table 5.1 lists all variable used in the *Loose*, *Medium* and *Tight* selection.

The jet rejection obtained from the *Loose*, *Medium* and *Tight* requirements for electron candidates with $E_{\mathrm{T}} > 17$ GeV has been estimated on Monte Carlo to be of the order of 10^2, 10^3 and 10^5, for the signal efficiency of 95%, 90% and 70% respectively [74]

5.2 Selection of $W \to e\nu_e$ candidates

This section will list stages of the selection procedure applied to identify W boson candidates. The reliability of the method is assessed via kinematic distributions for the variables of interest. W candidates selection criteria were exercised on the data covering *periods* $A-I$ of the data taking, effectively 78% statistics available

Type	Description
	***Loose* selection**
Acceptance	$\lvert\eta\rvert < 2.47$
Hadronic leakage	Ratio of E_{T} in the first layer of the hadronic calorimeter to E_{T} of the EM cluster (used over the range $\lvert\eta\rvert < 0.8$ and $\lvert\eta\rvert > 1.37$)
	Ratio of E_{T} in the hadronic calorimeter to E_{T} of the EM cluster (used over the range $\lvert\eta\rvert > 0.8$ and $\lvert\eta\rvert < 1.37$)
Second layer of EM calorimeter	Ratio of the energy in 3×7 cells over the energy in 7×7 cells centred at the electron cluster position
	Lateral width of the shower
	***Medium* selection (includes *Loose*)**
First layer of the EM calorimeter	Total shower width
	Ratio of the energy difference between the largest and second largest energy deposits in the cluster over the sum of these energies
Track quality	Number of hits in the pixel detector (≥ 1)
	Number of hits in the pixel and SCT detectors (≥ 7)
	Transverse impact parameter (< 5 mm)
Track-cluster matching	$\Delta\eta$ between the cluster and the track (< 0.01)
	***Tight* selection (includes *Medium*)**
b-layer	Number of hits in the b-layer (≥ 1)
Track-cluster matching	$\Delta\phi$ between the cluster and the track (< 0.02)
	Ratio of the cluster energy to the track momentum (E/p)
	Tighter $\Delta\eta$ requirement (< 0.005)
Track quality	Tighter transverse impact parameter cut (< 1 mm)
TRT	Total number of hits in TRT
	Ratio of the number of high-threshold hits to the to the total number of hits in TRT
Conversions	Electron candidates matched to the reconstructed photon conversions are rejected

Table 5.1: Detailed list of identification variables used for the Loose, Medium and Tight electron identification requirements. For the central region of detector ($\lvert\eta\rvert < 2.47$)(adapted from Ref. [75])

from the 7 TeV 2010 runs. The standard e/γ Good Run Lists (*GRLs*) recommendations were used [44]. The luminosity for each period has been computed with the systematic uncertainty of 3.4% [41]. Signal and background Monte Carlo samples used in the analysis are listed in Chapter 4.

5.2.1 Missing Transverse Energy

In the $W \rightarrow e\nu_e$ decay channel, reconstruction of the missing transverse energy escaping with an undetected neutrino is of a prime importance. As already indicated it is based on the assumption that the colliding proton bunches are collinear with the beam direction. Calculation of the energy imbalance in the transverse plane to the beam direction is based exclusively on the information from *EM* calorimeter, including FCal (muons are not included). This relies on a cell-based algorithm which sums the energy deposits from the calorimeter' cells inside three - dimensional topological clusters ("topoclusters") [76]. The clusters are formed by calorimeter cells with energy $E^{clus} > 4\sigma$ above the noise, where σ is the *RMS* of the noise. Subsequently, closest neighbors are added for all cells with signals above a secondary threshold $E^{clus} > 2\sigma$. Finally, the energy in all further immediate neighbors of this secondary cells is added. The cell energies are summed to give the cluster energy. The baseline calibration for these clusters corrects their energy to the electromagnetic scale, which was established using test-beam measurements for electrons and muons in the electromagnetic and hadronic calorimeters. The topoclusters are then corrected according to the local hadron calibration scheme [77] to take into account the different responses to hadrons and to electrons or photons and known sources of energy loses in inactive material, such as the Liquid Argon Calorimeter cryostat walls. In a first step clusters are classified as electromagnetic or hadronic clusters. Next the local hadron calibration weights are applied to the topoclusters based on the energy density in the cells. The weighting scheme corrects for the different e/π response in the

ATLAS calorimeter. Finally the dead material and out of cluster corrections yield the energy deposited by the final state particles in the ATLAS calorimeter.

The $x-$ and $y-$ components of the calorimeter $\not{E}_{\mathrm{T}}$ term are calculated by summing over the transverse energies measured in these topological cluster cells i, calibrated according to the local hadron calibration scheme

$$E_{x,y}^{miss} = -\sum_{cells} E_{x,y}^{calo}$$

and hence the $\not{E}_{\mathrm{T}}$ variable is defined as a scalar norm:

$$\not{E}_{\mathrm{T}} = \sqrt{(E_x^{miss})^2 + (E_y^{miss})^2} \tag{5.1}$$

5.2.2 Preselection of high E_{T} electrons

Following standard ATLAS recommendations [78], the selection is performed using a combinations of electromagnetic calorimeter cluster variables for electron energy, and η and ϕ coordinates provided by the inner detector tracking system. The choice ensures that electron energy information is based exclusively on the calorimeter performance while the accuracy of the coordinates relies on the tracking capabilities of the ATLAS detector. Electron candidates passing $et > 20$ GeV must be detected within fiducial region of the inner detector i.e. $|\eta| < 2.47$, with the exclusion of the transition between the barrel and the end-cap ($1.37 < |\eta| < 1.52$). Potential W boson candidates are required to occur in good lumiblocks as indicated in the *GRLs*.

The trigger requirement used with Monte Carlo samples is dictated by selections made during the data taking when two electron triggers were chosen. For low luminosity periods (starting from A up to run 160530 of period E) the $L1$ trigger `L1_EM_14` was used with a nominal threshold $E_{\mathrm{T}} > 14$ GeV, while for the remaining periods (98% of collected statistic) the high level trigger `EF_e15_medium` was used, with a threshold $E_{\mathrm{T}} > 15$ GeV and *Medium* electron requirement. For the event to be accepted the sum of hits in the pixel detector and semi-conductor

SCT tracker should exceed 3 ("SCT + pixel hits" in Table 5.2). Selected events must have at least one primary reconstructed vertex compatible with the beam-spot position in bunch crossing, moreover the primary vertex must have at least three reconstructed tracks associated to it("Primary vertex").

Further Object Quality cuts ("OTX cleaning") are applied to ensure correct reconstruction of the electron energy deposits within the LAr calorimeter. The procedure uses the information about LAr problematic regions, from the online LAr monitoring system, summarized on $\eta - \phi$ maps with the granularity of an individual cell. Each map is valid for the range of runs depending on the nature and history of the problem which may involve: isolated cells producing a high noise signal or no signal at all, regions affected by high voltage problems, lack of output signal due to "dead" optical readout line *etc.* If the cluster involves cells where the major problem (i.e."dead" OTX) has been identified, the energy of the cluster will be affected by exclusion of these cells i.e. cell energy is set to 0 at the reconstruction stage, therefore the cluster has to be rejected. This is ensures that the same amount of luminosity per OTX map is chosen for Monte Carlo samples as it was during data acquisition periods. The status of the LAr calorimeter up to the run 167521 can be seen in Figure 5.1.

To avoid problems with cosmic ray muons or bursts of noise which can produce localized high energy deposits in the EM and hadronic calorimeters, an additional jet cleaning procedure ("$\not\!\!E_{\mathrm{T}}$ cleaning") was performed, as detailed in [79,80]. The step is required in order to measure $\not\!\!E_{\mathrm{T}}$ with required accuracy. Jets are flagged as *bad* if they coincide with noisy cells in the hadronic endcap calorimeter, are indicative of coherent noise in the EM calorimeter, or have large out-of-time energy deposits (e.g. from cosmic rays). Any event containing a *bad* jet with $p_{\mathrm{T}} > 10$ GeV is rejected. Further information on jet cleaning can be found in [79].

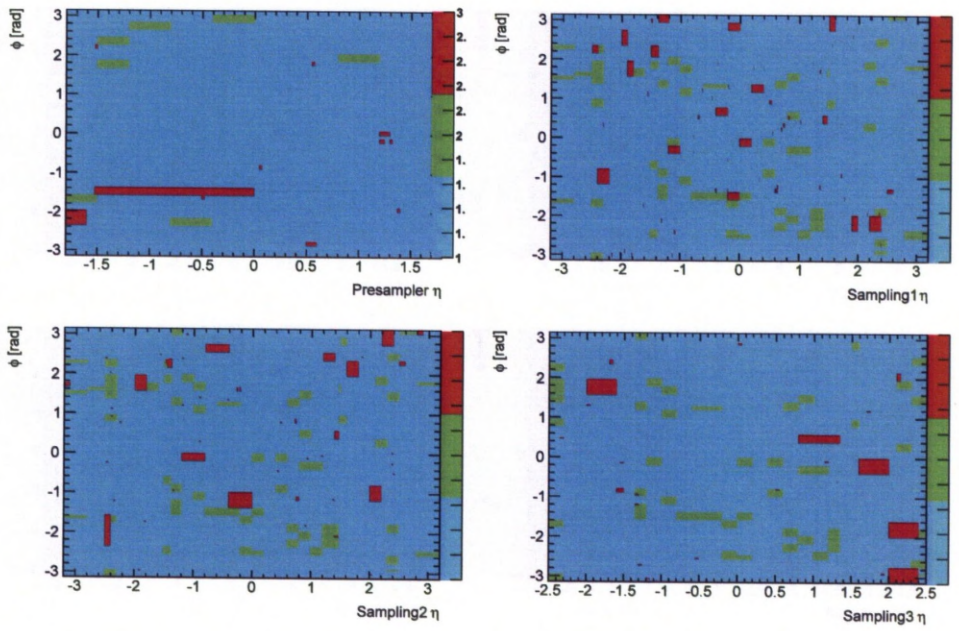

Figure 5.1: OTX maps in $\eta-\phi$ space of the presampler and tree sampling layers of the electromagnetic calorimeter. Status shown for runs 166658−167521. Different colors represents the status of the given cell, in following manner: Turquoise - cell is functioning well; Green - non-nominal high voltage, corrected during reprocessing; Red - regions where the major problem exists

5.2.3 W boson specific selection

In order to discriminate $W \to e\nu_e$ from the background events additional requirements beyond those already specified in Section 5.2.2 are set. The electrons identification level, as described in Section 5.1, is set to *Tight* to ensure that electrons which passed through disabled $b-layer$ modules are not flagged as photon conversions. To suppress Z bosons contamination, events with more than one *Medium* electron passing $E_{\mathrm{T}} > 20$ GeV are excluded ("Z veto"). Finally, W candidates must meet $\not{E}_{\mathrm{T}} > 25$ GeV and $m_{\mathrm{T}} > 40$ GeV.

In order to derive QCD background from the data, the additional requirement on the calorimetric isolation variable was proposed $E_{\mathrm{T}}^{cone}(0.3)$. This is is only mentioned here and more details are presented in Chapter 6 along with the actual implementation of the method.

Summary of the final W selection criteria:

- Preselection
  - SCT + pixel hits
  - Trigger
  - Primary vertex
  - OTX cleaning
  - $\not{E}_{\mathrm{T}}$ cleaning
  - $|\eta| < 2.47$ (no crack) i.e. excluding $1.37 < |\eta| < 1.52$
  - $E_{\mathrm{T}} > 20\,\mathrm{GeV}$
  - *Losse*
  - *Medium*
- W specific selection

- *Tight*
- Z veto
- $\not{E}_{\mathrm{T}} > 25\,\mathrm{GeV}$
- $m_{\mathrm{T}} > 40\,\mathrm{GeV}$
- $E_{\mathrm{T}}^{cone}(0.3) < 10\,\mathrm{GeV}$

Table 5.2 summarizes the number of data, simulated $W \to e\nu_e$ signal, electroweak (EW), $t\bar{t}$ and $JF17$ background events after each of the requirements described above. The final W selection results in 114047 events in data for an integrated luminosity of $35.1\,pb^{-1}$. From the signal Monte Carlo simulation, the expected number of $W \to e\nu_e$ events that pass the selection is 106492 ± 206 events. Monte Carlo estimate of 3621 ± 34 events for the background contamination from W, $t\bar{t}$, $Z$is roughly equal to final number of $JF17$ events. The uncertainties correspond to the MC statistical uncertainties. From the summary of the final W selection in the case of QCD background the suppression is mostly achieved by the electron quality cuts that reject events with fake $\not{E}_{\mathrm{T}}$ (due to energy mismeasurement) and final $\not{E}_{\mathrm{T}} > 25$ GeV selection. The effect has been depicted in Figure 5.2. The EW background is strongly reduced by the $\not{E}_{\mathrm{T}} > 25$ GeV and Z veto in case of Z boson sources. Additional selection criteria exploiting the characteristic properties of $W \to e\nu_e$ decays further separate the W signal from the backgrounds.

Given the small number of events remaining in the $JF17$ after the final W selection (before normalization to the data luminosity), which is due to the small size of produced MC sample in conjunction with large rejection factors of the selection criteria, it is clear that the final differential analysis cannot rely on simulated events alone to accurately predict the fraction of QCD processes. Therefore, the QCD background is treated separately, based on the estimate derived from the data. This will be discussed in Chapter 6.

(a) $W \to e\nu_e$

Cut	Data	$W \to e\nu_e$	JF17	$W \to \tau\nu_\tau$	$t\bar{t}$	$Z/\gamma^* \to e^+e^-$	$Z/\gamma^* \to \tau^+\tau^-$
Preselection							
SCT + pixel hits	36038843	244996 ± 314	300291065 ± 218427	65360 ± 162	2549 ± 8	26264 ± 32	11707 ± 67
Trigger	10793376	213180 ± 293	8180728 ± 36094	14920 ± 77	1034 ± 5	25041 ± 31	2948 ± 34
Primary vertex	10793230	213126 ± 293	8180728 ± 36094	14920 ± 77	1034 ± 5	25038 ± 31	2947 ± 34
OTX cleaning	10072894	195430 ± 281	7522294 ± 34604	13716 ± 74	947 ± 5	23108 ± 30	2702 ± 32
$\not{E}_T$ cleaning	10071869	195425 ± 281	7522294 ± 34604	13716 ± 74	947 ± 5	23106 ± 30	2701 ± 32
$\|\eta\| < 2.47$ (no crack)	9655391	185456 ± 273	6776060 ± 32833	13068 ± 72	901 ± 5	22101 ± 29	2563 ± 31
$E_T > 20$ GeV	4393460	169717 ± 261	3264110 ± 22774	8403 ± 58	823 ± 5	20885 ± 28	1749 ± 26
Loose	2424444	166713 ± 257	1924931 ± 17492	7949 ± 56	784 ± 5	20578 ± 28	1656 ± 25
Medium	1933983	161101 ± 251	1466423 ± 15277	7560 ± 54	754 ± 5	20177 ± 27	1553 ± 24
W specific selection							
Tight	449846	132618 ± 230	266995 ± 6495	5943 ± 49	649 ± 4	18935 ± 27	1176 ± 21
Z veto	436114	132471 ± 230	266272 ± 6488	5934 ± 49	602 ± 4	5982 ± 15	1139 ± 21
$\not{E}_T > 25$ GeV	124200	107946 ± 208	7825 ± 1054	3237 ± 36	513 ± 4	224 ± 3	295 ± 10
$m_T > 40$ GeV	116797	106838 ± 207	3665 ± 732	2831 ± 34	424 ± 3	208 ± 3	187 ± 8
$E_T^{cone}(0.3) < 10$ GeV	114047	106492 ± 206	2325 ± 568	2822 ± 33	406 ± 3	206 ± 3	187 ± 8

(b) $W^+ \to e^+\nu_e$

Cut	Data	$W \to e\nu_e$	JF17	$W \to \tau\nu_\tau$	$t\bar{t}$	$Z/\gamma^* \to e^+e^-$	$Z/\gamma^* \to \tau^+\tau^-$
Preselection							
SCT + pixel hits	18362169	147922 ± 244	150145532 ± 109213	36520 ± 121	1273 ± 6	13266 ± 22	5874 ± 47
Trigger	5495206	128367 ± 227	4090364 ± 18047	8832 ± 60	513 ± 4	12646 ± 22	1518 ± 24
Primary vertex	5495121	128332 ± 227	4090364 ± 18047	8832 ± 60	513 ± 4	12644 ± 22	1518 ± 24
OTX cleaning	5125808	117676 ± 218	3761147 ± 17302	8143 ± 57	471 ± 4	11667 ± 21	1390 ± 23
$\not{E}_T$ cleaning	5125290	117672 ± 218	3761147 ± 17302	8143 ± 57	471 ± 4	11666 ± 21	1390 ± 23
$\|\eta\| < 2.47$ (no crack)	4913551	111558 ± 212	3388030 ± 16416	7744 ± 56	448 ± 4	11153 ± 21	1322 ± 22
$E_T > 20$ GeV	2259448	101228 ± 202	1632055 ± 11387	4986 ± 45	408 ± 3	10538 ± 20	901 ± 19
Loose	1245145	99442 ± 199	962466 ± 8746	4718 ± 43	388 ± 3	10383 ± 20	850 ± 18
Medium	995934	96191 ± 194	733211 ± 7639	4499 ± 42	373 ± 3	10180 ± 19	799 ± 17
W specific selection							
Tight	240920	79315 ± 178	133498 ± 3247	3542 ± 38	322 ± 3	9551 ± 19	615 ± 15
Zveto	234061	79219 ± 178	133136 ± 3244	3536 ± 38	299 ± 3	3039 ± 11	593 ± 15
$\not{E}_T > 25$ GeV	73253	63579 ± 160	3913 ± 527	1913 ± 28	253 ± 3	116 ± 2	151 ± 7
$m_T > 40$ GeV	69395	62850 ± 159	1833 ± 366	1641 ± 26	209 ± 2	108 ± 2	95 ± 6
$E_T^{cone}(0.3) < 10$ GeV	67941	62651 ± 158	1163 ± 284	1636 ± 25	201 ± 2	107 ± 2	95 ± 6

(c) $W^- \to e^-\bar{\nu}_e$

Cut	Data	$W \to e\nu_e$	JF17	$W \to \tau\nu_\tau$	$t\bar{t}$	$Z/\gamma^* \to e^+e^-$	$Z/\gamma^* \to \tau^+\tau^-$
Preselection							
SCT + pixel hits	17676674	97074 ± 198	150145532 ± 109213	28840 ± 108	1276 ± 6	12998 ± 22	5833 ± 47
Trigger	5298170	84813 ± 185	4090364 ± 18047	6088 ± 49	520 ± 4	12395 ± 22	1429 ± 23
Primary vertex	5298109	84794 ± 185	4090364 ± 18047	6088 ± 49	520 ± 4	12393 ± 22	1429 ± 23
OTX cleaning	4947086	77755 ± 177	3761147 ± 17302	5573 ± 47	476 ± 4	11441 ± 21	1313 ± 22
$\not{E}_T$ cleaning	4946579	77753 ± 177	3761147 ± 17302	5573 ± 47	476 ± 4	11440 ± 21	1311 ± 22
$\|\eta\| < 2.47$ (no crack)	4741840	73898 ± 172	3388030 ± 16416	5324 ± 46	453 ± 4	10947 ± 20	1241 ± 22
$E_T > 20$ GeV	2134012	68489 ± 166	1632055 ± 11387	3417 ± 37	415 ± 3	10348 ± 20	847 ± 18
Loose	1179299	67272 ± 163	962466 ± 8746	3231 ± 36	396 ± 3	10195 ± 20	806 ± 17
Medium	938049	64910 ± 159	733211 ± 7639	3062 ± 35	381 ± 3	9997 ± 19	754 ± 17
W specific selection							
Tight	208926	53302 ± 146	133498 ± 3247	2402 ± 31	327 ± 3	9384 ± 19	562 ± 14
Zveto	202053	53252 ± 146	133136 ± 3244	2398 ± 31	304 ± 3	2943 ± 11	546 ± 14
$\not{E}_T > 25$ GeV	50947	44366 ± 133	3913 ± 527	1324 ± 23	260 ± 3	108 ± 2	143 ± 7
$m_T > 40$ GeV	47402	43988 ± 133	1833 ± 366	1190 ± 22	215 ± 2	100 ± 2	92 ± 6
$E_T^{cone}(0.3) < 10$ GeV	46106	43841 ± 132	1163 ± 284	1186 ± 22	206 ± 2	99 ± 2	92 ± 6

Table 5.2: Cut flow tables showing the number of events passing each step of the final W boson selection on 2010 data and Monte Carlo

5.3 Electron efficiency determination in Data

The following section splits into parts where electron correction factors, used to account for data/MC[1] differences, are assessed. The scaling relies on the evaluation of electron reconstruction, identification and trigger efficiencies with the use of the data driven methodologies, *Tag* and *Probe*. Furthermore, the electron energy scale calibration is assessed. These steps are vital for further cross-section calculations where simulated data samples are used as the main components. Since the electron identification efficiency is highly dependent on the kinematics of the electron, the efficiencies and SFs are measured as a function of η and E_{T} .

5.3.1 *Tag* and *Probe*

The *Tag* and *Probe* (*T&P*) is a data driven technique, central for the estimate of efficiencies. In order to calculate the efficiency one needs a pair of related objects coming e.g from a mass resonance (i.e. J/ψ, Z etc.). The di-electron $Z/\gamma^* \rightarrow e^+e^-$ channel has a clear decay signature and easily reducible background, therefore is well suited for the *Tag* and *Probe* application. The relation between electrons from Z is explored by applying stringent selection to the *Tag* electron, responsible for triggering an event, and less stringent to the *Probe* electron, leaving *Probe* unbiased from the selection of the event. The details however depend on the specific analysis. The technique can be applied in various efficiency requirement scenarios, depending on the respective definitions of *Tag* and *Probe*. It is worth mentioning that efficient background substraction is crucial for reliable extraction of the *Tag*s and *Probe*s . Since the *Tag* is already subject to a very

[1]The ratio between the data measurements and the Monte Carlo predictions *data/MC* are frequently referred to as 'scale factors' (*SF*).

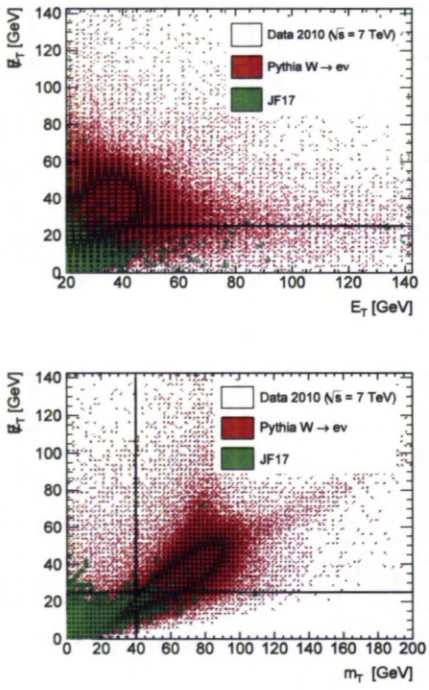

Figure 5.2: E_T^{miss} vs (a) electron cluster E_T and (b) m_T. Red color marks signal, Green background Monte Carlo. Distributions indicate that the choice of the kinematic selection greatly enhance $W \to e\nu_e$ signal over expected background. Monte Carlo predictions are normalised to the data luminosity.

strict selection requirements compared to the *Probe* it is important to address the background contamination at each level of the efficiency assessment, when applying different sets of criteria to the *Probe*. Finally, a small combinatorial background present in the signal Monte Carlo i.e majority of *Probes* comes from the investigated channel, requires the the data-driven efficiencies to be compared to efficiencies for truth-matched electrons in *MC*. After the efficiencies have been obtained in both the data and MC, data/MC scale factors can be calculated. The official ATLAS recommendations for the values of the scale factors are used by physics groups to correct the simulated data for the data/MC discrepancies. The methodology was applied for the W boson cross section measurement summarized in this thesis.

T&P Working Example

The *Tag* and *Probe* method is central for the assessment of electron efficiencies, therefore it is instructive, first to demonstrate a working example of its direct application, before specifying recommendations used in the presented analysis. For the purpose of the exercise *T&P* results shown here are performed using period D-J of 2011 7TeV data set ($1.7\,fb^{-1}$) and Monte Carlo samples reprocessed with the newest ATLAS reconstruction software (Athena release v17). Z boson electrons kinematically resemble $W \rightarrow e\nu_e$, therefore *T&P* electron efficiencies evaluated with this channel are essential inputs to $W \rightarrow e\nu_e$ analysis. For simplicity the choice was made to estimate `EF_e20_medium` electron trigger *T&P* efficiency with respect to offline selection. Therefore, complicated assessment of background contamination may be avoided. This is achieved by stringent identification requirements, i.e. applying *Medium* or *Tight* selection, which in the case of $Z/\gamma^* \rightarrow e^+e^-$ results in background below the percent level. The similarity between Z and W boson invariant masses leads to the same electron preselection requirements in both cases (see Section 5.2.2). Further Z analysis specific selec-

tions involve the choice of two *Medium* electrons with the highest E_T, imposing a mass window for di-electron invariant mass of $66 < M_{ee} < 116$ GeV and requiring opposite charge for the electrons in selected pairs. From the determined subsample of Z events we select *Tag* electrons by imposing *Tight ID* and ensuring that it has actually triggered the given event, i.e. for `EF_e20_medium`, *Tag* needs to match the triggered object within $\Delta R < 0.15$ cone at Level 1 ($L1$), Level 2 ($L2$) and Event Filter (EF) in order to trigger the event. For selected *Tag* events we impose *Medium* or *Tight* electron *ID* on the second electron, *Probe*, and subsequently test the *Probe* against the trigger requirement.

The trigger efficiency is evaluated from a ratio of the number of *Probes* matched to the trigger, $N_{P,trigger}$, to all *Probes*, $N_{P,all}$:

$$\epsilon_{trigger} = \frac{N_{P,trigger}}{N_{P,all}} \tag{5.2}$$

For clarity the specific requirements used for the selection of the *Tag* and the *Probe* electrons were summarized below:

- common for both, the *Tag* and for the *Probe*:
  - standard e/γ *GRLs* selection
  - Primary vertex cut
  - `EF_e20_medium` trigger selection
  - *OTX* cleaning
  - $|\eta| < 2.47$
  - $E_T > 20\,\text{GeV}$
- additional for the *Probe*:
  - *Medium* or *Tight* electron identification
- additional for the *Tag*:

- $\Delta R < 0.15$ in $\{\eta, \phi\}$[2]. between an offline electron (Tag) and triggered object
- exclusion of the calorimeter crack region $1.37 < |\eta| < 1.52$
- *Tight* electron identification
- opposite charge between the Tag and *Probe*

As already mentioned the background contamination at the trigger efficiency numerator level is low and compatible with the denominator, thus subtraction is not applied for the trigger efficiency calculation. In principle the choice between *Medium* and *Tight* selection allows us to differentiate the analysis requirements of $Z/\gamma^* \to e^+e^-$ and $W \to e\nu_e$. Nevertheless, as presented in Figure 5.3, efficiencies w.r.t. *Medium* and w.r.t. *Tight* agree overall at the per mil level. The `EF_e20_medium` trigger is expected to have high efficiency for electrons with transverse momentum above 20 GeV. There is essentially $\sim 99\%$ efficiency found for electrons above 40 GeV with the turn on curve clearly visible (see Figure 6.3(b) and 5.3(d)). For electron pseudorapidity a slight increase in efficiency towards the central values is observed (see Figure 6.3(a) and 6.3(c)). No large dependance is visible apart from the drop in efficiency and observed asymmetry at $\eta = \pm 1.5$ related to the poorly instrumented crack regions of the detector. Moreover no electron charge dependency for the efficiency was found. The observations correlate well with the choice of the electron identification SF used in this thesis where a single set was used for both W^+ and W^- candidate events (see Table 5.3).

In order to evaluate SF the efficiency was derived also from Monte Carlo samples. In case of electron p_T (see Figure 5.3(f)) the efficiency was well reflected in simulation. For electron η, in contrast, the variation of up to $\sim 3\%$ was observed ranging from undervaluation in the central region to overvaluation of

[2]The ΔR distance is chosen since it is comparable to the size of reconstructed clusters in electromagnetic calorimeter (EM), therefore *Region of interest* (RoI) cannot be associated with a cluster if it is further away

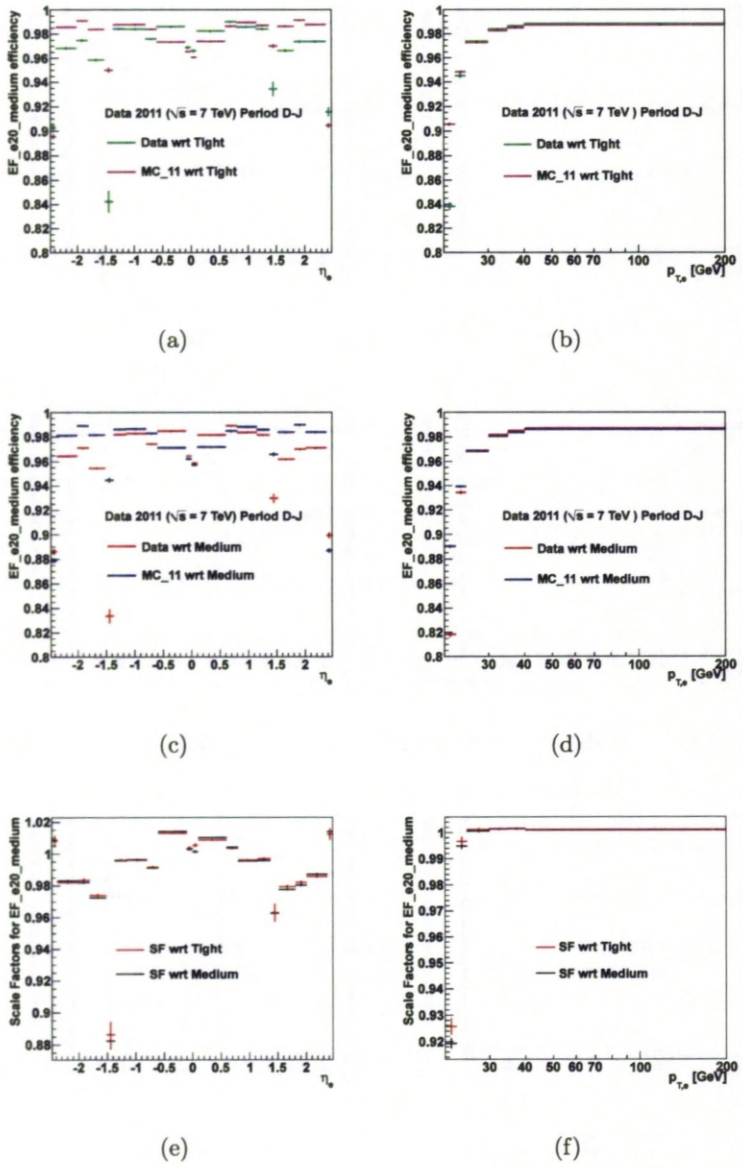

Figure 5.3: Trigger efficiency for `EF_e20_medium` *measured with* $Z/\gamma^* \rightarrow e^+e^-$ *Tag and Probe method, with respect to Medium (c-d) (evaluated by [81]) and Tight (a-b) (by author) offline electrons. Shown for electron pseudorapidity,* η*, and transverse momentum* p_{T}*. Also shown for Monte Carlo samples with resultant data/MC scale factors (e-f).*

efficiency towards the edges of acceptance (see Figure 5.3(e)). In particular, poor agreement is found for the crack region where the scale of the effect is not fully understood. This is however not a concern since $1.37 < |\eta| < 1.52$ is excluded for the measurement presented in this thesis.

Trigger Efficiency

The methodology described was used in the determination of the official e/γ trigger efficiency *data/MC* scale factor applied in the thesis. Around 2% of early data used for this analysis was collected with trigger `L1_EM14`, while the majority (98%) was collected with trigger `EF_e15_medium`. The efficiency was well modeled in Monte Carlo samples and a scale factor of $99.8\% \pm 0.2\%$ was determined. Only 2% of data were collected with `L1_EM14` which has an efficiency close to unity, therefore the final *data/MC* trigger efficiency correction was based on the remaining 98% of data. The subsequent `EF_e15_medium` trigger used applies Event Filter (*EF*) level *Medium* requirements and is seeded by `L1_EM10`. For electrons the efficiency of the L1 single electron trigger with its nominal threshold of 10 GeV was measured to be close to 100%. This was evaluated using minimum-bias data and samples obtained with lower-threshold electron triggers at lower luminosities [63]. At the *EF* level trigger has been measured to be $98.70 \pm 0.1\%$ efficient for a *Medium* electron above 20 GeV. Since, eventually `EF_e15_medium` defines the scale for the majority of the data analysis conducted in order to evaluate data/MC factors, to be used in the analysis, the same trigger selection was applied to simulated data. The resultant data/MC scale factors for this trigger has been estimated using $W \to e\nu_e$ and $Z/\gamma^* \to e^+e^-$ tag-and-probe [82], [83]. The plateau observed in the scale factor distributions in η and E_{T} for *Medium* and *Tight* electrons, after the $E_{\mathrm{T}} = 20$ GeVcut has been applied, allowed for an overall scale factor of $99.5 \pm 0.4\%$ to be assigned.

5.3.2 Electron reconstruction and identification efficiency

The efficiency *data/MC* scale factors used to correct the Monte Carlo samples in the following analysis are based on *Tag* and *Probe* methodology described in Section 5.3.1. In order to asses performance of the electron reconstruction and identification algorithms the accurate estimate derived from the data has to be calculated. In effect data from $Z/\gamma^* \rightarrow e^+e^-$ and $W \rightarrow e\nu_e$ decay channels have been used for this purpose [82,84]. The combined scale factors derived from *T&P* studies have smaller statistical uncertainties and present more robust result. Moreover these scale factors have the advantage of being easily incorporated in any physics analysis to correct the simulated data.

The basic reconstruction efficiency is defined as the probability for an electron that an electromagnetic cluster in the calorimeter is reconstructed in a fiducial region of the detector and is matched to a reconstructed track. This factor does not include losses of leptons due to imperfect regions of the detector within the geometrical acceptance. These losses are accounted for by the application of *OTX* maps. Electron reconstruction studies [82] indicated that the pure Monte Carlo efficiencies can be used i.e single scale factor of unity with a systematic uncertainty of 1.5%, thus flat across the electron pseudorapidity range. The systematic effect for the final result may by be fully accounted for by adding the uncertainty on the reconstruction efficiency in quadrature with to the total uncertainty on the identification efficiency scale factors. However, in order to detail the relative contributions the decision was made to quote them separately with the uncertainty band for reconstruction efficiency.

The efficiency of an electron to pass certain identification requirements i.e to be classified as *Loose*, *Medium* or *Tight* have been measured with data using W and Z *Tag* and *Probe* methods [82]. Despite slight differences of the η and E_{T} distributions for the electrons from W and Z the results were combined to yield

η	SF Loose	SF Medium	SF Tight
(-2.47 - -2.01)	0.976 ± 0.016	0.945 ± 0.017	0.925 ± 0.034
(-2.01 - -1.52)	0.990 ± 0.015	0.988 ± 0.016	0.995 ± 0.024
(-1.37 - -0.80)	0.982 ± 0.015	0.972 ± 0.016	1.006 ± 0.021
(-0.80 - 0.00)	0.991 ± 0.015	0.974 ± 0.015	0.982 ± 0.018
(0.00 - 0.80)	0.988 ± 0.015	0.972 ± 0.015	0.987 ± 0.018
(0.80 - 1.37)	0.982 ± 0.015	0.967 ± 0.015	1.033 ± 0.025
(1.52 - 2.01)	0.996 ± 0.015	0.995 ± 0.029	1.028 ± 0.045
(2.01 - 2.47)	0.974 ± 0.016	0.961 ± 0.017	0.936 ± 0.034

Table 5.3: Electron identification efficiency data/MC scale factors as a function of η , measured for probes within $20 < E_{\mathrm{T}} < 50\,\mathrm{GeV}$ [82, 85].

η dependent result for the suitable WZ energy range of 20-50 GeV. The results were further compared with the outcome from the Monte Carlo studies. The measurement was conducted in 8 η bins and the quoted errors include the combined statistical and systematic uncertainties. The dominant systematic uncertainties were related to the assumptions used to extract the efficiencies, the level of background in the sample, the choice of the discriminating variable, and the method used to subtract the background, as discussed in [82]. Recommended values of SF for electron identification efficiencies have been summarized in Table 5.3.

5.3.3 Electron energy calibration

The energy scale correction was determined [86] from data as a function η of the electron, by comparing the measured $Z/\gamma^* \rightarrow e^+e^-$ line shape to that predicted by the simulation. Additionally J/ψ and E/p measurements from $W \rightarrow e\nu_e$ events are used for a cross checks. The energy is scaled in data depending on the η of the electron, by applying the formula $E_{corr} = E_{meas}/(1+\alpha)$, where α is the correction factor and δE_{corr} denote the systematic uncertainty on the value of the corrected energy. The linearity in the electron energy have been tested by determining the correction factor α after applying the η-dependent calibration. The non-linearity was found to be less than 1% [84]. The summary of α factors is presented in Table 5.4.

cluster $\|\eta\|$	α	δE_{corr}
(0.0; 1.4)	-0.0096	1%
(1.4; 2.5)	0.0189	3%

Table 5.4: Recommendations for the electron energy scale correction.

5.4 Charge Identification

The accurate assessment of the electron charge translates directly to the precision of the $W^{\pm}$ boson charge separated cross section measurement, therefore it is important to study the charge mis-measurement probability. This is defined as a fraction of electrons with incorrectly measured charge, $N^{rec}_{q,wrong}$, with respect to all electrons $N^{rec}_{q,all}$:

$$\varepsilon_q^{misID} = \frac{N^{rec}_{q,wrong}}{N^{rec}_{q,all}}, \tag{5.3}$$

Depending on the requirements of the specific analysis ε_q^{misID} can be evaluated w.r.t. different cuts, as a function of the electron kinematic variables. For the purpose of cross section measurements the initial investigation was conducted using W and Z Monte Carlo truth information, since this provides high purity and large statistics samples. Figure 5.4 shows ε_q^{misID} distribution for W and Z bosons as a function on electron η and p_{T}. In this study the numerator of Equation 5.3 was defined by the number of reconstructed electrons matched to the truth level electrons within $\Delta R < 0.2$ and w.r.t. charge. As observed the charge misidentification, ε_q^{misID}, depends mainly on η_e of the electron with only small dependance on p_{T}. This is related to the increase of the amount of material traversed by the electrons in front of the calorimeter end-caps, i.e. early showering of the electrons (bremsstrahlung). The subsequent photon conversions produce a shower of secondary high p_{T} tracks, which can be further matched to the electromagnetic cluster in the calorimeter. This is also more probable for higher $|\eta|$ values, since the tracking worsens due to the limited coverage of TRT. In the case of electron p_{T}, the increase in the charge misidentifications probability towards higher values

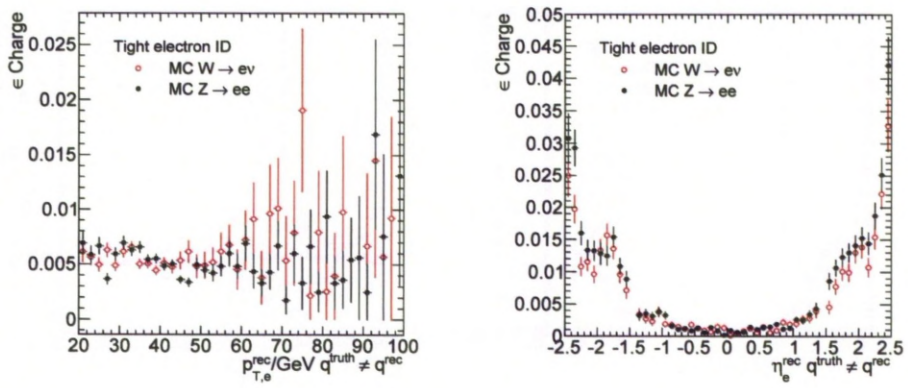

Figure 5.4: Comparison between charge misidentification probabilities, ε_q^{misID}, for electrons originating from $Z/\gamma^* \to e^+e^-$ and $W \to e\nu_e$. For Z candidate events final Z selection (see Section 5.3.1) (excluding opposite charge requirement) was applied, and final W selection in $W \to e\nu_e$ case. The results are obtained using the generated electron charge, matched to the reconstructed electrons within $\Delta R < 0.2$. A good agreement between W and Z samples as a function of η_e and also $p_{T,e}$ is observed.

is caused by reduced bending of the tracks. There is also small rise in ε_q^{misID} for low transverse momentum range due to electrons heavily showering within the volume of the detector, thus being reconstructed with relatively low p_{T} and, more likely, misidentified charge. No significant difference for the value of ε_q^{misID} in η_e or p_{T} between $W \to e\nu_e$ and $Z/\gamma^* \to e^+e^-$ electrons was observed, also when separated in charges.

The Monte Carlo studies provide an indication for the expected scale of ε_q^{misID}, it is important, however, to verify this estimate of the charge misidentification rate directly in data. This was conducted also recently [82, 84] using *Tag* and *Probe* methodology in $Z/\gamma^* \to e^+e^-$ events. In the study of ε_q^{misID} the ratio (see Equation 5.3) was formed by comparison between same-sign pairs and all (same-sign and opposite-sign) pairs, for several levels of electron identification including standard *Tight* electron ID, which forms direct input to the global and differential cross section analysis presented in this thesis. The specific require-

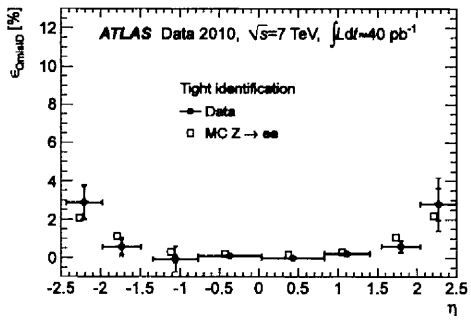

Figure 5.5: Electron charge misidentification probability, ε_q^{misID}, measured (T&P) on $Z/\gamma^* \rightarrow e^+e^-$ events, as a function of pseudorapidity, for electrons with $E_T > 20$ GeV, shown with respect to Tight offline selection. Data points are shown with statistical (inner error bars) and total uncertainties (outer error bars). The Monte Carlo expectation is indicated by open squares. For clarity, the data and Monte Carlo points are displaced horizontally in opposite directions [82, 84].

ments for the probe selection together with the background subtraction method used and related systematic effects are further discussed in [84]. The result for charge misidentification probability as a function electron η is presented in Figure 5.5. The overall good agreement between data and Monte Carlo estimate is observed, also when compared to the previous pure Monte Carlo level studies. The measured probability for charge misidentification ranges from $\sim 0.2\%$ in the barrel up to around 3% for the endcaps. The globally averaged ε_q^{misID} after *Tight* identification cut was equal to $0.37 \pm 0.07_{(syst.)} \pm 0.11_{(stat.)}$ (%) [84].

Chapter 6

Treatment of Background

The estimation of a background contamination to the $W \rightarrow e\nu_e$ decay channel is examined in this chapter. The background sources are listed and the mechanisms of how they contribute to the signal events passing the selection criteria are discussed. The emphasis is placed on the determination of contribution from jets faking electrons - the dominant component of the $W \rightarrow e\nu_e$ background.
It is feasible to group background sources into three main categories: real or fake electrons [1] plus missing transverse energy, produced by hadronic jet events, leptons from the decay of real W and Z (i.e from electroweak (EW) and $t\bar{t}$ decay channels) and leptons from cosmic rays. Cosmic-ray muons may on rare occasions fake real electrons in the detector [87], via combination of energy deposit in the electromagnetic calorimeter, either by direct ionization in the detector material or bremsstrahlung radiation, and the track pointing to it. The event has to coincide in time with the bunch crossing, with the lepton track passing near the beam spot. Its rather sporadic occurrence and the fact that effect does not scale with luminosity, allowed for exclusion from further consideration.
Di-bosons processes with WW, WZ or ZZ in the final state, have a relatively small cross-section and overall contribution of $< 0.1\%$ which is negligible.

[1] The term electron will be used in general to describe both the electron e^- and its anti-particle e^+, unless the charge is specifically mentioned

6.1 EW and $t\bar{t}$ background

The model of electroweak background to $W \to e\nu_e$ channel, derived from Monte Carlo Data sets, was assumed to be correct for the purpose of this analysis. The systematic uncertainties on the cross sections for the eletroweak processes considered were estimated at 5% level [63] and 6% for $t\bar{t}$ [63] i.e. the uncertainty on any event count prediction normalized using these cross sections. These uncertainties are primarily related with the choice of PDF sets. The following events account for sources of EW and $t\bar{t}$ background to $W \to e\nu_e$ channel:

$W \to \tau\nu_\tau$

This is the largest electroweak background in the $W \to e\nu_e$ channel. Having the same production rate as a signal, involving true missing transverse energy from neutrinos and real electron in 18% of cases coming from τ decay, makes it difficult to suppress. Nevertheless, due to the three body final state signature of $\tau \to e\nu_e\nu_\tau$, electrons share the τ momentum and generally have smaller p_{T} than signal electrons. This is clearly visible in Table 5.2 where suppression is achieved by trigger requirement of a single *Medium* electron with $p_{\mathrm{T}} > 15\,\mathrm{GeV}$ (77% relative suppression) and subsequently by $E_T > 20\,\mathrm{GeV}$ cut (36%). $\not{E}_{\mathrm{T}} > 25\,\mathrm{GeV}$ requirement provides 45% reduction and $m_{\mathrm{T}} > 40\,\mathrm{GeV}$ cut reduce the channel by another 13%. Relative contribution to the final number of all $W^{\pm}$ candidate events is at the level of 2.4%.

$t\bar{t}$ final state

The top quark decay leads predominantly to W and bottom quark final state. Therefore genuine Ws from $t\bar{t}$ are accompanied by hadronic b-jets. Single W's will decay hadronically 2/3 of the time giving rise to two jets from $W \to q\bar{q}'$ and 1/3 of the time leptonically, $W \to l\nu_l$. Consequently, for the $t\bar{t}$ pair, there are three main production signatures:

- 4/9 of the time both Ws decay hadronically resulting in six jets and no leptons in a final state,
- in 4/9 of cases Ws from $t \to Wb$ produce a mixture of hadronic and leptonic final states, with one lepton, one neutrino and four jets
- the remaining 1/9 of $t\bar{t}$ decays, fully leptonic final states from both Ws produce two leptons, two neutrinos and two b-jets

The small relative cross section for $t\bar{t}$ production and for a jet to fake an electron should allow for the exclusion of the fully hadronic modes at the trigger stage. In Monte Carlo pure hadronic final states $t\bar{t}$ events are removed from simulation by the generator filter imposed at the generator level (see Table 4.1), therefore 59% suppression at the trigger level relates to low p_{T} electrons, similarly as observed in $W \to \tau\nu_{\tau}$. Further reduction in a background contamination is achieved by transverse momentum and $\not{E}_{\mathrm{T}}$ requirements, with relative efficiency of up to 20%. The resultant background from $t\bar{t}$ is determined to be 0.4%.

$Z/\gamma^* \to e^+e^-$

The relative efficiency of a subsequent selection cuts (see Table 5.2), show that electrons from $Z/\gamma^* \to e^+e^-$ are not sensitive to most of the applied criteria, thus they kinematically resemble signal - a consequence of both W and Z being close in mass and having similar production mechanisms. $Z/\gamma^* \to e^+e^-$ will mimic $W \to e\nu_{\mathrm{e}}$ if one of the electrons from Z decay fails the acceptance criteria and there is an associated large amount of fake missing transverse energy in the event. The fake $\not{E}_{\mathrm{T}}$ may arise from mis-measured jet or if one of the electrons escaped the detector i.e. falling into a crack region, but this is less likely due to the coverage of the $ATLAS$ calorimeters. Therefore the suppression of $Z/\gamma^* \to e^+e^-$ is mainly achieved by imposing $Z_v eto$ on the second $Medium$ electron in the event (68%) and subsequently by 96% due to $\not{E}_{\mathrm{T}} > 25\,\mathrm{GeV}$ requirement. Remaining events account for 0.2% of selected $W^{\pm}$ candidates.

$Z/\gamma^* \to \tau^+\tau^-$

Similarly to $W \to \tau\nu_\tau$, $Z/\gamma^* \to \tau^+\tau^-$ can mimic $W \to e\nu_e$ when a τ decays leptonically into an electron. Despite having a smaller production rate for a single electron in a final state compared to $Z/\gamma^* \to e^+e^-$, larger true $\not{E}_{\mathrm{T}}$ from the presence of neutrinos in $Z/\gamma^* \to \tau^+\tau^-$ accounts for a comparable contribution of 0.2% to the final number of selected $W^\pm$ candidates. As was the case for $W \to \tau\nu_\tau$, the trigger choice reduces this channel to 25% of the trigger input, which leaves mainly electrons from τs. Discriminating primary electrons from those of leptonic τ decay origin is difficult. $Z_v eto$ is not really effective, since it helps only when both τs decay to electrons, thus in 3.2% of cases. Again, the strongest suppression comes from the transverse momentum requirement, namely $E_T^{clus} > 20\,\mathrm{GeV}$ cut (32% suppression) and well placed missing transverse energy cut rejecting low energy neutrinos (74%). Final $m_{\mathrm{T}} > 40\,\mathrm{GeV}$ reduces $Z/\gamma^* \to \tau^+\tau^-$ by 37%.

The sum of EW and $t\bar{t}$ backgrounds are found to be 3.2% for the $W^\pm$, 3.4% in W^- and 3% in W^+ channel of the respective numbers of selected W candidates. Table 6.1 presents the summary of $EW + t\bar{t}$ background contribution to the $W \to e\nu_e$ channel.

6.2 QCD Background

Multi-jet events produced in QCD interactions are the dominant source of fake electrons (i.e. jets mis-reconstructed as electrons) and fake missing transverse energy (i.e. due to detector inefficiencies and resolution). Although the probability that a jet is misidentified as an electron is small, the enormous production rate of the QCD events at the LHC, when compared to the $W \to e\nu_e$, makes it the dominant source of background. Its determination with data is most suitable because of the limited theoretical understanding of how the partons hadronise and fragment into jets together with uncertainties on multijet production. Contributions

η	$W^{\pm}_{(stat)\pm(syst)}$	$W^{+}_{(stat)\pm(syst)}$	$W^{-}_{(stat)\pm(syst)}$
(-2.47 - -2.01)	267 ± 10 ± 14	165 ± 8 ± 9	102 ± 6 ± 5
(-2.01 - -1.52)	317 ± 10 ± 16	181 ± 8 ± 9	135 ± 7 ± 7
(-1.52 - -1.37)			
(-1.37 - -0.8)	439 ± 12 ± 23	233 ± 9 ± 12	206 ± 8 ± 11
(-0.8 - 0)	720 ± 15 ± 37	391 ± 11 ± 20	329 ± 10 ± 17
(0 - 0.8)	804 ± 16 ± 42	440 ± 12 ± 23	364 ± 11 ± 19
(0.8 - 1.37)	495 ± 13 ± 26	278 ± 10 ± 14	217 ± 9 ± 11
(1.37 - 1.52)			
(1.52 - 2.01)	339 ± 11 ± 18	200 ± 9 ± 10	139 ± 7 ± 7
(2.01 - 2.47)	240 ± 9 ± 12	150 ± 7 ± 8	90 ± 5 ± 5
(-2.47 - 2.47)	3621 ± 35 ± 73	2038 ± 26 ± 40	1583 ± 23 ± 32

Table 6.1: Sum of electroweak $EW + t\bar{t}$ background to $W \to e\nu_e$ channel along the electron pseudorapidity range η. The contribution to the observed number of W boson events after final W selection is at the level of 3%. The uncertainties are due to statistical and systematics weights. 5% systematic uncertainty arise from a choice of $PDFs$.

from the underlying event and multiple interactions (pile-up) are further uncertainties. In addition the low electron fake rate and large QCD jets cross section make it difficult to produce Monte Carlo event sets with the desired statistics.

6.2.1 Data-driven QCD background estimation

In order to perform the calculation of the differential cross section a reliable QCD background modeling has to be conducted.

In the following analysis the method, termed $ABCD$, is used which allows for the estimation of the QCD background contribution directly from the data. The method to obtain QCD template is commonly used and may be found in several analyses [63, 88–94]

The $ABCD$ method used here relies on the choice of the two-dimensional phase space of mutually independent discriminant variables, which define 3 control background dominated regions and one signal dominated region (see Figure 6.1). To implement the method, however, several studies are needed in order to determine and validate a suitable set of variables. The boundaries of the control regions should be chosen to minimize the leakage of the signal into the background re-

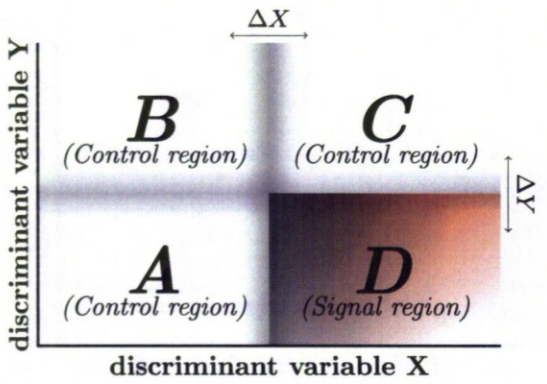

Figure 6.1: Schematic representation of ABCD regions formed by a set $\{X, Y\}$ of independent variables. The correct choice of the discriminating variables ensures that QCD distributions enclosed by background dominated control regions (A,B,C) provide unbiased feed for the data driven QCD model in the signal region (D).

gions as well as to limit possible correlations for the number of fake electrons arising from mis-reconstructed QCD events. Therefore, if the QCD events distribution may be described (i.e. factorized) by a set $\{X, Y\}$ of mutually independent variables, then a consequence will be conservation of the following relation:

$$\frac{N_A}{N_D} = \frac{N_A + N_B}{N_C + N_D} \quad \left(\Longleftrightarrow \frac{N_A}{N_B} = \frac{N_A + N_D}{N_B + N_C} \right) \qquad \forall\, i \in \{A, B, C, D\} : i \neq \emptyset, \tag{6.1}$$

which can be rewritten:

$$\frac{N_A}{N_B} = \frac{N_D}{N_C} \tag{6.2}$$

where N_i is the integrated number of events in a given region of phase space.

Equation 6.1 provides a systematic handle for searches of the correct set of discriminant variables and also a probe of potential correlations between them. The procedure is: to first introduce values for a chosen set $\{X, Y\}$, i.e define the boundaries of $ABCD$, and next to asses the ratio for a given slice w.r.t. one of the discriminating variables. E.g. ratio $\frac{N_A}{N_D}$ ($\frac{N_A}{N_B}$) for the slice lying below the value of Y (X). Finally we remove variable Y (X) and evaluate $\frac{N_A+N_B}{N_C+N_D}$ ($\frac{N_A+N_D}{N_B+N_C}$).

If both relations give the same result the variables may be regarded as being uncorrelated. If this is not the case for a given set of $\{X, Y\}$ we can try to limit a possible correlation by redefinition of $ABCD$ phase space into the one for which Equation 6.1 holds i.e shifting initial boundaries by ΔY (ΔX). Moreover, in the same manner, we may exclude some regions of phase space, introducing gaps between $ABCD$ regions, if this is more suitable for the final analysis.
It is essential for the above assessment to conduct it also in terms of the agreement between the shapes of the respective distributions enclosed within $ABCD$ and not only integrated number of events, therefore confirming the plausibility of $ABCD$ result.

In the following analysis the choice was made to use a calorimetric energy isolation variable $E_{\mathrm{T}}^{cone}(R_0)$ (see Equation 6.3) of the electron candidate and transverse mass (see Equation 2.7) of the resulting W boson, in order to construct $ABCD$ regions. $E_{\mathrm{T}}^{cone}(R_0)$ is defined as the amount of reconstructed energy in a cone of a half opening angle R_0 around the electron candidate direction, with the exclusion of the energy from the given electron candidate corresponding to cluster size of $\Delta\eta \times \Delta\phi = 5 \times 7$ cells

$$E_{\mathrm{T}}^{cone}(R_0) = \left(\sum_{cells:\ \Delta R < R_0} E_T(cell) \right) - E_T(5 \times 7\ cells), \tag{6.3}$$

The $E_{\mathrm{T}}^{cone}(R_0)$ and m_{T} variables are strong signal discriminators. In addition $E_{\mathrm{T}}^{cone}(R_0)$ explore a global property of an event, where m_{T} is a local property of an electron, therefore they are assumed to be uncorrelated. Equation 6.3 is a consequence of a general observation that jets faking electrons produce much larger hadronic activity around the candidate due to accompanying particles when compared to real electrons, which deposit energy in a narrow cluster. The amount of transverse energy deposited in cells around the electron candidate cluster gives a handle to distinguish signal electrons from hadronic background. The subsequent studies revealed that selection of $E_{\mathrm{T}}^{cone}(0.3)$ is the most optimal with regards to

correlation and performance. It is worth mentioning, that initially a set of the discriminant variables was defined as $\{\not\!\!E_{\mathrm{T}}, E_{\mathrm{T}}^{cone}\}$. It was confirmed however that the assumption regarding this set as uncorrelated was invalid. There was a class of events observed mainly for lower range of missing transverse energy spectrum (i.e. $\not\!\!E_{\mathrm{T}} < 25\mathrm{GeV}$) with E_{T} deposits above 20GeV and low isolation values for which subsequent signal and $EW + t\bar{t}$ removal was ineffective, resulting in bias to the estimated QCD distribution. The probable origin was classified as being due the underlying event (soft particles). They were mostly excluded by replacing $\not\!\!E_{\mathrm{T}}$ with m_{T} and conducting assessment for $\not\!\!E_{\mathrm{T}} > 25\mathrm{GeV}$.

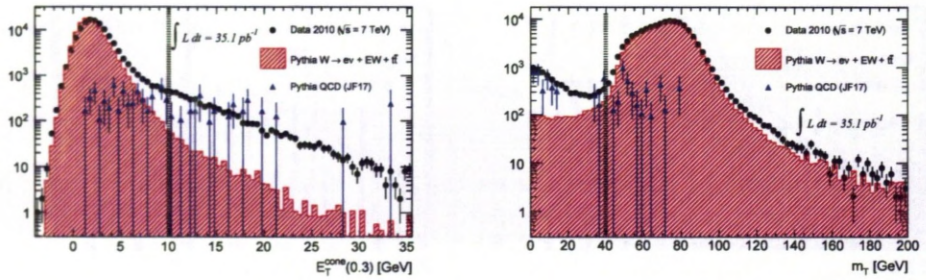

(a) (b)

Figure 6.2: Isolation E_{T}^{cone} and m_{T} distributions seen in DATA and modeled by Monte Carlo. Shape from Pythia ($JF17$) is significantly different from the signal and remaining electroweak (EW) sources of contamination.

As can be seen in Figure 6.2 the isolation and transverse mass distributions for electron candidates originating from multijet events are significantly different in shape compared to electrons from $W \to e\nu_e$ events. This allows for the separation of the two dimensional E_{T}^{cone} vs. m_{T} space into four mutually exclusive intervals of low and high isolation and transverse mass, leading to three kinematic regions enriched in fake electrons of jet origin and one corresponding to the signal region.

In this study, the following four regions of $ABCD$ were chosen:

- Region A (control):

  electron candidates satisfying $E_{\mathrm{T}}^{cone}(0.3) < 10$ GeV and $m_{\mathrm{T}} \leq 40$ GeV

$\|\eta\|$	(0.00; 0.80)	(0.80; 1.37)	(1.37; 1.52)	(1.52; 2.01)	(2.01; 2.47)

Table 6.2: Granularity for electron candidate pseudorapidity distribution of final differential W cross-section measurement, shown for absolute range, $|\eta|$.

- Region B (control):
  electron candidates satisfying $E_{\mathrm{T}}^{cone}(0.3) \geq 10$ GeV and $m_{\mathrm{T}} \leq 40$ GeV
- Region C (control):
  electron candidates satisfying $E_{\mathrm{T}}^{cone}(0.3) \geq 10$ GeV and $m_{\mathrm{T}} > 40$ GeV
- Region D (signal):
  electron candidates satisfying $E_{\mathrm{T}}^{cone}(0.3) < 10$ GeV and $m_{\mathrm{T}} > 40$ GeV

To implement the method which discriminates the QCD background, a two dimensional plot of "E_T^{cone} *vs* m_T" (see Figure 6.3) is produced for all electron candidates that pass final W boson selection, described in Chapter 5, except for the m_{T} and E_{T}^{cone} requirement. The plot is separated into four regions, denoted A, B, C, D. Slices A, B and C are dominated by QCD events and their boundaries are selected so as to avoid signal contamination and variable correlation. In contrast, the signal region D is dominated by isolated electron candidates that occur in events with high m_{T} threshold, therefore those are mainly W events. The topology of the events for each $ABCD$ region is summarized in the Table 6.3.

The distribution for the QCD background events in the signal region is estimated from the shapes of observed events in all three background dominated regions. The approach differs from the commonly used variant of $ABCD$, where the shape of the background derived from the region(s) of choice is scaled by the integrated number of events enclosed within remaining region(s). Here, also the scaling is conducted differentially for each bin of electron pseudorapidity η, to obtain the background for the differential analysis. The binning is adopted accordingly to the granularity of final cross section measurement (see Table 6.2).

As can be seen in Figure 6.3 there is some signal contamination in the A,B

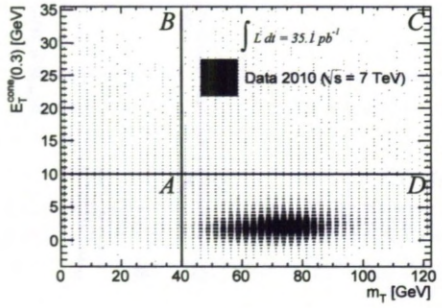

(a)

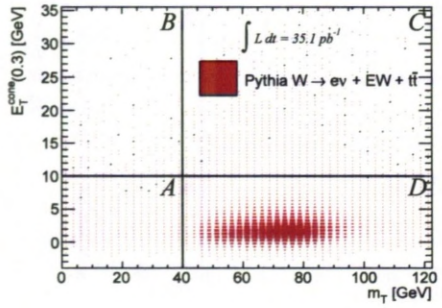

(b)

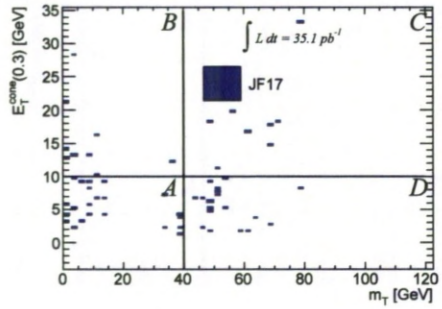

(c)

Figure 6.3: m_T vs isolation for electron candidates passing final W boson selection cuts except for $m_T > 40\,GeV$ and $E_T^{cone}(0.3) < 10\,GeV$. Lines denote the boundaries of the $ABCD$ regions. Shown for (a) data, (b) sum of signal, EW and $t\bar{t}$ and (c) $JF17$ samples. The area of boxes is proportional to the event yield. Monte Carlo samples are scaled to the data luminosity of $35\,pb^{-1}$ for this plot.

and C quadrants which will bias the QCD estimate. The effect is most significant in regions A and C (see Table 6.3), where the number of signal events, N^{SIG}, and number of background events, $N^{EW+t\bar{t}}$, combined account for $\sim$ 33% and $\sim$ 13% of contained data, respectively. Removal of signal events, along with other electroweak (EW) contributions, from the regions in which the estimate is made is discussed in Section 6.2.2

In order to confirm whether $ABCD$ defines four independent regions, initial validation of the method was conducted on a sample of QCD events from the standard $JF17$ Monte Carlo. Apart from the most common hard processes, di-jets and photon+jet processes, the *Pythia* dataset contains W, Z and $t\bar{t}$ events. Therefore, to select a pure QCD Monte Carlo sample, any events identified by the generator process ID to be genuine W, Z or $t\bar{t}$ production were discarded. The distribution of events among $ABDC$ regions is shown in Table 6.4. The statistics of the $JF17$ sample represents only $0.1\,pb^{-1}$. Despite the small number of events the assumption of the method (see Equation 6.2) was checked, also differentially in electron η. Furthermore, to increase statistics i.e. probing sensitivity additional complementary ratios $(N_A + N_D)/(N_B + N_C)$ and $(N_A + N_B)/(N_D + N_C)$.

$$\frac{N_A}{N_B} = 2.34 \pm 0.96 \qquad \frac{N_D}{N_C} = 1.73 \pm 0.73 \qquad \frac{N_A + N_D}{N_B + N_C} = 2.03 \pm 0.58$$
$$\frac{N_A}{N_D} = 1.25 \pm 0.40 \qquad \frac{N_B}{N_C} = 0.93 \pm 0.46 \qquad \frac{N_A + N_B}{N_C + N_D} = 1.13 \pm 0.31$$

From the inspection of Table 6.4 it follows that any assessment conducted differentially in $|\eta|$ will be subject to large statistical uncertainties, due to limited statistics available, therefore difficult to interpret. It is most apparent in regions B and C with 100% uncertainty for the middle $|\eta|$ bins, and only marginally improved by the evaluation of complementary ratios (see Figure 6.4).

As a conclusion, there was an indication, albeit within large statistical uncertainty, that the choice of the boundaries for the $ABCD$ method was correct.

(a) $W \to e\nu_e$

	N_A	N_B	N_C	N_D
DATA	5164	2239	2750	114047
$W \to e\nu_e$	1100.98 ± 20.97	6.67 ± 1.67	345.93 ± 11.54	106492.14 ± 206.46
$W \to \tau\nu_\tau$	403.80 ± 12.56	1.93 ± 0.91	9.30 ± 2.00	2822.00 ± 33.47
$t\bar{t}$	86.21 ± 1.55	3.60 ± 0.31	17.25 ± 0.70	406.41 ± 3.40
$Z/\gamma^* \to e^+e^-$	16.42 ± 0.69	0.09 ± 0.05	1.98 ± 0.27	205.76 ± 2.70
$Z/\gamma^* \to \tau^+\tau^-$	107.88 ± 6.23	0.00 ± 0.00	0.21 ± 0.21	186.79 ± 8.25

(b) $W^+ \to e^+\nu_e$

	N_A	N_B	N_C	N_D
DATA	2731	1127	1454	67941
$W^+ \to e^+\nu_e$	723.46 ± 17.04	5.87 ± 1.60	198.89 ± 8.70	62651.26 ± 158.40
$W^+ \to \tau^+\nu_\tau$	271.50 ± 10.28	0.67 ± 0.48	5.62 ± 1.53	1635.52 ± 25.47
$t\bar{t}$	42.43 ± 1.09	1.80 ± 0.22	8.33 ± 0.49	200.68 ± 2.40
$Z/\gamma^* \to e^+e^-$	8.44 ± 0.51	0.06 ± 0.04	0.87 ± 0.18	106.75 ± 1.95
$Z/\gamma^* \to \tau^+\tau^-$	56.40 ± 4.46	0.00 ± 0.00	0.21 ± 0.21	94.84 ± 5.92

(c) $W^- \to e^-\bar{\nu}_e$

	N_A	N_B	N_C	N_D
DATA	2433	1112	1296	46106
$W^- \to e^-\bar{\nu}_e$	377.52 ± 12.22	0.80 ± 0.47	147.04 ± 7.58	43840.88 ± 132.42
$W \to \tau^-\bar{\nu}_\tau$	132.30 ± 7.22	1.26 ± 0.78	3.68 ± 1.29	1186.48 ± 21.72
$t\bar{t}$	43.78 ± 1.09	1.80 ± 0.23	8.91 ± 0.50	205.72 ± 2.41
$Z/\gamma^* \to e^+e^-$	7.98 ± 0.47	0.03 ± 0.03	1.11 ± 0.20	99.01 ± 1.87
$Z/\gamma^* \to \tau^+\tau^-$	51.49 ± 4.34	0.00 ± 0.00	0.00 ± 0.00	91.95 ± 5.76

Table 6.3: The observed number of $W^\pm$ events in four regions of $ABCD$ plane for the data-driven estimation of QCD background, together with the Monte Carlo estimates for the number of signal N^{SIG} and background $N^{EW+t\bar{t}}$ events. Monte Carlo based predictions are normalized to the measurement luminosity $L = 35.1\,pb^{-1}$ and corrected for trigger, reconstruction efficiency scale factors and for pile-up re-weighting. Data are calibrated according to the energy scale correction. The uncertainties are due to statistical weights only.

$\|\eta\|$	N_A	N_B	N_C	N_D
(0-0.8)	7.61±2.73	6.18±2.62	1.97±1.41	2.83±1.65
(0.8-1.37)	7.46±2.54	1.77±1.29	0.72±0.72	5.76±2.21
(1.37-1.52)				
(1.52-2.01)	3.53±1.82	0.65±0.65	4.06±2.06	4.32±2.27
(2.01-2.47)	1.49±1.07	0.00±0.00	2.49±1.84	3.12±1.61
(0-2.47)	20.09 ± 4.29	8.59 ± 2.99	9.24 ± 3.18	16.03 ± 3.92

Table 6.4: Distribution of $JF17$ events in $ABCD$ regions.

The differential assessment was much more difficult, nevertheless in terms of the shape of the η distribution, the relations remained conserved. It is clear that large statistical uncertainties, did not allow the formal exclusion of a possible correlation between isolation and transverse mass at this stage. A potential correlation would bias the data driven prediction of the QCD distribution, therefore, the estimate for the effect is conducted in a later section dedicated to the systematic uncertainties of the method.

The simple comparison between number the of QCD events counted directly in a signal region (D) and estimated using the other three regions, results in a consistency within $\sim 53\%$ uncertainty:

$$N_D = 16.03 \pm 3.92 \qquad \frac{N_A}{N_B} \times N_C = 21.62 \pm 11.55$$

here the scaling to the measurement luminosity was not applied.

It is worth mentioning, that to increase the statistical significance of the $JF17$ sample also when differentiated in charge, symmetrization of the events was performed. The assumption that in principle jet distribution should be independent of charge selection, allowed for the weighting to be applied, namely for W^+ and W^- both charges, N_{e-} and N_{e+} were summed with a weight of 1/2 each, to preserve the general normalization ($N_{W+} = N_{W-} \rightarrow 0.5N_{e-} + 0.5N_{e+}$). Therefore, any charge related biases due to low statistics were limited. As a result of this procedure, the number of events in the case of W^+ selection matched those from W^-.

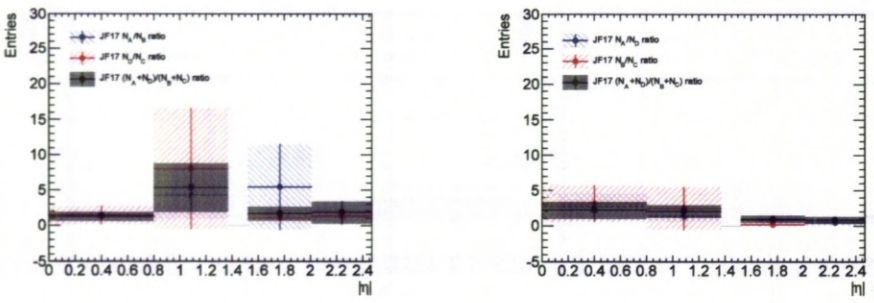

(a) (b)

Figure 6.4: Control ratios for the $JF17$ sample in terms of lepton $|\eta|$.

6.2.2 Electroweak removal

Although it was indicated with $JF17$ sample that in the case of jets faking electrons the discriminant variables are not heavily correlated, therefore the regions may be regarded as independent, it is no longer the case for signal, electroweak and $t\bar{t}$ distributions. From the expected numbers of N^{SIG} and $N^{EW+t\bar{t}}$ events, in each $ABCD$ region (see Table 6.3) it follows that for these contributions the Equation 6.2 does not hold. Therefore to avoid bias in the number of QCD events, signal, electroweak and $t\bar{t}$ components were removed from the $ABCD$ regions using Monte Carlo predictions. The normalisation of the $W \to e\nu_e$ and $EW + t\bar{t}$ samples to the data luminosity is fixed on the basis of their predicted cross sections.

Allowing for Equation 6.2 to be expressed in terms of the number of QCD events, N^{QCD}, the η differential estimate for the QCD background in the signal region, $N_D^{QCD}(\eta)$, can be stated as:

$$N_D^{QCD}(\eta) = \frac{N_A^{QCD}(\eta)}{N_B^{QCD}(\eta)} \times N_C^{QCD}(\eta), \tag{6.4}$$

Subtraction of the electroweak and $t\bar{t}$ components (Equation 6.6) requires enough statistics, therefore a variant of the common $ABCD$ method is used to

avoid a systematic effect due to the luminosity measurement.

$$c_i(\eta) = \frac{N_i^{SIG}(\eta) + N_i^{EW+t\bar{t}}(\eta)}{N_D^{SIG}(\eta) + N_D^{EW+t\bar{t}}(\eta)}, \qquad i = A, B, C \tag{6.5}$$

In this approach Monte Carlo components in the signal (D) region are used to get the correct normalization for the amount of N^{SIG} and $N^{EW+t\bar{t}}$ leakage into the control regions (see Equation 6.5 and Table A.1).

$$N_i^{QCD}(\eta) = N_i^{DATA}(\eta) - (N_i^{SIG}(\eta) + N_i^{EW+t\bar{t}}(\eta)) = \tag{6.6}$$

$$= N_i^{DATA}(\eta) - c_i(\eta) \cdot \underbrace{(N_D^{SIG}(\eta) + N_D^{EW+t\bar{t}}(\eta))}_{N_D^{DATA}(\eta) - N_D^{QCD}(\eta)}, \tag{6.7}$$

where $N_i^{DATA}(\eta) = N_i(\eta)$ represents the number of observed events in region i ($i = A$, B, or C).

Using Equation 6.7, the $ABCD$ relations is represented by the formula:

$$N_D^{QCD}(\eta) = \frac{N_A(\eta) - c_A(\eta) \cdot (N_D(\eta) - N_D^{QCD}(\eta))}{N_B(\eta) - c_B(\eta) \cdot (N_D(\eta) - N_D^{QCD}(\eta))} \times \\ \times (N_C(\eta) - c_C(\eta) \cdot (N_D(\eta) - N_D^{QCD}(\eta))), \tag{6.8}$$

This quadratic equation in $N_D^{QCD}(\eta)$ has to be solved for each η bin. The two roots, $N_D^{QCD}(\eta)(1)$ and $N_D^{QCD}(\eta)(2)$ are found expressing Equation 6.8 as:

$$a(\eta)(N_D^{QCD}(\eta))^2 + b(\eta)N_D^{QCD}(\eta) + k(\eta) = 0, \tag{6.9}$$

where a, b and k are constants:

$$a(\eta) = c_B(\eta) - c_A(\eta) \cdot c_C(\eta),$$

$$b(\eta) = N_B(\eta) - c_A(\eta) \cdot N_C(\eta) - c_B(\eta) \cdot N_D(\eta) - \\ - c_C(\eta) \cdot N_A(\eta) + 2 \cdot c_A(\eta) \cdot c_C(\eta) \cdot N_D(\eta),$$

$$k(\eta) = c_A(\eta) \cdot N_D(\eta) \cdot N_C(\eta) + c_C(\eta) \cdot N_D(\eta) \cdot N_A(\eta) - \\ - c_A(\eta) \cdot c_C(\eta) \cdot (N_D(\eta))^2 - N_A(\eta) \cdot N_C(\eta),$$

η	$W^{\pm}_{(stat)\pm(syst)}$	$W^{+}_{(stat)\pm(syst)}$	$W^{-}_{(stat)\pm(syst)}$
(-2.47 - -2.01)	949 ± 166 ± 285	617 ± 153 ± 185	359 ± 89 ± 108
(-2.01 - -1.52)	436 ± 60 ± 131	202 ± 40 ± 61	238 ± 47 ± 71
(-1.52 - -1.37)			
(-1.37 - -0.8)	435 ± 45 ± 131	205 ± 32 ± 62	224 ± 32 ± 67
(-0.8 - 0)	484 ± 44 ± 145	216 ± 29 ± 65	265 ± 33 ± 79
(0 - 0.8)	509 ± 44 ± 153	234 ± 30 ± 70	274 ± 32 ± 82
(0.8 - 1.37)	523 ± 50 ± 157	278 ± 39 ± 83	244 ± 32 ± 73
(1.37 - 1.52)			
(1.52 - 2.01)	341 ± 44 ± 102	152 ± 29 ± 46	191 ± 34 ± 57
(2.01 - 2.47)	561 ± 97 ± 168	228 ± 59 ± 69	333 ± 79 ± 100
(-2.47 - 2.47)	4239 ± 226 ± 1272	2134 ± 183 ± 640	2126 ± 147 ± 638

Table 6.5: The charge dependent estimate of the number of QCD events in the signal region (D), N_D^{QCD} for each lepton pseudorapidity bin, η. The uncertainties are statistical and systematic (30%) in that order.

The two explicit solutions, $N_D^{QCD}(\eta)(1)/(2)$, follows:

$$a(\eta) \cdot (N_D^{QCD}(\eta) - N_D^{QCD}(\eta)(1)) \cdot (N_D^{QCD}(\eta) - N_D^{QCD}(\eta)(2)) = 0, \tag{6.10}$$

where

$$N_D^{QCD}(\eta)(1)/(2) = \frac{-b(\eta) \pm \sqrt{b(\eta)^2 - 4 \cdot a(\eta) \cdot k(\eta)}}{2 \cdot a(\eta)}. \tag{6.11}$$

The inputs for the (Equation 6.8) have been presented in Table A.2 - Table A.4 differentially per lepton η bin. Table 6.5 presents the solutions to the quadratic polynomial for N_D^{QCD} differentially and integrated in η.

6.2.3 Correlation of the Isolation parameter and m_{T}

As already indicated the possibility of a correlation between the discriminant variables would bias the QCD template derived from the data. Consequently further investigation was needed to assess the plausibility of the $ABCD$ method and derive related systematic uncertainties. This was done on $JF17$ Monte Carlo sample. The initial assumption regarding E_{T}^{cone} and m_{T} as uncorrelated was scrutinized by comparing E_{T}^{cone} in ranges of m_{T} and equivalently $m_{\mathrm{T}}(E_{\mathrm{T}}^{cone})$. The shape comparison of the respective distributions, in the specific regions of $ABCD$,

allow us to differentiate the scale and trend of any bias with fine granularity of the chosen binning. In order to quantify whether the isolation (m_{T}) distributions are consistent in each m_{T} (E_{T}^{cone}) region, ratios between respective distributions normalized to the same area, were performed (see Figure 6.5). Additionally the ratios for a different acceptance requirements were investigated to establish whether the correlation between discriminant variables was a leading effect. Two sets of cuts where used in this study:

- *Tight* set:
  - Preselection
  - *Tight* electron ID
- $Medium + \not{E}_{\mathrm{T}}$ set:
  - Preselection
  - *Medium* electron ID
  - Missing transverse energy $\not{E}_{\mathrm{T}} > 25$ GeV

For *Tight* set $\not{E}_{\mathrm{T}} > 25$ GeV requirement was not included in order to provide significant statistics. It is worth mentioning that the choice of *Medium* electron ID implies the change of respective data/MC scale factors. We observe that the shapes of the distributions depends on the choice of isolation and W transverse mass slices, which implies general correlation between discriminant variables. Subsequent efficiency requirements do not interfere strongly with the overall correlation pattern between m_{T} an E_{T}^{cone}. This is visible in the overall agreement between the ratios of electron ID shapes. Therefore the choice was made to relax ID of an electron for $\not{E}_{\mathrm{T}} > 25\,\mathrm{GeV}$ allowing in principle to mimic the final $ABCD$ plane as accurately as possible with $JF17$. Gained statistical sensitivity of $JF17$ for of $Medium + \not{E}_{\mathrm{T}}$ selection, revealed that there was no statistically significant alternation to the initial correlation pattern, despite the

	N_A	N_B	N_C	N_D
$W^{+/-}$	47.55 ± 6.52	24.36 ± 5.15	45.85 ± 6.70	117.35 ± 10.32

Table 6.6: Distribution of jet events from $JF17$ sample in $ABCD$ regions with relaxed electron ID identification requirement.

functional dependance of m_{T} on $\not{E}_{\mathrm{T}}$ clearly visible in the shape of transverse mass distribution for the region of $\not{E}_{\mathrm{T}} > 25\,\mathrm{GeV}$.

The above analysis leads to the conclusion that it is safe to estimate the systematic uncertainty of the method arising from the correlation between discriminant variables, using final W selection with relaxed electron ID requirement ($Tight \rightarrow Medium$).

Systematics

The nature of a correlation between m_{T} and E_{T}^{cone} is not uniform, therefore to estimate a systematic effect on the QCD data driven template i.e. impact on the final cross-section measurement, it is necessary to repeat the closure test of $ABCD$ with $JF17$ for relaxed electron ID sample.

$$\frac{N_A}{N_B} = 1.95 \pm 0.49 \qquad \frac{N_D}{N_C} = 2.56 \pm 0.44 \qquad \frac{N_A + N_D}{N_B + N_C} = 2.35 \pm 0.33$$
$$\frac{N_A}{N_D} = 0.41 \pm 0.07 \qquad \frac{N_B}{N_C} = 0.53 \pm 0.14 \qquad \frac{N_A + N_B}{N_C + N_D} = 0.44 \pm 0.06$$

The comparison between the number of QCD events counted directly in a signal region (D) and estimated using the other three regions of $ABCD$, revealed consistency within $\sim 31\%$ uncertainty:

$$N_D = 117.35 \pm 10.32 \qquad \frac{N_A}{N_B} \times N_C = 89.50 \pm 26.07$$

here the scaling to the measurement luminosity was not conducted. It was also interesting to test the $ABCD$ method differentially in $|\eta|$ (see Figure 6.6(b)).

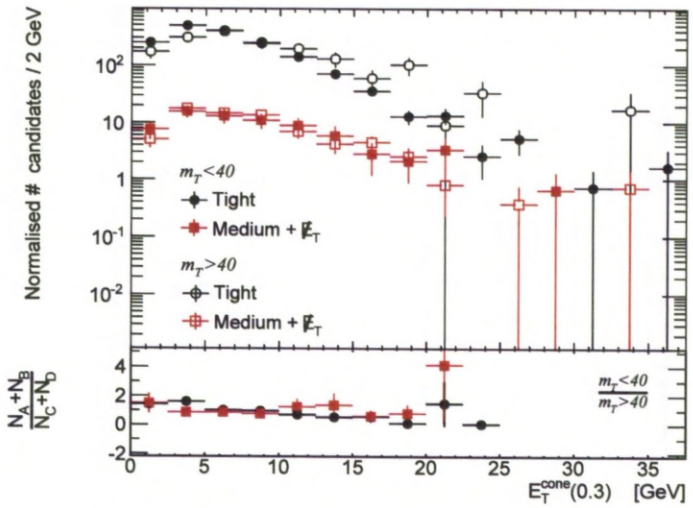

(a) E_{T}^{cone} distribution in slices of $m_{\mathrm{T}} < 40$ and $m_{\mathrm{T}} > 40$ GeV

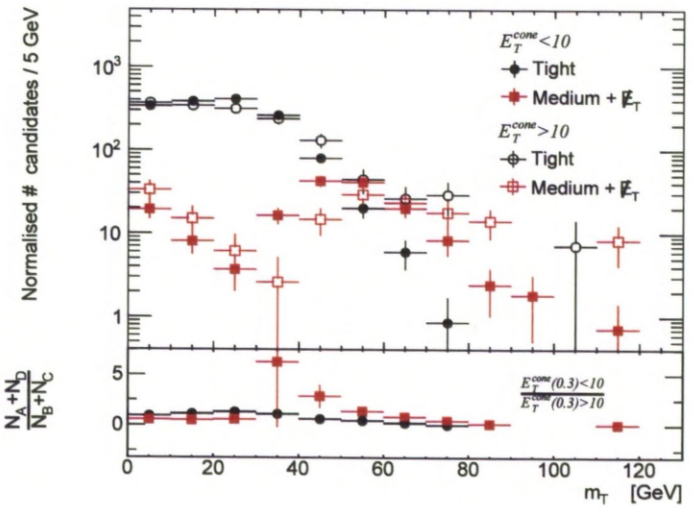

(b) m_{T} distribution in slices of $E_{\mathrm{T}}^{cone} < 10$ and $E_{\mathrm{T}}^{cone} > 10$ GeV

Figure 6.5: Electromagnetic isolation E_{T}^{cone} (a) and m_{T} (b) distributions seen in different regions of ABCD plane, as modeled by JF17 sample. In (a) close (open) markers denote E_{T}^{cone} distribution for $m_{\mathrm{T}} < 40$ ($m_{\mathrm{T}} > 40$) slice. Similarly, for (b) close (open) markers denote m_{T} distribution in $E_{\mathrm{T}}^{cone} < 10$ ($E_{\mathrm{T}}^{cone} > 10$) slice. Good agreement is observed between open and close markers within large uncertainties. Nevertheless certain degree of correlation between E_{T}^{cone} and m_{T} should be noted.

The test revealed that for the (0.0; 0.8) range, within available statistics, $ABCD$ estimate clearly differs in shape from the direct $JF17$ distribution but is consistent for the remaining $|\eta|$ range. It was never claimed, however that the $JF17$ provides the correct shape of the QCD background distribution, therefore the estimate for the $ABCD$ systematic is derived from the integrated number of events rather that evaluated differentially. The additional uncertainty for the $ABCD$ comes from $W \to e\nu_e$ and $EW + t\bar{t}$ removal applied to control regions used for the estimation of the QCD template (see Section 6.2.2) and is related to the uncertainty on the theoretical cross-sections for the electroweak Monte Carlo. In particular, regions A and C (with 33% and 13% signal and $EW + t\bar{t}$ relative contamination respectively) are affected. The systematic from variation within 5% limit provides only a small (3%) effect on the number of estimated QCD background events, which is therefore dominated by the systematics estimate from the closure test for the final uncertainty evaluation. Since the limitations of $JF17$ sample do not allow for detailed studies of the systematics variation in each bin of electron $|\eta|$ separately, as a conclusion a conservative estimate for the method overall systematic uncertainty is taken to be at the level of 30%. The choice was confirmed with the further stability test of the method.

The summary of the resultant QCD background template uncertainty in terms of a relative fraction of observed W candidate events, for a given $|\eta|$ range, is presented in Table 6.7.

6.2.4 Method validation

The comparison between the integrated number of events from the $ABCD$ data driven template and that provided directly by $JF17$, 4239 ± 226 and 2325 ± 568 respectively, reveals that they do not agree within statistical uncertainties. This is not unexpected. The limitations of the QCD Monte Carlo sample, visible in

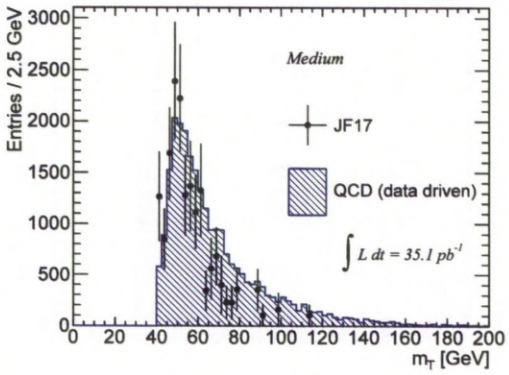

(a) m_{T} *QCD* data driven template vs. $JF17$

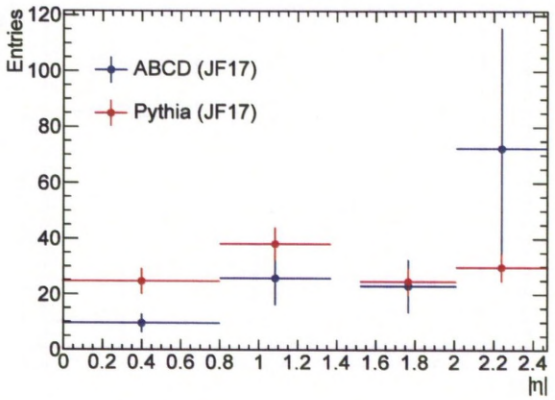

(b) *ABCD* with $JF17$ vs. pure $JF17$ in $|\eta|$

Figure 6.6: Plots are made using final W selection except for Tight electron identification requirement.(a) QCD data driven estimate compared to pure $JF1$ Monte Carlo, shown for electron transverse mass. (b) ABCD closure test with $JF17$ compared to direct values provided by $JF17$ distribution, shown in absolute pseudorapidity of an electron candidate, $|\eta|$.

fine binned distributions, simply do not allow for details to be reflected with the required accuracy, resulting in many unpopulated bins for the final W selection. Therefore, the conclusion regarding the agreement, is derived mainly from the direct comparison of shapes for populated bins and not from the global number of events. As shown on Figure 6.7 there is a consistency within statistical uncertainty between respective bins of m_{T} distributions, with well modeled maximum in a region of $\sim 50\,\mathrm{GeV}$ sharply falling towards the lower values of m_{T} due to transverse mass cut.

A similar conclusion is derived by comparing the sample with relaxed electron identification requirement (see Figure 6.6(a)) resulting in an almost sixfold background increase compared to full W boson selection. Albeit here, there is in general a slight overestimate in a tail of the distribution observed for $ABCD$ template compared to $JF17$ prediction, with reversed tendency around the maximum, nevertheless most within statistical uncertainty. The integrated number of events provided by $ABCD$ was 25259 ± 1393 and 17020 ± 1496 by $JF17$ model (actual number of Monte Carlo events before scaling to $\int L = 35.1\,pb^{-1}$ was 117.35 ± 10.32). There is still no consistency within statistics but the relative difference ($\sim 32\%$) is reduced compared to full W boson selection ($\sim 45\%$).
A more stringent test of the method comes from the direct comparison between the data and the sum of Monte Carlo samples ($W \rightarrow e\nu_e + EW + t\bar{t}$) with the QCD background template. From the requirements of the final measurement, the shape assessment of the hadronic jets distribution has to be conducted for each pseudorapidity bin η separately with differentiation into respective W charges. This was conducted for the final W selection of W^+ (see Figure 6.8) and W^- (see Figure 6.9) and also changing *Tight* to *Medium*. Relaxing electron ID results in large background contamination of up to 36% for the highest $|\eta|$ intervals (see Figure A.1(W^+) and Figure A.2 (W^-)). In both cases there was a reasonable agreement observed within statistics, with slight deviation for W^+

$-2.47 < \eta < -2.01$ (see Figure A.1(a)) due to an apparent overestimate in the tail of the QCD template.
Noticeable background increase towards the edges of the η range, in general, originates from the decline in electron identification performance (signal efficiency vs. background rejection). This is partially due to material effects in conjunction with reduced tracking performance for $|\eta| > 2.0$, as a consequence of the limited coverage of TRT.

Concluding, the $ABCD$ method is applicable for the purpose of QCD background modeling in further analysis. The resultant QCD template provides a plausible model for the hadronic jet events, as confirmed differentially for electron candidate pseudorapidity, η. The statistical uncertainties are within 5% overall with variations of up to 25% at the edges of the fiducial volume. The method overall systematic uncertainty is estimated to by in the range of 30% and is mostly related to residual correlation between the discriminant variables. The estimate is important for the precision of the final measurement but eventually it is not a major source of the systematic uncertainty.

6.2.5 Stability of the $ABCD$ method

To test the method stability under the condition of significant hadronic jets contamination, the full analysis chain was applied to a sample of electron candidates with *Medium* identification, where ID efficiency scale data/MC was applied accordingly Table 5.3.

The possibility of assessing systematic effects for the final cross section measurement from the cross-check analysis conducted on the enriched background sample (see Table 6.8) compared to full selection (see Table 6.7) was confirmed by general agreement between the data driven template and $JF17$ model (see Figure 6.6(a)). Within statistical limitations visible in m_{T} distribution the data

η	$W^{\pm}_{(stat)\pm(syst)}(\%)$	$W^{+}_{(stat)\pm(syst)}(\%)$	$W^{-}_{(stat)\pm(syst)}(\%)$
(0 - 0.8)	2.2 ± 0.1 ± 0.7	1.8 ± 0.2 ± 0.5	2.9 ± 0.2 ± 0.9
(0.8 - 1.37)	3.1 ± 0.2 ± 0.9	2.6 ± 0.3 ± 0.8	3.7 ± 0.4 ± 1.1
(1.37 - 1.52)			
(1.52 - 2.01)	3.7 ± 0.4 ± 1.1	2.7 ± 0.4 ± 0.8	5.3 ± 0.7 ± 1.6
(2.01 - 2.47)	8.6 ± 1.1 ± 2.6	7.7 ± 1.5 ± 2.3	10.6± 1.1 ± 3.2
(0 - 2.47)	3.7 ± 0.2 ± 1.1	3.1 ± 0.3 ± 0.9	4.6 ± 0.3 ± 1.4

Table 6.7: The charge dependent estimate of the number of QCD events in the signal region (D), N_D^{QCD} for each lepton pseudorapidity bin, $|\eta|$, as a relative fraction of observed W boson candidate events, shown for full $W \to e\nu_e$ selection The uncertainties are statistical and systematic (30%) in that order.

driven template is comparable to direct $JF17$ output. This was further confirmed by the good agreement for the expected shape of the QCD template, also when compared to globally measured transverse mass distribution Figure 6.10, and when examined differentially in bins of η for W^+ (see Figure 6.8) and W^- (see Figure 6.9). That was an explicit confirmation of the $ABCD$ template method stability.

However, since the QCD background is relatively large and unknown, it is required to reduce it as far as possible, and limit possible systematic biases for the precise cross sections measurement. The ratio between the W differential cross section measurements evaluated with full and relaxed criterion provides further tests of the systematics for the final measurement in each electron $|\eta|$ bin, differentiated also in W charges (see Figure 6.10). In particular, we observe large $\sim$ 6% systematic effect on the fiducial measurement at the edge of acceptance. Modeled QCD fraction for *Medium* electron selection is at the level of 30% for the largest eta bin and therefore the combined statistical and systematic effect on the differential cross section is $30\% \times 33\% = 10\%$ thus fully accounting for the measured *Medium* electron candidates cross section deviation.

In Table 6.7 the QCD estimate is presented in terms of relative number of W candidate events. In this way the overall impact on the accuracy of to the final measurement is assessed.

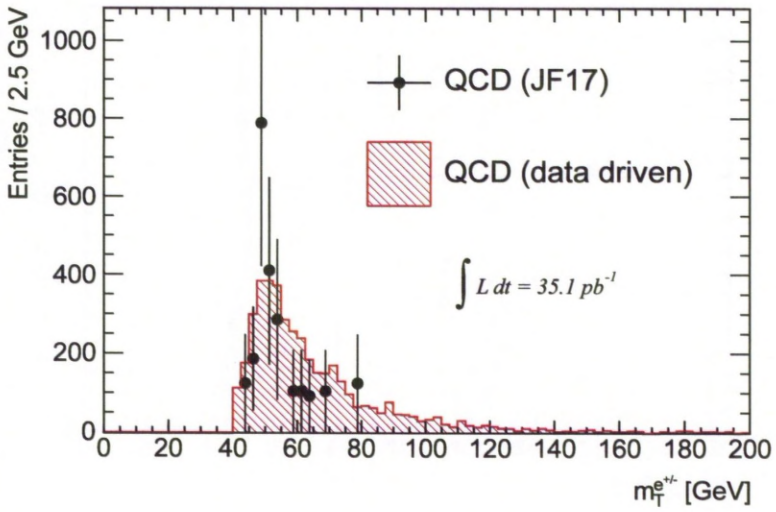

Figure 6.7: QCD data driven background distribution for full $W \to e\nu_e$ selection compared with the Monte-Carlo $QCD(JF17)$, normalized to the data luminosity.

η	$W^{\pm}_{(stat)\pm(syst)}(\%)$	$W^{+}_{(stat)\pm(syst)}(\%)$	$W^{-}_{(stat)\pm(syst)}(\%)$
(0 - 0.8)	7.8 ± 0.5 ± 2.3	6.3 ± 0.6 ± 1.9	9.8 ± 0.8 ± 2.9
(0.8 - 1.37)	14.5 ± 1.0 ± 4.4	12.4 ± 1.3 ± 3.7	17.5 ± 1.7 ± 5.3
(1.37 - 1.52)			
(1.52 - 2.01)	17.4 ± 1.7 ± 5.2	14.0 ± 1.9 ± 4.2	22.6 ± 3.1 ± 6.8
(2.01 - 2.47)	29.8 ± 3.8 ± 9.0	26.4 ± 5.1 ± 7.9	36.1 ± 4.2 ± 10.8
(0 - 2.47)	15.8 ± 0.9 ± 4.7	13.5 ± 1.2 ± 4.0	19.3 ± 1.4 ± 5.8

Table 6.8: The charge dependent estimate of the number of QCD events in the signal region (D), N_D^{QCD} for each lepton pseudorapidity bin, $|\eta|$, as a relative fraction of observed W boson candidate events, shown for the sample with large background increase, resulting from relaxed electron ID, used in cross-check analysis. The uncertainties are statistical and systematic (30%) in that order.

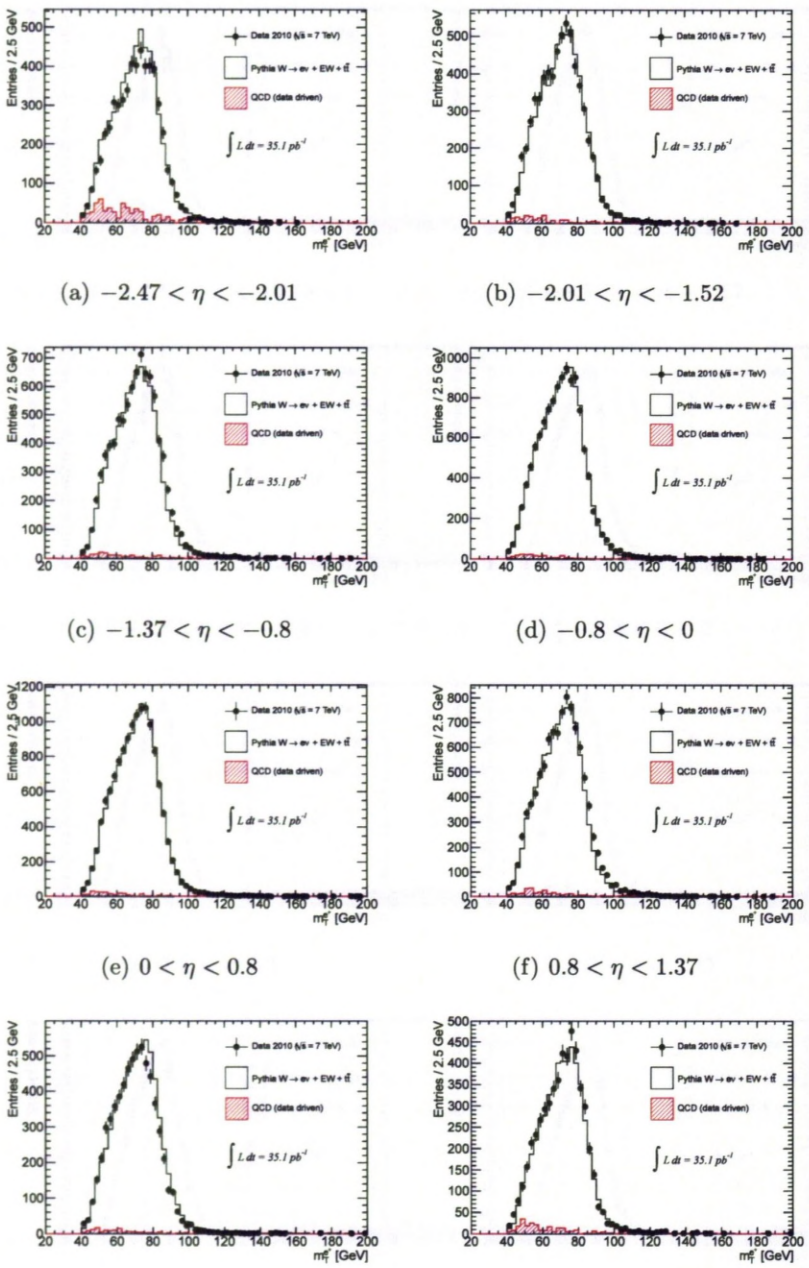

(a) $-2.47 < \eta < -2.01$

(b) $-2.01 < \eta < -1.52$

(c) $-1.37 < \eta < -0.8$

(d) $-0.8 < \eta < 0$

(e) $0 < \eta < 0.8$

(f) $0.8 < \eta < 1.37$

(g) $1.52 < \eta < 2.01$

(h) $2.01 < \eta < 2.47$

Figure 6.8: QCD background for $W^+ \to e^+\nu_e$ in different electron η ranges, shown for m_T distribition. Performance of QCD data driven template, confirmed with MC template for the $W \to e\nu_e + EW + t\bar{t}$ and 2010 DATA.

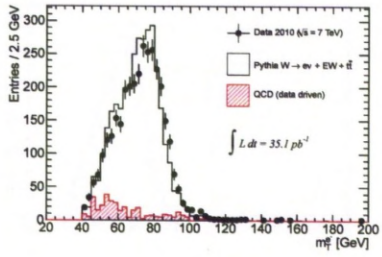

(a) $-2.47 < \eta < -2.01$

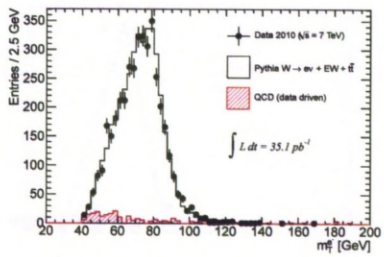

(b) $-2.01 < \eta < -1.52$

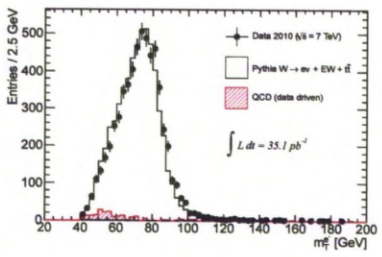

(c) $-1.37 < \eta < -0.8$

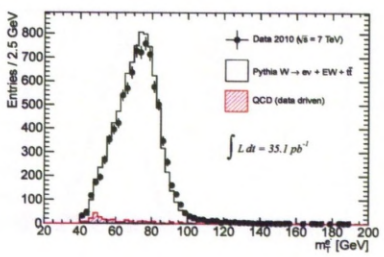

(d) $-0.8 < \eta < 0$

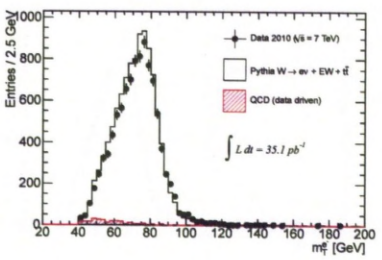

(e) $0 < \eta < 0.8$

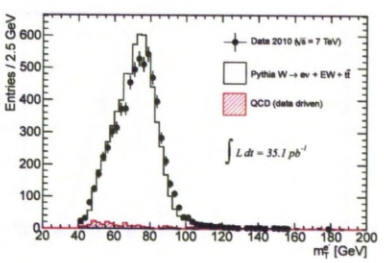

(f) $0.8 < \eta < 1.37$

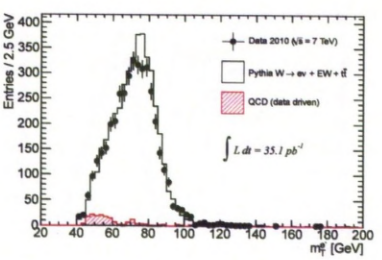

(g) $1.52 < \eta < 2.01$

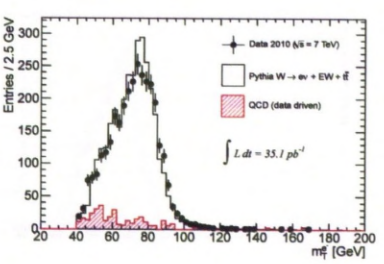

(h) $2.01 < \eta < 2.47$

Figure 6.9: QCD background for $W^- \to e^-\bar{\nu}_e$ in different electron η ranges, shown for m_T distribition. Performance of QCD data driven template, confirmed with MC template for the $W \to e\nu_e + EW + t\bar{t}$ and 2010 DATA.

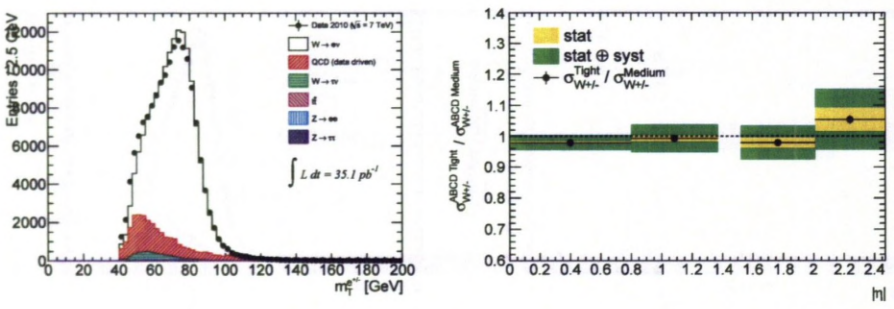

(a) $W^{\pm}$

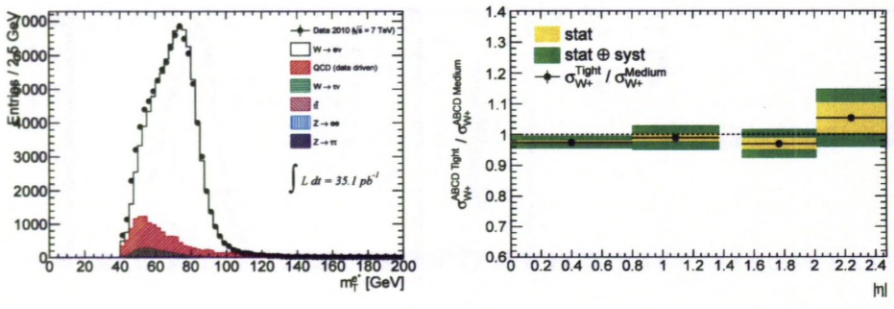

(b) W^{+}

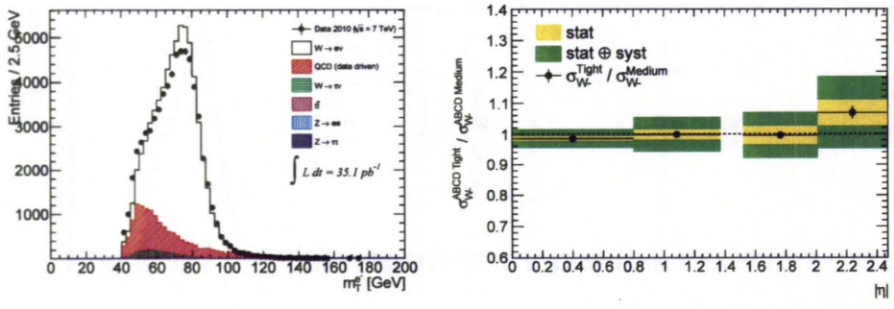

(c) W^{-}

Figure 6.10: Cross-check analysis results. ABCD method stability assessment with the sample of electrons, resulting from full W selection and relaxed (Medium) electron identification requirement. Ratios of a final fiducial cross-section values in $|\eta|$, performed with QCD template from standard W boson selection and derived with sample of electron with relaxed identification requirements.

6.3 Background Summary

The background to the $W \rightarrow e\nu_e$ channel accounts for 6.9% of the observed number W boson candidate events. It is 6.1% of W^+ and 8.0% of W^- candidates when differentiated in charge. In terms of W, W^+ and W^- candidates this is due to 3.7%, 3.1% and 4.6% contribution from hadronic jet events and 3.2%, 3.0% and 3.4% from electroweak and $t\bar{t}$ components. The main source of the systematics to the final measurement comes from the $ABCD$ data driven template, this has 1.1%, 0.9% and 1.4% impact on the final precision and when combined with electroweak + $t\bar{t}$ components accounts for 1.3%, 1.1% and 1.6% systematic uncertainty to the value of W, $W^+$and W^- integrated cross section respectively. Considered differentially, there are variations among $|\eta|$ regions of up to 8% in W^+ and 11% in W^- case of relative background contamination for the edges of the acceptance, this translates to 2.4% and 3.4% uncertainty for the precision of the differential W^+ and W^- measurements respectively.

Chapter 7

Cross Section Measurement

The chapter presents the summary of results for the inclusive W boson cross section measurement, together with the comparison to the recently published ATLAS $W \to e\nu_e$ result [21] and several theory predictions, also in terms of measured W^+/W^- cross sections ratio. The opening section illustrates the overall level of understanding of the W boson measurement by comparison between measured and simulated distributions. This is followed by the methodology of the documented measurement, details of the measurement systematics and discussion of the results.

7.1 Data - Monte Carlo Comparisons

The following section presents distributions for the selected W candidate events in data. These are compared to the full simulated sample of signal and background events generated with PYTHIA and the QCD template derived from the data (see Section 6.2). The plots show p_{T}, η, ϕ and E of selected electrons, together with $\not\!\!E_{\mathrm{T}}$ and resulting m_{T} and W p_{T}, for combined charge and also with additional selection on W charges. All Monte-Carlo samples have been normalised to the data integrated luminosity of $\int L = 35.1\,pb^{-1}$. The expected amount of background contamination is indicated as the shaded area in histograms. Typically the background accumulates at lower electron p_{T}, $\not\!\!E_{\mathrm{T}}$ or m_{T} values.

Detailed investigation of Figure 7.1 unveils the poor agreement of data and Monte Carlo in the region of m_T between 90-110 GeV. The effect is attributed to the QCD background estimate, since the region covers the m_{T} distribution edge with sharply falling statistics, and is difficult to model. This is however not a real concern since integration over the m_{T} distribution is conducted for the final measurement. Moreover it should be indicated that Figure 7.1 does not account for systematic effects which are not shown.

As a function of electron η the amount of background is relatively constant, with a small increase towards the edges of the acceptance being visible. This is caused by the dominant fake electrons from QCD jet production in detector regions with worse electron identification capabilities.

The visible asymmetry in data, and also as modeled by Monte Carlo distributions, observed for the region of ± 0.5 in electron η (see Figure 7.3) is understood from the investigation of LAr calorimeter problematic regions, summarized on $\eta - \phi$ maps (see Figure 5.1 in Section 5.2.2). There is a large [-1.5-0.0] region in calorimeter presampler η with clearly visible major problems detected, marked in red. In addition, there are further regions with identified "dead" OTXs in $\eta[-1, 0]$ of the second sampling layer, which contribute to the overall loss in efficiency. This also explains a fall in ϕ distribution at around -1.5 (see Figure 7.5).

As a conclusion, the observed agreement of the Monte Carlo with the data is generally very good and supports the cross section extraction following the method as described in the subsequent section.

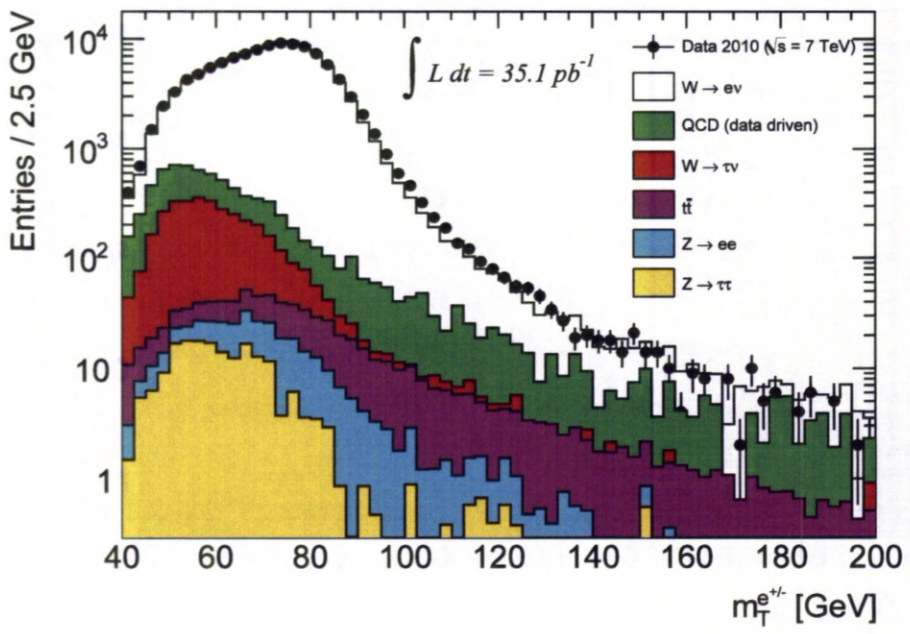

Figure 7.1: Distribution of transverse mass m_T of the electron-$\not{E}_T$ system in the selected $W \rightarrow e\nu$ candidate events after final W boson selection. Shown are clearly visible components of the background with the main contribution - QCD, derived from the data driven method. The simulated distributions are normalised to the data luminosity.

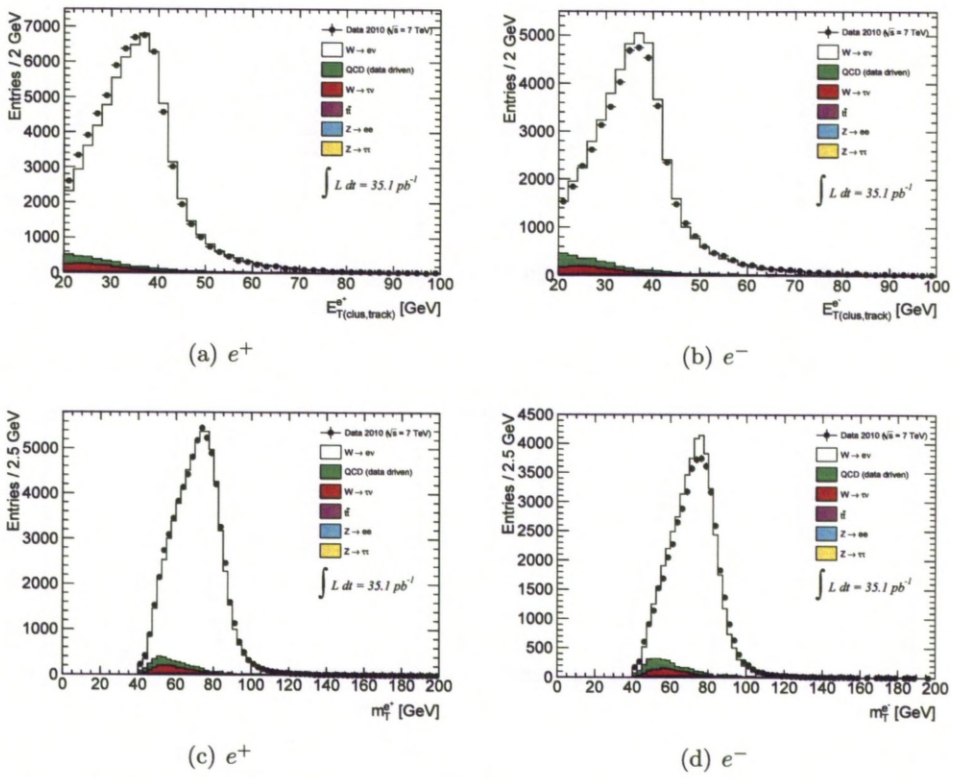

(a) e^+ (b) e^-

(c) e^+ (d) e^-

Figure 7.2: Distribution of transverse energy E_T of the electron in the selected $W \to e\nu$ candidate events after all cuts for positive (left) and negative (right) charge. Bottom: Transverse mass distributions for e^+ (left) and e^- (right). The simulated distributions are normalised to the data luminosity

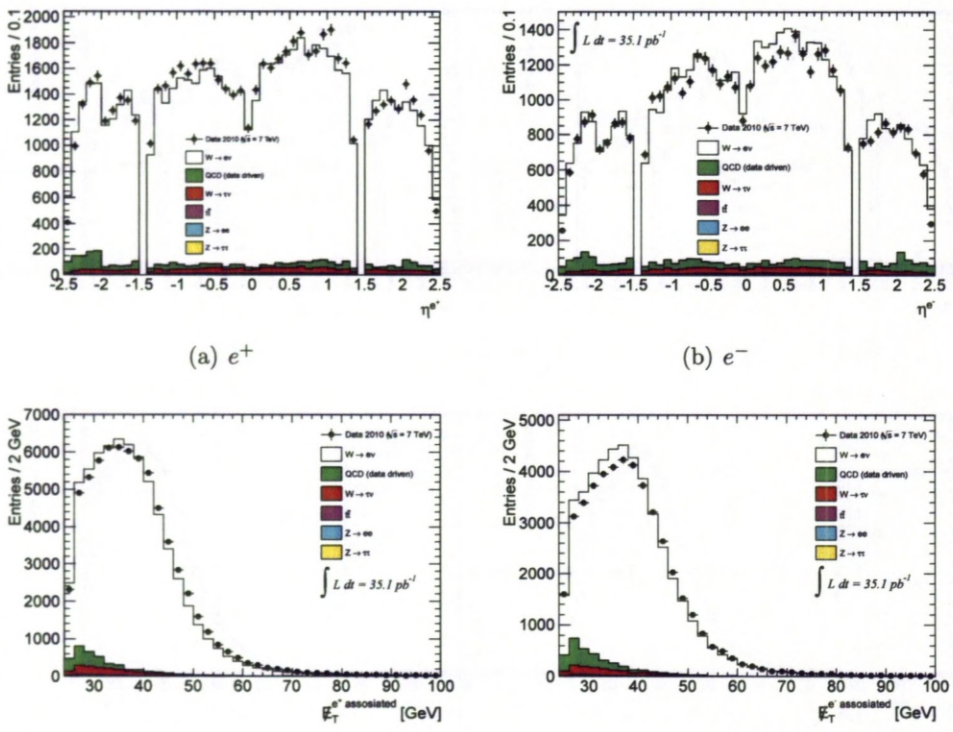

(a) e^+ (b) e^-

(c) e^+ (d) e^-

Figure 7.3: Top: Distribution η of the electron in the selected $W \to e\nu$ candidate events after final W boson selection for positive (left) and negative (right) charge. Bottom: Distributions of E_T^{miss} for e^+ (left) and e^- (right), where the label "associated" indicates the charge of the electron in the $W \to e\nu_e$ event. The simulated distributions are normalised to the data luminosity

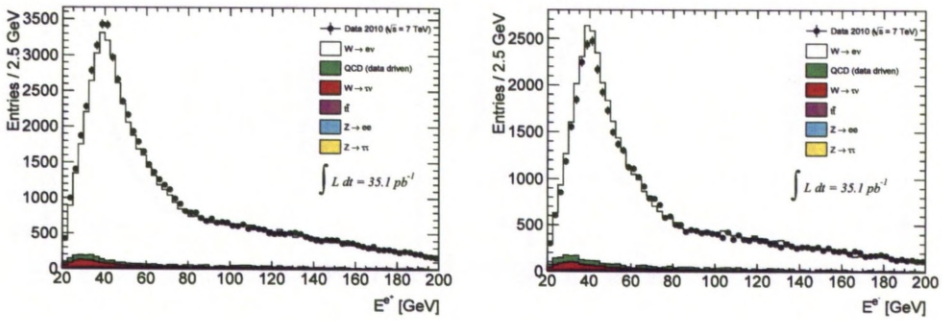

Figure 7.4: Distribution of the energy of the electron selected $W \rightarrow e\nu$ candidate events for complete selection. Shown for positive (left) and negative (right) charge. The simulated distributions are normalised to the data luminosity

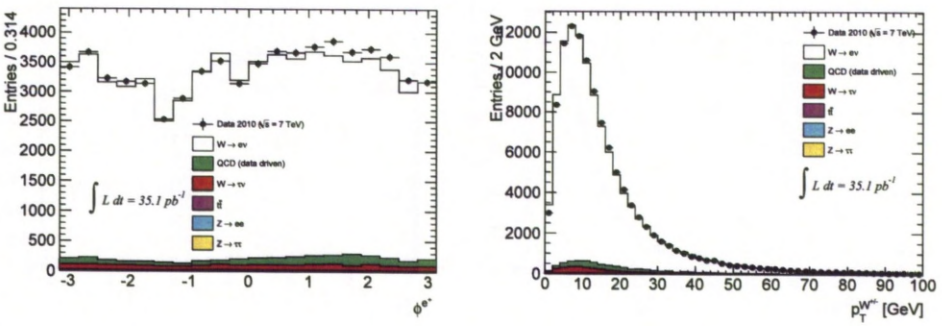

Figure 7.5: Distribution of the the ϕ of the electron and the transverse momentum of the W selected $W \rightarrow e\nu$ candidate events for complete selection and sum of charges. The simulated distributions are normalised to the data luminosity

7.2 Cross Section Analysis Procedure

In the following section two definitions for the W boson cross section measurement are consider, σ_W^{fid} and σ_W^{tot}, corresponding to the restricted geometrical and kinematical volume of the measurement and to the full domain, respectively. The total integrated W cross section, σ_W^{tot}, is evaluated using the following formula:

$$\sigma_W^{tot} = \sigma_W \times BR(W \to e\nu_e) = \frac{\sigma_W^{fid}}{A_W}, \tag{7.1}$$

where directly measured , σ_W^{fid}, cross section is defined as:

$$\sigma_W^{fid} = \frac{N^{DATA} - B}{C_W \cdot L_{int}}, \tag{7.2}$$

The number of candidate events measured in data, N^{DATA} (see Chapter 5), has to be adjusted by the number of expected background events, B, determined using data and simulation estimates (see Chapter 6). The result is further scaled by the value of the integrated luminosity, L_{int}, corresponding to the run selections and trigger employed. In order to evaluate the cross section for the analysis fiducial volume, σ_W^{fid}, scaling by the efficiency factor, C_W, is performed. C_W denotes the ratio (see Equation 7.3) between the total number of simulated events, which pass the final W selection, $N_{MC,rec}$, and the total number of generated events satisfying the fiducial volume cuts, $N_{MC,gen,cut}$. This correction factor includes the efficiency for reconstructing, identifying and triggering on W boson decays, falling within the geometrical acceptance. Therefore the correction by the efficiency factor C_W determines the integrated cross section, σ_W^{fid}, within the fiducial region of the measurement. For the purpose of the following analysis, the correction factor C_W is fully taken from the $W \to e\nu_e$ Monte Carlo signal sample and is evaluated using electrons extrapolated to the point before QCD Final State

Radiation (FSR) provided by PHOTOS algorithm. Therefore the measurements are fully corrected for $QED\ FSR$ and can be consistently compared to $NNLO$ QCD calculations.

$$C_W = \frac{N_{MC,rec}}{N_{MC,gen,cut}} \quad \text{and} \quad A_W = \frac{N_{MC,gen,cut}}{N_{MC,gen,all}}, \tag{7.3}$$

The total inclusive cross section times the electron branching ratio, σ_W^{tot} defined by Equation 7.1, is derived via the geometrical acceptance factor, A_W, introduced to extrapolate the measurement of σ_W^{fid} to the full kinematic domain. The geometrical acceptance factor A_W is defined as (see Equation 7.3) a fraction of the total number of generated events at truth level, $N_{MC,gen,all}$ which pass the fiducial volume cuts, $N_{MC,gen,cut}$. Also the quantity A_W is determined at so called Born level, i.e. before QED final-state radiation. Since A_W can only be evaluated via Monte Carlo simulation, it has an associated theoretical uncertainty which is discussed further in Section 7.2.1.

The associated statistical uncertainties δC_W and δA_W on efficiencies C_W and A_W are standard binomial uncertainties (see Appendix C):

$$(\delta C_W)^2 = \frac{C_W(1-C_W)}{N_{MC,gen,cut}} \quad \text{and} \quad (\delta A_W)^2 = \frac{A_W(1-A_W)}{N_{MC,gen,all}}, \tag{7.4}$$

It is worth mentioning, that the proposed binomial estimate for the efficiency error is reasonable for the values far from the limits, i.e $A_W, C_W \neq 0,\ 1$. This is true in a considered case.

As briefly mentioned, the extrapolation to the total cross section is dominated by the theoretical uncertainties on A_W estimated from the Monte Carlo, since the statistics is not a limiting factor. This is a major effect for the σ_W^{tot} measurement and has only negligible impact within the experimentally accessible phase-space region.

Therefore it is beneficial to decouple the cross section measurement in the fiducial region and the extrapolation to the total cross-section. The cross section measured within the fiducial region can be easily adapted at a later time to update the total cross section measurement, given further improvements on the prediction of A_W.

Depending on the desired granularity for the final cross section measurement, several C_W and A_W correction factors may be required. In the case of the integrated cross section measurement presented in the following section the global correction factor C_W was defined for the fiducial measurement. This corresponds to a single bin in the phase space, which is determined by the geometrical and kinematical acceptance cuts at the Monte Carlo generator level. The subsequent extrapolation, A_W, is a simple scaling from the fiducial volume to the full kinematic domain. This simplified approach, may be subject to significant biases in the case when the predicted kinematical distributions for W boson differ from reality. However this was already confirmed as not being the case, in the presented analysis, via comparisons between measured and predicted distribution of $W \rightarrow e\nu_e$ events (see Section 7.1). Moreover for the η differential cross section measurement, $\sigma(\eta)$, (see Section 7.5), different bin to bin correction factors were determined to reflect the granularity of the decay lepton phase space, i.e four bins in $|\eta|$ and one in p_{T}.

7.2.1 A_W Uncertainty

The extrapolation of the fiducial measurement to the total cross-section is entirely based on the estimate provided by the Monte Carlo simulation. The central values of the geometrical acceptance factors, $A_{W^{\pm}}$, have been calculated using the PYTHIA samples (see Chapter 4) generated with the modified LO parton distribution function (PDF) MRST LO^* [31,95]. The statistical uncertainties on these values are negligible. The systematic uncertainties on the geometrical acceptances

Monte Carlo	A_W	A_{W^+}	A_{W^-}
PYTHIA MRST (*LO**)	0.462	0.466	0.457
PYTHIA CTEQ6.6 (*NLO*) [96]	0.471	0.479	0.458
PYTHIA HERAPDF1.0 (*NLO*) [96]	0.470	0.477	0.461
MC@NLO CTEQ6.6 (*NLO*)	0.466	0.478	0.452
MC@NLO HERAPDF1.0 (*NLO*)	0.465	0.475	0.453

Table 7.1: Summary of acceptance values A_W for $W \to e\nu_e$ channel, also separated in charges, using various Monte Carlo simulations resulting from a combination of PDF set and generator.

are dominated by the limited knowledge of the proton *PDF*s and the modeling of W boson production at the LHC. They have been estimated as half of the maximum deviation between the acceptances obtained with different combinations of generators and *PDF* sets. The default MRSTO *LO** used with PYTHIA generator was subsequently replaced by CTEQ6.6 [26] and HERAPDF1.0 [24] *NLO PDF* sets. The procedure was repeated for MC@NLO generator since it employs a different parton shower model. Table 7.1 summarizes the geometrical acceptance central values used in the presented analysis and the remaining variations derived using the above method. The resultant systematic uncertainties of 1.0% ($W^{\pm}$), 1.4% (W^+) and 1.0% (W^-) were propagated to the respective total cross section measurements. The same methodology was adapted (see Table 7.2) for the total differential cross section measurement reported in Section 7.5.

7.2.2 The ATLAS $W \to e\nu_e$ cross section measurement

It is important to briefly address the major differences between recently published ATLAS result for $W \to e\nu_e$ cross section [21] and the one presented in this thesis. The major difference comes from the Athena release 16 which was used to re-process the data and MC samples for the ATLAS 2010 measurement. This was followed by modifications to the $W \to e\nu_e$ event selection (*Tight* selection

$A_W(\|\eta\|)$									
$\|\eta\|$	PYTHIA MRST			MC@NLO CTEQ6.6			MC@NLO HERAPDF1.0		
	$W^{\pm}$	W^{+}	W^{-}	$W^{\pm}$	W^{+}	W^{-}	$W^{\pm}$	W^{+}	W^{-}
(0.00 - 0.80)	0.648	0.604	0.714	0.662	0.610	0.729	0.659	0.608	0.721
(0.80 - 1.37)	0.657	0.621	0.714	0.667	0.626	0.721	0.666	0.627	0.715
(1.52 - 2.01)	0.671	0.652	0.706	0.685	0.671	0.704	0.684	0.670	0.702
(2.01 - 2.47)	0.696	0.700	0.690	0.705	0.721	0.684	0.707	0.723	0.688

Table 7.2: Summary of $|\eta|$ differential acceptance values $A_W(|\eta|)$ for $W \to e\nu_e$ channel, also separated in charges, using various Monte Carlo simulations resulting from a combination of PDF set and generator.

is replaced by *Medium*, b-layer and calorimeter isolation requirements), more accurate *QCD* background template and refined treatment of systematic effects (e.g. smaller $\not{E}_{\mathrm{T}}$ uncertainty due to updated $\not{E}_{\mathrm{T}}$ reconstruction algorithm which makes use of the full event reconstruction, with a calibration based on reconstructed physics objects (refined calibration)). Therefore the ATLAS measurement is dominated by smaller systematic uncertainties i.e. electron identification scale factors are derived within fine granularity of 10 bins in cluster central η and 11 bins in cluster E_{T}, starting from 5 GeV. Finally the Monte Carlo generator used to model the signal process had been altered from PYTHIA to MC@NLO.

7.3 Systematic Uncertainties

In this section the systematic uncertainties for the final W cross section measurement are presented. Since the treatment of systematic effects related to the modeling of the background to $W \to e\nu_e$ channel was discussed in the Chapter 6 the discussion will not be repeated here but only relevant results quoted.

	$\delta\sigma_{W^\pm}$	$\delta\sigma_{W^+}$	$\delta\sigma_{W^-}$
Trigger efficiency	0.4	0.4	0.4
Electron reconstruction	1.5	1.5	1.5
Electron identification (SF)	2.5	2.5	2.5
Electron energy scale	1.2	1.3	1.1
$\not{E}_T$ scale and resolution	2.0	2.0	2.0
OTX	0.4	0.4	0.4
Charge misidentification	0.0	0.1	0.1
QCD background template	1.1	0.9	1.4
EW + $t\bar{t}$ background	0.2	0.2	0.2
Total experimental uncertainty	3.9	3.9	4.0
A_W theoretical uncertainty (PDFs)	1.0	1.4	1.0
Total excluding luminosity	4.1	4.1	4.1
Luminosity		3.4	

Table 7.3: Summary of systematic uncertainties on the integrated $W \to e\nu_e$ cross-section measurement defined in the fiducial acceptance of the ATLAS *detector, $\sigma^{fid}_{W^\pm}$, also differentiated between respective W boson charges. Also shown the theoretical uncertainty on A_W from the extrapolation to the total cross section calculation. The relative errors on the cross sections are given in percent.*

7.3.1 Trigger modeling

As detailed in section Section 5.3.1, the trigger SF applied to the simulated data is $99.5 \pm 0.4\%$. For the $W \to e\nu_e$ channel this directly translates to 0.4% uncertainty on the final cross section measurement.

7.3.2 Electron reconstruction and identification efficiency (SF)

The overall reconstruction efficiency scale factor (see Section 5.3.2) that accounts for differences between reconstruction efficiency in data and Monte Carlo was determined to be 1.000 ± 0.015 (stat+syst) [85]. This translates directly to the 1.5% uncertainty on the final fiducial cross section measurement.

The electron identification scale factors together with related uncertainties are summarized in Table 5.3. Values were estimated as function of electron pseudorapidity η in the p_{T} range $20 < E_{\mathrm{T}} < 50\,\mathrm{GeV}$, without differentiating into separate W boson charges. The resultant systematic uncertainty for $\sigma^{fid}_{W\pm}$ is an averaged value across entire $\{\eta, p_{\mathrm{T}}\}$ range weighted by the number of events. For the differential measurements in the $|\eta|$ this simplifies to the average value per bin, since the η distribution for electrons originating from $W^{\pm}$ boson is symmetrical, thus both ranges contribute to the half of the $|\eta|$ statistics.

7.3.3 Electron energy scale

In this thesis the official recommendations for the energy scale were applied to data [86]. The uncertainty on the energy scale (see Section 5.3.3) is accounted for in the cross section value by applying the correction (see Table 5.4) also to Monte Carlo (which is otherwise applied to the data alone) and varying the scale within its respective uncertainty. In principle, this could be evaluated exclusively on data, nevertheless larger amount of statistics present in the Monte Carlo samples makes it the choice for the test of the effect. The resultant relative systematic

uncertainty on the final cross section measurement is a difference between up and down variation divided by twice the nominal cross section value i.e. $\delta\sigma_W = \frac{\sigma_W^{up} - \sigma_W^{down}}{2\times\sigma_W}$. The result has been summarized for $W^{\pm}$ integrated measurement in Table 7.3 and also in terms of electron pseudorapidity $|\eta|$ for the differential cross section in Table 7.3(a) (W^+) and Table 7.3(b) (W^-).

7.3.4 $\not\!\!E_{\mathrm{T}}$ scale and resolution

The systematic uncertainty on the calorimetric part of the $\not\!\!E_{\mathrm{T}}$ has been studied in detail in [84], separating the contributions from the jet energy scale and resolution, soft jet and cell-out terms. In each case, up and down variations, as well as correlations have been estimated for $W \to e\nu_e$ events in charge and pseudorapidity bins.

7.3.5 LAr problematic regions (OTX)

Due to the exclusion of dying or noisy OTX plug-ins in the LAr calorimeter (see Section 5.2.2), there is an additional uncertainty attributed to electrons that fail to be properly reconstructed due this problem ("boarder effects"). It was found that the fiducial cut (OTX cut) in the LAr removes a sizable $\sim 5\%$ fraction of W events within the fiducial region of the measurement. The overall systematic uncertainty associated with the exclusion of these regions by using maps provided by LAr monitoring system (OTX maps, see Figure 5.1), was studied and found to be 0.4% - a very small effect for the $W \to e\nu_e$ channel [97].

7.3.6 Charge misidentification

The major systematic effect on the charge misidentification probability comes from the uncertainty on the background estimate in the $T\&P$ method. To asses the systematic uncertainty, variations in the background level due to different selections of tag requirements were performed [84]. Also the values for the discriminating variables used in the background estimation were varied. To propagate

this effect to the uncertainties for the final W boson cross section measurement, systematic variation of the charge misidentification, as a function of the electron η which covered the observed data/MC differences was performed, as detailed in [98]. The resulting variations on the inclusive the W^+ and W^- measurements were small, at the level of 0.1% depending on η region.

7.4 Integrated Cross Section Results

Table 7.7 reports the number of W candidates, estimated background events, and the correction factors A_W and C_W used as inputs for the measurement. Additionally Table 7.6 differentiates the background contributions from EW and QCD components. Equation 7.1 and Equation 7.2 results in total and fiducial cross sections values listed in Table 7.8. The integrated fiducial cross sections for W^+, W^- and $W^\pm$ channels with their respective uncertainties are all measured to about 4% systematic uncertainty, with significantly smaller uncertainties due to statistics and the luminosity uncertainty of 3.4%.

(a) W^+

$\|\eta\|$	(0.0;0.8)	(0.8;1.37)	(1.52;2.01)	(2.01,2.47)
Trigger efficiency	0.4	0.4	0.4	0.4
Electron reconstruction	1.5	1.5	1.5	1.5
Electron identification (SF)	1.8	2.3	3.5	3.4
Electron energy scale	1.0	1.0	1.7	1.8
$\not{E}_T$ scale and resolution	2.0	2.0	2.0	2.0
OTX	0.4	0.4	0.4	0.4
Charge misidentification	< 0.1	0.1	0.2	0.4
QCD background template	0.5	0.8	0.8	2.3
EW + $t\bar{t}$ background	0.2	0.1	0.2	0.1
Total experimental uncertainty	3.3	3.7	4.7	5.2
A_W theoretical uncertainty (PDFs)	0.4	0.5	1.5	1.6
Total uncertainty excluding luminosity	3.3	3.7	4.9	5.4

(b) W^-

$\|\eta\|$	(0.0;0.8)	(0.8;1.37)	(1.52;2.01)	(2.01,2.47)
Trigger efficiency	0.4	0.4	0.4	0.4
Electron reconstruction	1.5	1.5	1.5	1.5
Electron identification (SF)	1.8	2.3	3.5	3.4
Electron energy scale	0.9	0.8	1.5	1.5
$\not{E}_T$ scale and resolution	2.0	2.0	2.0	2.0
OTX	0.4	0.4	0.4	0.4
Charge misidentification	< 0.1	0.1	0.3	0.7
QCD background template	0.9	1.1	1.6	3.2
EW + $t\bar{t}$ background	0.2	0.2	0.2	0.2
Total experimental uncertainty	3.4	3.7	4.8	5.6
A_W theoretical uncertainty (PDFs)	1.0	0.5	0.3	0.4
Total uncertainty excluding luminosity	3.5	3.7	4.8	5.6

Table 7.4: Relative impact of the different systematic uncertainties on the precision of the $W \to e\nu_e$ differential cross section measurement given in percent, separated into W boson respective charges $\frac{d\sigma^{fid}_{W^+}}{d|\eta|}$ and $\frac{d\sigma^{fid}_{W^-}}{d|\eta|}$. The estimate of the uncertainty from the extrapolation to the full kinematic range, A_W, is also presented.

$\|\eta\|$	(0.0;0.8)	(0.8;1.37)	(1.52;2.01)	(2.01,2.47)
Trigger efficiency	0.4	0.4	0.4	0.4
Electron reconstruction	1.5	1.5	1.5	1.5
Electron identification (SF)	1.8	2.3	3.5	3.4
Electron energy scale and resolution	0.9	0.9	1.6	1.7
$\not{E}_{\mathrm{T}}$ scale and resolution	2.0	2.0	2.0	2.0
OTX	0.4	0.4	0.4	0.4
Charge misidentification	0.0	0.0	0.0	0.0
QCD background template	0.7	0.9	1.1	2.7
EW + $t\bar{t}$ background	0.2	0.1	0.2	0.1
Total experimental uncertainty	3.3	3.7	4.7	5.3
A_W theoretical uncertainty (PDFs)	0.6	0.5	1.0	1.1
Total uncertainty excluding luminosity	3.4	3.7	4.8	5.4

Table 7.5: Relative impact of the different systematic uncertainties on the precision of the differential W boson cross section measurement, $\frac{d\sigma^{fid}_{W^{+/-}}}{d|\eta|}$, given in percent, summarized for $W \to e\nu_e$ channel. The estimate of the uncertainty from the extrapolation to the full kinematic range, A_W, is also presented.

process	W	W^+	W^-
$N^{EW+t\bar{t}}$	$3621 \pm 35 \pm 73$	$2038 \pm 26 \pm 40$	$1583 \pm 23 \pm 32$
N^{QCD}	$4239 \pm 226 \pm 1272$	$2134 \pm 183 \pm 640$	$2126 \pm 147 \pm 638$
Total Background	$7860 \pm 229 \pm 1274$	$4172 \pm 185 \pm 641$	$3709 \pm 149 \pm 639$

Table 7.6: Summary of the estimated number of background events in $W \to e\nu_e$ channel for the integrated cross section measurements, with respective statistical and systematic uncertainties.

	W	W^+	W^-
N^{DATA}	114047	67941	46106
B	$7860 \pm 229 \pm 1274$	$4172 \pm 185 \pm 641$	$3709 \pm 149 \pm 639$
C_W	$0.6276 \pm 0.0007 \pm 0.0245$	$0.6251 \pm 0.0009 \pm 0.0244$	$0.6314 \pm 0.0011 \pm 0.0253$
A_W	$0.4621 \pm 0.0005 \pm 0.0046$	$0.4660 \pm 0.0007 \pm 0.0065$	$0.4567 \pm 0.0008 \pm 0.0046$
L_{int}		$35.1 \pm 1.2\,\mathrm{pb}^{-1}$	

Table 7.7: Inputs for the cross section calculation in the $W \to e\nu_e$ channels. The first error is due to statistical effects, while the second is systematic.

	$\sigma_W^{fid} \times \mathbf{BR}(W \to e\nu_e)$ [nb]
W^+	$2.907 \pm 0.015_{(stat.)} \pm 0.113_{(syst.)} \pm 0.099_{(lumi.)}$
W^-	$1.913 \pm 0.012_{(stat.)} \pm 0.077_{(syst.)} \pm 0.065_{(lumi.)}$
$W^\pm$	$4.820 \pm 0.019_{(stat.)} \pm 0.188_{(syst.)} \pm 0.164_{(lumi.)}$
	$\sigma_W^{tot} \times \mathbf{BR}(W \to e\nu_e)$ [nb]
W^+	$6.237 \pm 0.034_{(stat.)} \pm 0.243_{(syst.)} \pm 0.212_{(lumi.)} \pm 0.087_{(acc.)}$
W^-	$4.189 \pm 0.028_{(stat.)} \pm 0.168_{(syst.)} \pm 0.142_{(lumi.)} \pm 0.042_{(acc.)}$
$W^\pm$	$10.430 \pm 0.043_{(stat.)} \pm 0.407_{(syst.)} \pm 0.355_{(lumi.)} \pm 0.104_{(acc.)}$

Table 7.8: Fiducial and total cross sections times branching ratio for W^+, W^- and $W^\pm$ production in the electron decay channel. The electron fiducial regions are defined as: $p_{T,e} > 20\,\text{GeV}$, $pt, \nu > 25\,\text{GeV}$, and $m_T > 40\,\text{GeV}$ and $|\eta| < 2.47$ (exclude $1.37 < |\eta| < 1.52$) The uncertainties denote the statistical (stat.), the experimental systematic (syst.), the luminosity (lumi.) and the extrapolation (acc.) uncertainties.

It is natural to compare the measured integrated cross sections with the recently published ATLAS results [21] and theoretical prediction, evaluated in the fiducial and extrapolated to full kinematic volume. The comparison is shown in Figure 7.6, where W^+ cross section versus the corresponding W^- value are overlayed with the recently published ATLAS values and predictions based on the *NNLO PDFs* from MSTW08 [32], ABKM09 [99,100], HERAPDF1.5 [24,101] and JR09 [102]. The *NNLO* predictions used, had been calculated with recent version of FEWZ [20,61] and DYNNLO [103,104] programs and the uncertainties shown correspond to the *PDFs* errors only. The uncertainties are depicted by 68% CL ellipses (see Appendix D) defined by correlation coefficients for the statistical and systematic uncertainties, where inner, shorter ellipse, is obtained excluding luminosity uncertainty and the outer ellipse shows total uncertainty.

The following sources of uncertainty (see Section 7.3) were regarded as fully correlated between W^+ and W^- measurements: trigger efficiency, electron reconstruction and identification, uncertainty on the $\not{E}_T$ measurement and the use of

the maps for LAr problematic regions. The luminosity uncertainty of 3.4% is also fully correlated between measurements. In contrast the charge misidentification is regarded as anti-correlated, which is also assumed for the uncertainty from the $A_{W^\pm}$ estimates in case of the total measurements.

For the fiducial cross section results (see Figure 7.6(a)) the measured values are compatible with the most recent results from ATLAS [21]. There is also good agrement with the theory predictions, particularly, derived from MSTW08 and HERAPDF1.5 PDF sets. It is worth noting that the overall differences between the theory values are larger than with respect to the conducted measurement. The predictions rely on the evolution of the PDFs into the W mass scale, determined mainly by the deep inelastic scattering (DIS) data from HERA, therefore it is an evident confirmation of its validity up to the kinematic range probed in W boson production at the LHC.

The comparison was also conducted for the total integrated cross sections (see Figure 7.6(b)). As mentioned the precision of the results is a subject to the additional extrapolation uncertainty. For the published ATLAS measurement the central values of the geometrical acceptances were determined using the MC@NLO Monte Carlo generator and CTEQ6.6 PDF set, (see Table 7.1). This fully accounts for approximately 2.5% positive (for W^+) and 1.1% negative (for W^-) shift in respective values observed, compared to relative position of the fiducial measurement from ATLAS with respect to he one conducted by the author. Nevertheless both measurements are still compatible despite being less able to discriminate the details of PDFs.

Figure 7.7 shows the ratios of $W^\pm$ cross sections. These were evaluated accounting for possible correlations between the uncertainties. As a result a high precision of $\sim$ 2.5% and $\sim$ 2.8% is achieved, for fiducial (see Figure 7.7(a)) and total (see Figure 7.7(b)) measurements ratio respectively. The increase in accuracy compared to the pure cross section values is attributed to the cancelations

between fully correlated uncertainties discussed earlier. The measured ratios are compatible with the ATLAS measurement and remaining $NNLO$ predictions within the total uncertainty.

7.5 Differential Cross Section Results

The differential $W^{\pm}$ cross sections divided by the bin widths are shown in Figure 7.8 and Figure 7.9, for separated and combined charge measurements. The summary for the numbers of W candidates, estimated background events, and the correction factors, A_W and C_W, is reported differentially in electron pseudorapidity bins (see Table 7.9). The fiducial measurements are seen to be in a very good agreement with published ATLAS results. The overall precision of the fiducial cross section data, excluding luminosity normalisation uncertainty, reaches $\sim 4\%$ for the central pseudorapidity and falls to $\sim 7\%$ at the edge of acceptance. The numerical values for the fiducial measurement are given in Table 7.10.

Measured $|\eta|$ dependencies are broadly described by the predictions of the PDF sets examined. Considering systematic uncertainties only, observed deviations, in particular for JR09 PDF set, within central pseudorapidity range, indicate that improved experimental precision of coming experiments may provide a genuine constraints for the parton distributions in the proton. The precision of the total differential cross section measurement is further limited by the theoretical constrains on the estimate of the extrapolation factor A_W. General agreement is observed between the measurement and available CTEQ and HERA PDFs, nevertheless additional information may be extracted due to large uncertainties of the measurement.

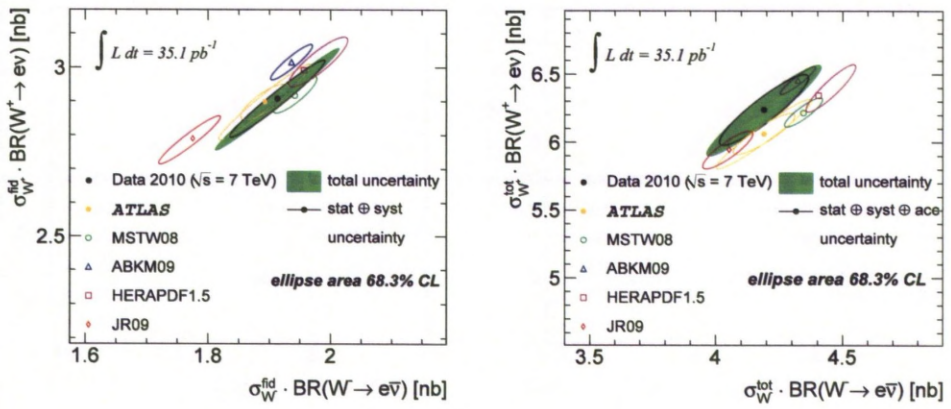

(a) (b)

Figure 7.6: Measured and predicted total cross sections times leptonic branching ratios σ_{W^+} vs. σ_{W^-}, shown for fiducial volume (left) and extrapolated to full kinematic range (right). The ellipses (see Appendix D) illustrate the 68% CL coverage for total uncertainties (full green) and excluding the luminosity (open black). Also shown recently published [21] ATLAS results. The uncertainties of the theoretical predictions correspond to the PDF uncertainties only.

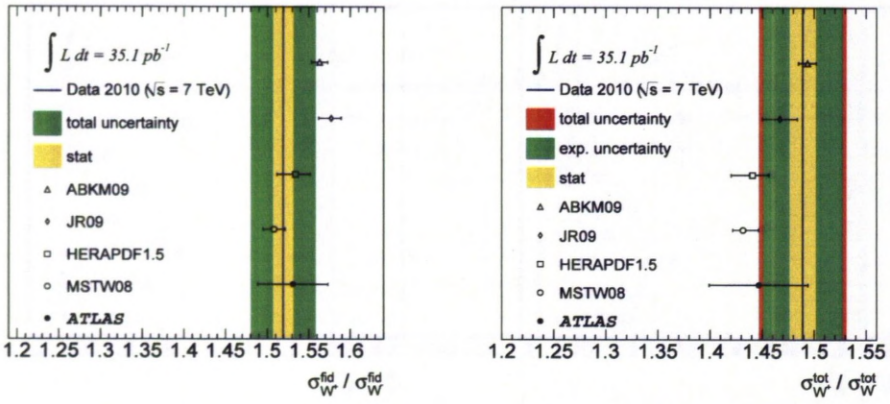

(a) (b)

Figure 7.7: Measured and predicted fiducial (left) and total (right) cross section ratios, $\sigma_{W^+}/\sigma_{W^-}$. For the fiducial measurement shown uncertainties are statistical (inner yellow band) and total (stat $\oplus$ syst) uncertainty (outer green band). In addition, extrapolation to the full kinematic range includes contribution from acceptance correction (outer orange band). Also shown recently published [21] ATLAS results. The uncertainties of ABKM, JR09, HERAPDF and MSTW predictions correspond to the PDF uncertainties only.

(a) $W \to e\nu_e$

$\|\eta\|$	N^{DATA}	N^{QCD}	$N^{EW+t\bar{t}}$	C_W
(0.00 - 0.80)	44178 ± 210	$993 \pm 62 \pm 298$	$1524 \pm 22 \pm 79$	$0.6981 \pm 0.0011 \pm 0.0187$
(0.80 - 1.37)	31170 ± 177	$958 \pm 67 \pm 287$	$934 \pm 18 \pm 49$	$0.6626 \pm 0.0013 \pm 0.0205$
(1.52 - 2.01)	21191 ± 146	$777 \pm 75 \pm 233$	$656 \pm 15 \pm 34$	$0.5690 \pm 0.0016 \pm 0.0245$
(2.01 - 2.47)	17508 ± 132	$1510 \pm 192 \pm 453$	$507 \pm 13 \pm 26$	$0.5101 \pm 0.0017 \pm 0.0251$

(b) $W^+ \to e^+\nu_e$

$\|\eta\|$	N^{DATA}	N^{QCD}	$N^{EW+t\bar{t}}$	C_W
(0.00 - 0.80)	25323 ± 159	$451 \pm 41 \pm 135$	$831 \pm 17 \pm 43$	$0.7000 \pm 0.0014 \pm 0.0185$
(0.80 - 1.37)	18549 ± 136	$483 \pm 50 \pm 145$	$511 \pm 13 \pm 27$	$0.6611 \pm 0.0017 \pm 0.0204$
(1.52 - 2.01)	13063 ± 114	$354 \pm 49 \pm 106$	$381 \pm 12 \pm 20$	$0.5714 \pm 0.0020 \pm 0.0243$
(2.01 - 2.47)	11006 ± 105	$845 \pm 164 \pm 254$	$315 \pm 10 \pm 16$	$0.5098 \pm 0.0022 \pm 0.0244$

(c) $W^- \to e^-\bar{\nu}_e$

$\|\eta\|$	N^{DATA}	N^{QCD}	$N^{EW+t\bar{t}}$	C_W
(0.00 - 0.80)	18855 ± 137	$539 \pm 46 \pm 162$	$693 \pm 15 \pm 36$	$0.6957 \pm 0.0016 \pm 0.0190$
(0.80 - 1.37)	12621 ± 112	$467 \pm 45 \pm 140$	$423 \pm 12 \pm 22$	$0.6646 \pm 0.0020 \pm 0.0207$
(1.52 - 2.01)	8128 ± 90	$429 \pm 58 \pm 129$	$275 \pm 10 \pm 14$	$0.5650 \pm 0.0025 \pm 0.0249$
(2.01 - 2.47)	6502 ± 81	$691 \pm 119 \pm 207$	$192 \pm 8 \pm 10$	$0.5104 \pm 0.0028 \pm 0.0264$

Table 7.9: Inputs to the differential cross section measurement in $W \to e\nu_e$ channel, separated in $W^{\pm}$, W^+ and W^-. The first error is due to statistical effects, while the second is due to systematics. The integrated luminosity is $L = 35.1 \pm 1.2\, pb^{-1}$.

$\|\eta\|$	$d\sigma_W^{fid}/d\|\eta\|$	$d\sigma_{W+}^{fid}/d\|\eta\|$	$d\sigma_{W-}^{fid}/d\|\eta\|$
(0.00 - 0.80)	$1.063 \pm 0.006 \pm 0.035$	$0.612 \pm 0.004 \pm 0.020$	$0.451 \pm 0.004 \pm 0.015$
(0.80 - 1.37)	$1.104 \pm 0.007 \pm 0.041$	$0.664 \pm 0.006 \pm 0.025$	$0.441 \pm 0.005 \pm 0.016$
(1.52 - 2.01)	$1.010 \pm 0.009 \pm 0.047$	$0.627 \pm 0.007 \pm 0.029$	$0.382 \pm 0.006 \pm 0.018$
(2.01 - 2.47)	$0.941 \pm 0.015 \pm 0.050$	$0.598 \pm 0.012 \pm 0.032$	$0.341 \pm 0.009 \pm 0.019$

Table 7.10: Differential $W \to e\nu_e$ cross-sections in the fiducial volume. Quoted errors are due to statistical and systematic weights, in that order. All cross-sections are given in nb.

7.6 W Boson Charge Asymmetry

It was indicated in Chapter 2 that W^+ (W^-) boson production relies predominantly on the underlying distributions of u and $\bar{d}$ (d and $\bar{u}$). Therefore in principle, measurement of the W charge asymmetry, defined as:

$$A_e(|\eta|) = \frac{d\sigma_{W+}^{fid}/d|\eta| - d\sigma_{W-}^{fid}/d|\eta|}{d\sigma_{W+}^{fid}/d|\eta| + d\sigma_{W-}^{fid}/d|\eta|}, \tag{7.5}$$

could explore the difference between relative shapes of u and d quarks distributions. The η differential W asymmetry measurement, conducted in the fiducial region of this analysis is shown in Figure 7.10. Also shown is the published ATLAS result [21] together with $NNLO$ predictions obtained in the combined lepton channel. Despite differences in the chosen binning it is clearly compatible with the measured W charge asymmetry. Nevertheless the measurement of $A_e(|\eta|)$ conducted in the thesis in not sensitive enough to provide additional information regarding respective quark distributions.

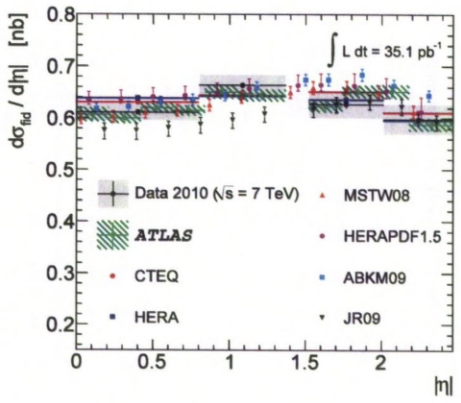

(a) W^+

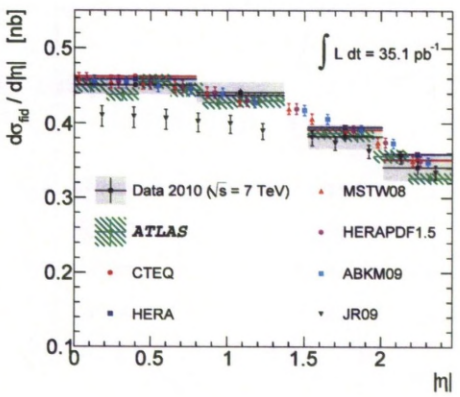

(b) W^-

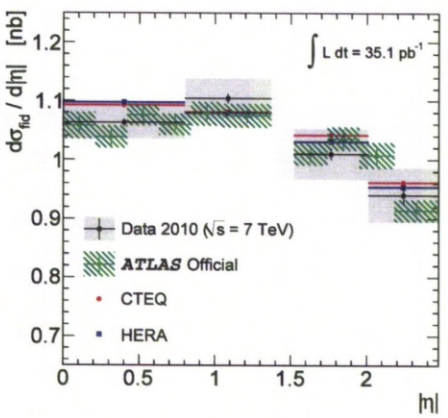

(c) $W^{\pm}$

Figure 7.8: Measured differential $d\sigma/d|\eta|$ for $W \to e\nu_e$ within the fiducial region compared with the most recent ATLAS result. Also shown theoretical prediction from HERAPDF1.0 *and* CTEQ6.6 *available at NLO, and* MSTW08, HERAPDF1.5, ABKM09 *and* JR09 *NNLO predictions, with the uncertainties purely from the PDF uncertainties. Both NLO predictions are normalized to the total cross section value calculated at NNLO. The error bars on the measurements represent uncertainties due to statistical effects and the shaded area shows the systematic uncertainties. For clarity the theoretical NNLO points are displaced within each $|\eta|$ bin. The kinematic requirements are $p_{T,e} > 20$GeV, $p_{T,\nu} > 25$GeV, $m_T > 40$GeV.*

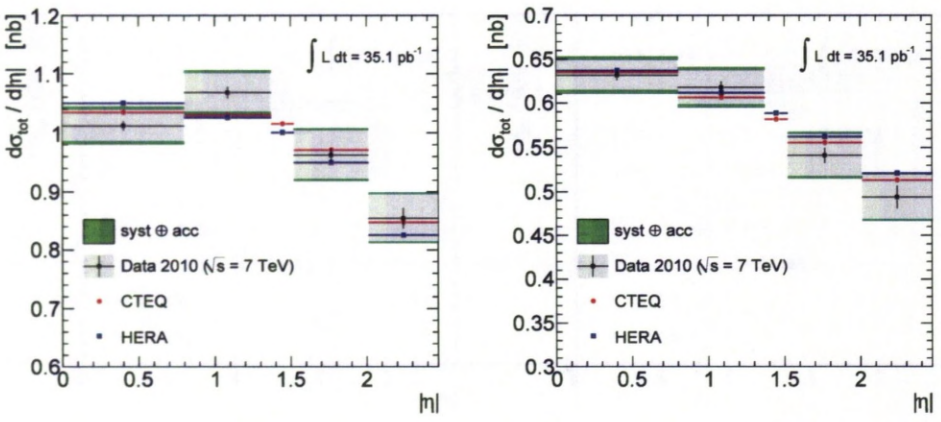

(a) W^+ (b) W^-

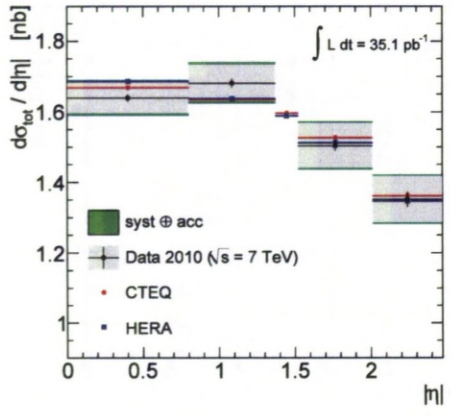

(c) $W^{\pm}$

Figure 7.9: Measured and predicted total differential $d\sigma_W/d|\eta|$ cross sections for $W \to e\nu_e$ channel. Theory estimates based on parton distribution sets from HERAPDF1.0 *and* CTEQ6.6 *available at NLO, normalized to $NNLO$ prediction. Theory error bars show the uncertainties purely from PDF uncertainties. The error bars on the measurement represent uncertainties due to statistical effects and shaded area shows the systematic uncertainties. Also shown combined uncertainty due to systematic effects (syst) and acceptance extrapolation (acc) to the full kinematic range, i.e. from A_W estimate at the generator level.*

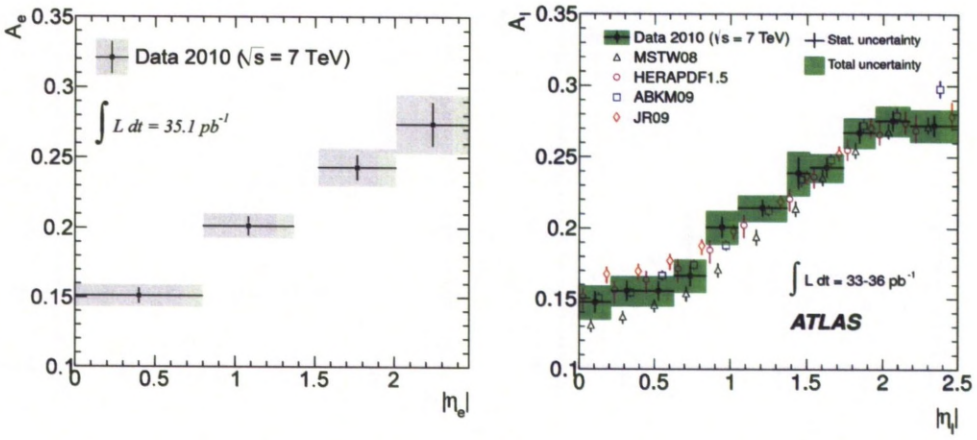

Figure 7.10: Measured (left) and published by ATLAS *(right) W charge asymmetry as a function of electron and lepton $|\eta|$, respectively. The kinematical requirements are $p_{T,e} > 20\,\text{GeV}$, $p_{T,\nu} > 25\,\text{GeV}$, and $m_\text{T} > 40\,\text{GeV}$.*

Chapter 8

Conclusions

This thesis has presented a study of the 2010 ATLAS data on inclusive $W^{\pm}$ production in the electron decay channel. Based on a reconstruction software version preceding the one in the corresponding ATLAS publication, an analysis has been pursued to cross-check the official result on the total and the fiducial integrated cross section, and as a function of the electron pseudorapidity. Special attention was given to understanding the background from QCD sources. The result, in different η_e bins, confirms the publication within the somewhat larger errors of the present analysis given the larger uncertainties mainly in the missing energy reconstruction and electron reconstruction and identification. The measured cross sections are broadly consistent with $pQCD$ predictions obtained for the ATLAS publication in $NNLO$, and within the present thesis using MC@NLO and PYTHIA Monte Carlo programs and further PDFs. A future even more precise measurement of the inclusive W production process with ATLAS will allow genuine constraints to be obtained on the parton distributions in the proton in the corresponding region of Bjorken x around 0.01 and for $Q^2 \simeq M_W^2$.

Appendix A

ABCD Method

A.1 Differential Inputs

This is a summary of the inputs required for the derivation of the *QCD* data driven template with the *ABCD* method, presented differentially in pseudorapidity η of an electron candidate, for $W^{\pm}$ and differentiated into respective W boson charges, W^{+} and W^{-}.

A.2 Stability of the *QCD* model

The plots summarize performance of the *ABCD* method in a case of large background contamination due to relaxed electron *ID* requirement. Shown for electron candidate m_{T} distribution, differentially in each lepton pseudorapidity bin and with differentiation into respective W boson charges. Table A.5 presents *QCD* background contamination as a relative fraction of observed W boson candidate events. For the $W^{+} \rightarrow e^{+}\nu_{e}$ there is observed an asymmetry of the *QCD* estimate at the edges of acceptance (see Figure A.1(a) and Figure A.1(h)). Nevertheless inspection of the statistical uncertainties (see Table A.5) proves that *QCD* model agree within $\approx 2\sigma$ fluctuation, which is sufficient for the stability as well as the cross section measurement.

(a) $W \to e\nu_e$

η	c_A	c_B	c_C
(-2.47 - -2.01)	0.01061 ± 0.00068	0.00003 ± 0.00003	0.00307 ± 0.00036
(-2.01 - -1.52)	0.01335 ± 0.00071	0.00015 ± 0.00008	0.00526 ± 0.00044
(-1.52 - -1.37)			
(-1.37 - -0.80)	0.01737 ± 0.00070	0.00006 ± 0.00002	0.00330 ± 0.00029
(-0.80 - 0.00)	0.01711 ± 0.00056	0.00018 ± 0.00005	0.00284 ± 0.00024
(0.00 - 0.80)	0.01803 ± 0.00053	0.00009 ± 0.00002	0.00300 ± 0.00021
(0.80 - 1.37)	0.01726 ± 0.00066	0.00015 ± 0.00006	0.00317 ± 0.00027
(1.37 - 1.52)			
(1.52 - 2.01)	0.01235 ± 0.00067	0.00009 ± 0.00005	0.00459 ± 0.00041
(2.01 - 2.47)	0.01054 ± 0.00069	0.00012 ± 0.00008	0.00300 ± 0.00036

(b) $W^+ \to e^+\nu_e$

η	c_A	c_B	c_C
(-2.47 - -2.01)	0.00994 ± 0.00083	0.00005 ± 0.00004	0.00255 ± 0.00040
(-2.01 - -1.52)	0.01425 ± 0.00095	0.00022 ± 0.00012	0.00429 ± 0.00050
(-1.52 - -1.37)			
(-1.37 - -0.80)	0.01959 ± 0.00098	0.00003 ± 0.00001	0.00312 ± 0.00038
(-0.80 - 0.00)	0.02017 ± 0.00083	0.00023 ± 0.00009	0.00277 ± 0.00030
(0.00 - 0.80)	0.02003 ± 0.00076	0.00006 ± 0.00002	0.00310 ± 0.00030
(0.80 - 1.37)	0.01875 ± 0.00090	0.00016 ± 0.00007	0.00346 ± 0.00038
(1.37 - 1.52)			
(1.52 - 2.01)	0.01310 ± 0.00090	0.00012 ± 0.00008	0.00416 ± 0.00048
(2.01 - 2.47)	0.01114 ± 0.00089	0.00017 ± 0.00013	0.00354 ± 0.00050

(c) $W^- \to e^-\bar{\nu}_e$

η	c_A	c_B	c_C
(-2.47 - -2.01)	0.01176 ± 0.00118	-0.00001 ± -0.00001	0.00398 ± 0.00069
(-2.01 - -1.52)	0.01193 ± 0.00107	0.00002 ± 0.00001	0.00681 ± 0.00082
(-1.52 - -1.37)			
(-1.37 - -0.80)	0.01424 ± 0.00096	0.00010 ± 0.00005	0.00355 ± 0.00047
(-0.80 - 0.00)	0.01319 ± 0.00073	0.00010 ± 0.00005	0.00293 ± 0.00037
(0.00 - 0.80)	0.01548 ± 0.00073	0.00012 ± 0.00004	0.00289 ± 0.00030
(0.80 - 1.37)	0.01518 ± 0.00095	0.00014 ± 0.00010	0.00277 ± 0.00039
(1.37 - 1.52)			
(1.52 - 2.01)	0.01116 ± 0.00100	0.00003 ± 0.00001	0.00528 ± 0.00072
(2.01 - 2.47)	0.00953 ± 0.00108	0.00003 ± 0.00001	0.00208 ± 0.00049

Table A.1: Collection of lepton η differential correction coefficients c_i for different regions i (i = A,B,or C) from Equation 6.5, differentiated into W charges. The uncertainties are statistical only.

(a) region A

η	N_A^{DATA}	N_A^{SIG}	$N_A^{EW+t\bar{t}}$	$\sum_{N_A^{SIG}+N_A^{EW+t\bar{t}}}$
(-2.47 - -2.01)	273	55.72 ± 4.57	33.39 ± 3.39	89.11 ± 5.69
(-2.01 - -1.52)	381	81.77 ± 5.73	54.14 ± 4.40	135.91 ± 7.22
(-1.52 - -1.37)				
(-1.37 - -0.80)	719	149.01 ± 7.76	87.55 ± 5.39	236.56 ± 9.45
(-0.80 - 0.00)	1097	229.51 ± 9.64	117.40 ± 5.97	346.91 ± 11.34
(0.00 - 0.80)	1242	271.83 ± 10.32	147.97 ± 6.70	419.8 ± 12.30
(0.80 - 1.37)	807	174.21 ± 8.48	96.37 ± 5.67	270.58 ± 10.20
(1.37 - 1.52)				
(1.52 - 2.01)	408	86.89 ± 5.98	46.02 ± 3.99	132.91 ± 7.19
(2.01 - 2.47)	237	52.04 ± 4.34	31.49 ± 3.30	83.53 ± 5.45
(-2.47 - 2.47)	5164	1100.98 ± 20.97	614.33 ± 14.12	1715.31 ± 25.28

(b) region B

η	N_B^{DATA}	N_B^{SIG}	$N_B^{EW+t\bar{t}}$	$\sum_{N_B^{SIG}+N_B^{EW+t\bar{t}}}$
(-2.47 - -2.01)	57	0.22 ± 0.22	0 ± 0.04	0.22 ± 0.22
(-2.01 - -1.52)	147	0.86 ± 0.65	0.63 ± 0.41	1.49 ± 0.77
(-1.52 - -1.37)				
(-1.37 - -0.80)	320	0 ± 0	0.76 ± 0.28	0.76 ± 0.28
(-0.80 - 0.00)	497	2.07 ± 0.99	1.48 ± 0.5	3.55 ± 1.11
(0.00 - 0.80)	574	0.83 ± 0.48	1.2 ± 0.17	2.03 ± 0.51
(0.80 - 1.37)	377	1.09 ± 0.65	1.27 ± 0.63	2.36 ± 0.91
(1.37 - 1.52)				
(1.52 - 2.01)	194	0.74 ± 0.53	0.2 ± 0.08	0.94 ± 0.54
(2.01 - 2.47)	73	0.86 ± 0.63	0.08 ± 0.04	0.94 ± 0.63
(-2.47 - 2.47)	2239	6.67 ± 1.67	5.62 ± 0.97	12.29 ± 1.93

(c) region C

η	N_C^{DATA}	N_C^{SIG}	$N_C^{EW+t\bar{t}}$	$\sum_{N_C^{SIG}+N_C^{EW+t\bar{t}}}$
(-2.47 - -2.01)	311	23.98 ± 2.89	1.84 ± 0.82	25.82 ± 3.00
(-2.01 - -1.52)	312	51.37 ± 4.4	2.14 ± 0.56	53.51 ± 4.44
(-1.52 - -1.37)				
(-1.37 - -0.80)	341	40.62 ± 3.91	4.32 ± 0.88	44.94 ± 4.01
(-0.80 - 0.00)	376	52.42 ± 4.68	5.13 ± 0.87	57.55 ± 4.76
(0.00 - 0.80)	420	63.9 ± 4.94	6.06 ± 0.62	69.96 ± 4.98
(0.80 - 1.37)	420	44.06 ± 4.16	5.69 ± 1	49.75 ± 4.28
(1.37 - 1.52)				
(1.52 - 2.01)	281	46.59 ± 4.29	2.78 ± 0.77	49.37 ± 4.36
(2.01 - 2.47)	289	23 ± 2.86	0.77 ± 0.32	23.77 ± 2.88
(-2.47 - 2.47)	2750	345.94 ± 11.54	28.73 ± 2.14	374.67 ± 11.74

(d) region D

η	N_D^{DATA}	N_D^{SIG}	$N_D^{EW+t\bar{t}}$	$\sum_{N_D^{SIG}+N_D^{EW+t\bar{t}}}$
(-2.47 - -2.01)	8938	8130.59 ± 54.99	266.52 ± 9.51	8397.11 ± 55.81
(-2.01 - -1.52)	10582	9860.31 ± 62.89	316.62 ± 10.4	10176.93 ± 63.74
(-1.52 - -1.37)		±	±	±
(-1.37 - -0.80)	14635	13181.41 ± 73.16	439.03 ± 12.1	13620.44 ± 74.15
(-0.80 - 0.00)	20779	19558.14 ± 88.12	719.65 ± 15.23	20277.79 ± 89.43
(0.00 - 0.80)	23399	22478.19 ± 94.65	804.2 ± 16.06	23282.39 ± 96.00
(0.80 - 1.37)	16535	15180.66 ± 79.65	495.35 ± 13.06	15676.01 ± 80.71
(1.37 - 1.52)		±	±	±
(1.52 - 2.01)	10609	10420.44 ± 65.71	339.25 ± 11.04	10759.69 ± 66.63
(2.01 - 2.47)	8570	7682.4 ± 53.96	240.35 ± 8.95	7922.75 ± 54.70
(-2.47 - 2.47)	114047	106492.14 ± 206.47	3620.97 ± 34.75	110113.11 ± 209.37

Table A.2: $W \to e\nu_e$ differential inputs for the QCD data - driven estimation in the background dominated A, B, C and signal D regions. The uncertainties are statistical only.

(a) region A

η	N_A^{DATA}	N_A^{SIG}	$N_A^{EW+t\bar{t}}$	$\sum_{N_A^{SIG}+N_A^{EW+t\bar{t}}}$
(-2.47 - -2.01)	156	30.57 ± 3.43	22.15 ± 2.74	52.72 ± 4.39
(-2.01 - -1.52)	211	52.82 ± 4.6	36.52 ± 3.73	89.34 ± 5.92
(-1.52 - -1.37)				
(-1.37 - -0.80)	365	100.83 ± 6.41	55.15 ± 4.35	155.98 ± 7.75
(-0.80 - 0.00)	561	157.55 ± 8.01	72.03 ± 4.8	229.58 ± 9.34
(0.00 - 0.80)	659	178.32 ± 8.37	82.98 ± 5.07	261.3 ± 9.79
(0.80 - 1.37)	432	114.99 ± 6.83	56.08 ± 4.37	171.07 ± 8.11
(1.37 - 1.52)				
(1.52 - 2.01)	227	57.11 ± 4.93	29.58 ± 3.25	86.69 ± 5.90
(2.01 - 2.47)	120	31.26 ± 3.35	24.29 ± 2.9	55.55 ± 4.43
(-2.47 - 2.47)	2731	723.45 ± 17.04	378.78 ± 11.28	1102.23 ± 20.43

(b) region B

η	N_B^{DATA}	N_B^{SIG}	$N_B^{EW+t\bar{t}}$	$\sum_{N_B^{SIG}+N_B^{EW+t\bar{t}}}$
(-2.47 - -2.01)	27	0.22 ± 0.22	0.02 ± 0.02	0.24 ± 0.22
(-2.01 - -1.52)	82	0.86 ± 0.65	0.54 ± 0.41	1.4 ± 0.77
(-1.52 - -1.37)				
(-1.37 - -0.80)	153	0 ± 0	0.21 ± 0.07	0.21 ± 0.07
(-0.80 - 0.00)	253	1.84 ± 0.96	0.8 ± 0.29	2.64 ± 1.00
(0.00 - 0.80)	288	0.26 ± 0.26	0.55 ± 0.12	0.81 ± 0.29
(0.80 - 1.37)	179	1.09 ± 0.65	0.33 ± 0.1	1.42 ± 0.66
(1.37 - 1.52)				
(1.52 - 2.01)	104	0.74 ± 0.53	0.08 ± 0.04	0.82 ± 0.53
(2.01 - 2.47)	41	0.86 ± 0.63	0 ± 0	0.86 ± 0.63
(-2.47 - 2.47)	1127	5.87 ± 1.60	2.53 ± 0.53	8.40 ± 1.69

(c) region C

η	N_C^{DATA}	N_C^{SIG}	$N_C^{EW+t\bar{t}}$	$\sum_{N_C^{SIG}+N_C^{EW+t\bar{t}}}$
(-2.47 - -2.01)	168	13.02 ± 2.09	0.49 ± 0.23	13.51 ± 2.10
(-2.01 - -1.52)	162	25.49 ± 3.06	1.44 ± 0.53	26.93 ± 3.11
(-1.52 - -1.37)				
(-1.37 - -0.80)	184	22.35 ± 2.89	2.5 ± 0.8	24.85 ± 3.00
(-0.80 - 0.00)	198	28.9 ± 3.39	2.57 ± 0.67	31.47 ± 3.46
(0.00 - 0.80)	212	37.66 ± 3.85	2.75 ± 0.48	40.41 ± 3.88
(0.80 - 1.37)	229	28.39 ± 3.34	3.18 ± 0.85	31.57 ± 3.45
(1.37 - 1.52)				
(1.52 - 2.01)	136	25.97 ± 3.17	1.56 ± 0.43	27.53 ± 3.20
(2.01 - 2.47)	165	17.11 ± 2.47	0.54 ± 0.31	17.65 ± 2.49
(-2.47 - 2.47)	1454	198.89 ± 8.70	15.03 ± 1.63	213.92 ± 8.85

(d) region D

η	N_D^{DATA}	N_D^{SIG}	$N_D^{EW+t\bar{t}}$	$\sum_{N_D^{SIG}+N_D^{EW+t\bar{t}}}$
(-2.47 - -2.01)	5611	5138.72 ± 43.73	164.6 ± 7.56	5303.32 ± 44.38
(-2.01 - -1.52)	6528	6089.67 ± 49.37	181.37 ± 8.01	6271.04 ± 50.02
(-1.52 - -1.37)	0	0 ± 0	0 ± 0	±
(-1.37 - -0.80)	8677	7729.77 ± 56.1	233.24 ± 8.8	7963.01 ± 56.79
(-0.80 - 0.00)	11834	10990.52 ± 66.01	390.86 ± 11.35	11381.38 ± 66.98
(0.00 - 0.80)	13489	12603.63 ± 71.02	439.8 ± 12.02	13043.43 ± 72.03
(0.80 - 1.37)	9872	8843.47 ± 60.73	278.07 ± 9.84	9121.54 ± 61.52
(1.37 - 1.52)	0	0 ± 0	0 ± 0	±
(1.52 - 2.01)	6535	6418.47 ± 51.65	199.94 ± 8.57	6618.41 ± 52.36
(2.01 - 2.47)	5395	4837.01 ± 42.87	149.91 ± 7.15	4986.92 ± 43.46
(-2.47 - 2.47)	67941	62651.26 ± 158.40	2037.79 ± 26.33	64689.05 ± 160.58

Table A.3: $W^+ \to e^+\nu_e$ differential inputs for the QCD data - driven estimation in the background dominated A, B, C and signal D regions. The uncertainties are statistical only.

(a) region A

η	N_A^{DATA}	N_A^{SIG}	$N_A^{EW+t\bar{t}}$	$\sum_{N_A^{SIG}+N_A^{EW+t\bar{t}}}$
(-2.47 - -2.01)	117	25.15 ± 3.01	11.24 ± 2	36.39 ± 3.61
(-2.01 - -1.52)	170	28.95 ± 3.42	17.63 ± 2.35	46.58 ± 4.15
(-1.52 - -1.37)				
(-1.37 - -0.80)	354	48.17 ± 4.37	32.4 ± 3.19	80.57 ± 5.41
(-0.80 - 0.00)	536	71.96 ± 5.36	45.37 ± 3.54	117.33 ± 6.42
(0.00 - 0.80)	583	93.51 ± 6.03	64.99 ± 4.38	158.5 ± 7.45
(0.80 - 1.37)	375	59.22 ± 5.03	40.29 ± 3.62	99.51 ± 6.20
(1.37 - 1.52)				
(1.52 - 2.01)	181	29.78 ± 3.39	16.44 ± 2.33	46.22 ± 4.11
(2.01 - 2.47)	117	20.78 ± 2.75	7.19 ± 1.57	27.97 ± 3.17
(-2.47 - 2.47)	2433	377.52 ± 12.22	235.55 ± 8.51	613.07 ± 14.89

(b) region B

η	N_B^{DATA}	N_B^{SIG}	$N_B^{EW+t\bar{t}}$	$\sum_{N_B^{SIG}+N_B^{EW+t\bar{t}}}$
(-2.47 - -2.01)	30	0 ± 0	-0.02 ± 0.03	-0.02 ± 0.03
(-2.01 - -1.52)	65	0 ± 0	0.09 ± 0.05	0.09 ± 0.05
(-1.52 - -1.37)	0	0 ± 0	0 ± 0	0 ± 0.00
(-1.37 - -0.80)	167	0 ± 0	0.55 ± 0.27	0.55 ± 0.27
(-0.80 - 0.00)	244	0.23 ± 0.23	0.68 ± 0.41	0.91 ± 0.47
(0.00 - 0.80)	286	0.57 ± 0.41	0.65 ± 0.12	1.22 ± 0.43
(0.80 - 1.37)	198	0 ± 0	0.94 ± 0.63	0.94 ± 0.63
(1.37 - 1.52)	0	0 ± 0	0 ± 0	0 ± 0.00
(1.52 - 2.01)	90	0 ± 0	0.12 ± 0.06	0.12 ± 0.06
(2.01 - 2.47)	32	0 ± 0	0.08 ± 0.04	0.08 ± 0.04
(-2.47 - 2.47)	1112	0.8 ± 0.47	3.09 ± 0.81	3.89 ± 0.94

(c) region C

η	N_C^{DATA}	N_C^{SIG}	$N_C^{EW+t\bar{t}}$	$\sum_{N_C^{SIG}+N_C^{EW+t\bar{t}}}$
(-2.47 - -2.01)	143	10.95 ± 1.99	1.35 ± 0.79	12.3 ± 2.14
(-2.01 - -1.52)	150	25.88 ± 3.17	0.7 ± 0.15	26.58 ± 3.17
(-1.52 - -1.37)	0	0 ± 0	0 ± 0	0 ± 0.00
(-1.37 - -0.80)	157	18.27 ± 2.64	1.82 ± 0.38	20.09 ± 2.67
(-0.80 - 0.00)	178	23.51 ± 3.22	2.56 ± 0.56	26.07 ± 3.27
(0.00 - 0.80)	208	26.24 ± 3.08	3.31 ± 0.4	29.55 ± 3.11
(0.80 - 1.37)	191	15.67 ± 2.47	2.51 ± 0.54	18.18 ± 2.53
(1.37 - 1.52)	0	0 ± 0	0 ± 0	0 ± 0.00
(1.52 - 2.01)	145	20.63 ± 2.9	1.22 ± 0.63	21.85 ± 2.97
(2.01 - 2.47)	124	5.89 ± 1.44	0.23 ± 0.07	6.12 ± 1.44
(-2.47 - 2.47)	1296	147.04 ± 7.58	13.7 ± 1.40	160.74 ± 7.71

(d) region D

η	N_D^{DATA}	N_D^{SIG}	$N_D^{EW+t\bar{t}}$	$\sum_{N_D^{SIG}+N_D^{EW+t\bar{t}}}$
(-2.47 - -2.01)	3327	2991.87 ± 33.33	101.92 ± 5.78	3093.79 ± 33.83
(-2.01 - -1.52)	4054	3770.64 ± 38.96	135.25 ± 6.63	3905.89 ± 39.52
(-1.52 - -1.37)	0	0 ± 0	0 ± 0	±
(-1.37 - -0.80)	5958	5451.64 ± 46.96	205.78 ± 8.3	5657.42 ± 47.69
(-0.80 - 0.00)	8945	8567.62 ± 58.37	328.79 ± 10.15	8896.41 ± 59.25
(0.00 - 0.80)	9910	9874.56 ± 62.56	364.4 ± 10.65	10238.96 ± 63.46
(0.80 - 1.37)	6663	6337.19 ± 51.53	217.28 ± 8.58	6554.47 ± 52.24
(1.37 - 1.52)	0	0 ± 0	0 ± 0	±
(1.52 - 2.01)	4074	4001.97 ± 40.63	139.31 ± 6.96	4141.28 ± 41.22
(2.01 - 2.47)	3175	2845.39 ± 32.77	90.43 ± 5.39	2935.82 ± 33.21
(-2.47 - 2.47)	46106	43840.88 ± 132.42	1583.16 ± 22.67	45424.04 ± 134.35

Table A.4: $W^- \to e^-\bar{\nu}_e$ differential inputs for the QCD data - driven estimation in the background dominated A, B, C and signal D regions. The uncertainties are statistical only.

η	$W^{\pm}_{(stat)\pm(syst)}(\%)$	$W^{+}_{(stat)\pm(syst)}(\%)$	$W^{-}_{(stat)\pm(syst)}(\%)$
(-2.47 - -2.01)	37.53 ± 6.57 ± 11.26	38.18 ± 9.46 ± 11.45	37.72 ± 9.39 ± 11.32
(-2.01 - -1.52)	19.20 ± 2.66 ± 5.76	15.39 ± 3.03 ± 4.62	24.98 ± 4.88 ± 7.49
(-1.37 - -0.8)	14.84 ± 1.53 ± 4.45	11.57 ± 1.79 ± 3.47	19.24 ± 2.72 ± 5.77
(-0.8 - 0)	7.85 ± 0.71 ± 2.36	6.22 ± 0.82 ± 1.87	9.95 ± 1.24 ± 2.98
(0 - 0.8)	7.76 ± 0.67 ± 2.33	6.34 ± 0.80 ± 1.90	9.68 ± 1.14 ± 2.90
(0.8 - 1.37)	14.29 ± 1.36 ± 4.29	13.19 ± 1.83 ± 3.96	15.96 ± 2.09 ± 4.79
(1.52 - 2.01)	15.49 ± 2.01 ± 4.65	12.53 ± 2.36 ± 3.76	20.07 ± 3.60 ± 6.02
(2.01 - 2.47)	21.73 ± 3.74 ± 6.52	14.12 ± 3.66 ± 4.24	34.38 ± 8.17 ± 10.31
(-2.47 - 2.47)	15.81 ± 0.84 ± 4.74	13.48 ± 1.16 ± 4.04	19.32 ± 1.34 ± 5.80

Table A.5: The charge dependent estimate of the number of QCD events in the signal region (D), N_D^{QCD} for each lepton pseudorapidity bin, η, as a relative fraction of observed W boson candidate events, shown for the sample with large background increase, resulting from relaxed electron ID, used in cross-check analysis. The uncertainties are statistical and systematic (30%) in that order.

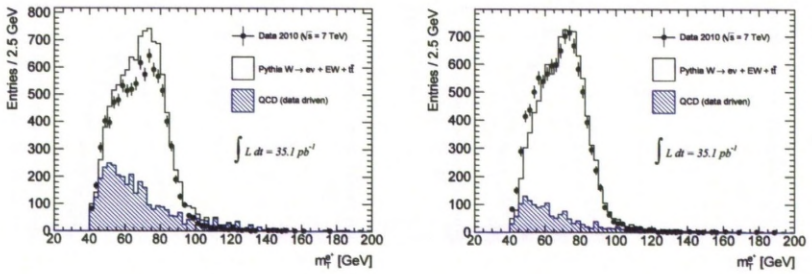

(a) $-2.47 < \eta < -2.01$ (b) $-2.01 < \eta < -1.52$

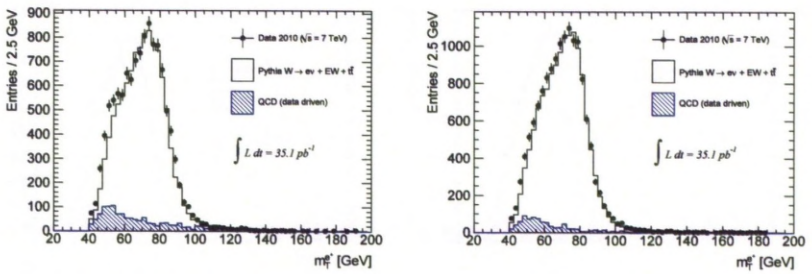

(c) $-1.37 < \eta < -0.8$ (d) $-0.8 < \eta < 0$

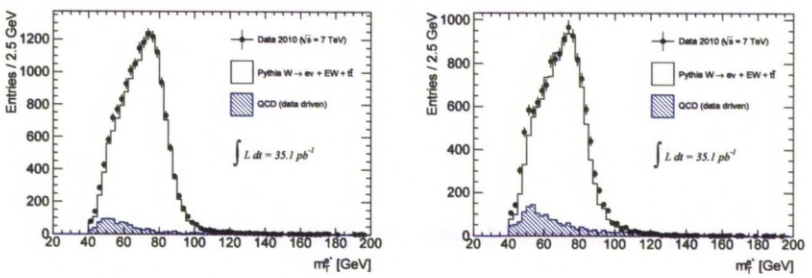

(e) $0 < \eta < 0.8$ (f) $0.8 < \eta < 1.37$

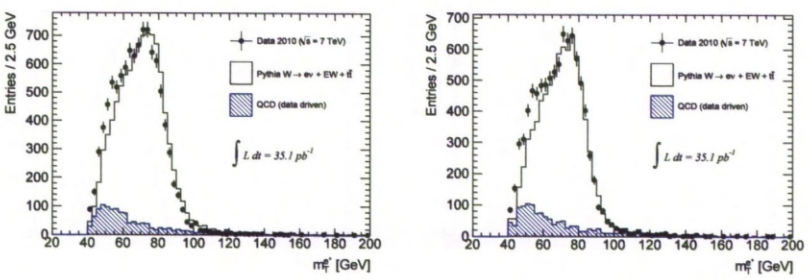

(g) $1.52 < \eta < 2.01$ (h) $2.01 < \eta < 2.47$

Figure A.1: QCD background for $W^+ \to e^+\nu_e$ in different electron η ranges, shown for m_T distribition. Performance of QCD data driven template derived for increased background sample, confirmed with MC template for the $W \to e\nu_e + EW + t\bar{t}$ and 2010 DATA

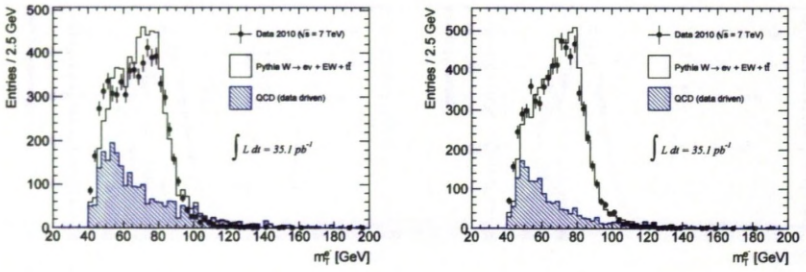

(a) $-2.47 < \eta < -2.01$

(b) $-2.01 < \eta < -1.52$

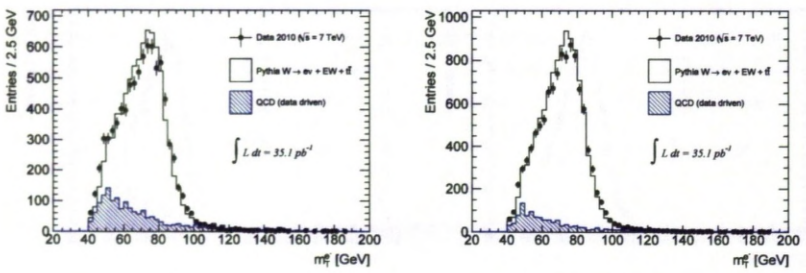

(c) $-1.37 < \eta < -0.8$

(d) $-0.8 < \eta < 0$

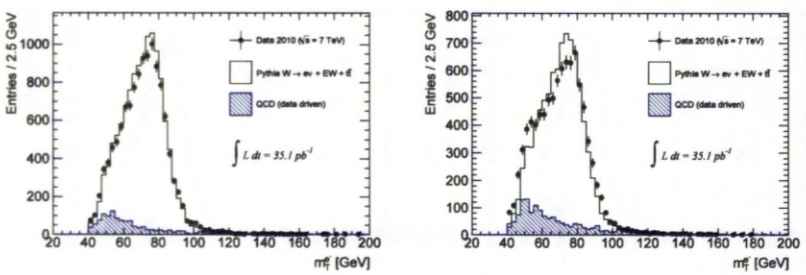

(e) $0 < \eta < 0.8$

(f) $0.8 < \eta < 1.37$

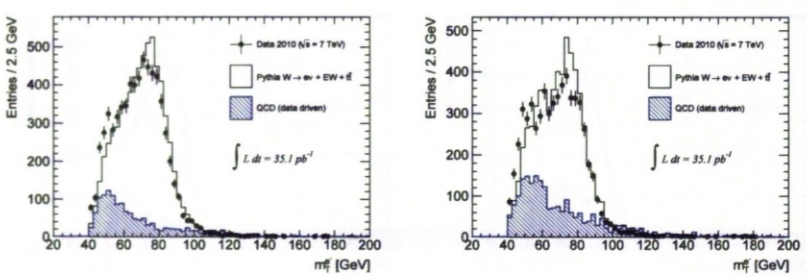

(g) $1.52 < \eta < 2.01$

(h) $2.01 < \eta < 2.47$

Figure A.2: QCD background for $W^- \to e^-\bar{\nu}_e$ in different electron η ranges, shown for m_T distribition. Performance of QCD data driven template derived for increased background sample, confirmed with MC template for the $W \to e\nu_e + EW + t\bar{t}$ and 2010 DATA

Appendix B

Summary of the official *ATLAS* W boson cross section measurement

B.1 Cross section results

[98] [21]

$$\sigma_{W}^{fid} \cdot BR(W \to e\nu) = 4.791 \pm 0.014(sta) \pm 0.089(sys) \pm 0.163(lum)\ [nb],$$
$$\sigma_{W^+}^{fid} \cdot BR(W \to e\nu) = 2.898 \pm 0.011(sta) \pm 0.052(sys) \pm 0.099(lum)\ [nb],$$
$$\sigma_{W^-}^{fid} \cdot BR(W \to e\nu) = 1.893 \pm 0.009(sta) \pm 0.038(sys) \pm 0.064(lum)\ [nb],$$

$$\sigma_{W}^{tot} \cdot BR(W \to e\nu) = 10.255 \pm 0.031(sta) \pm 0.190(sys) \pm 0.349(lum) \pm 0.156(acc)\ [nb],$$
$$\sigma_{W^+}^{tot} \cdot BR(W \to e\nu) = 6.063 \pm 0.023(sta) \pm 0.108(sys) \pm 0.206(lum) \pm 0.104(acc)\ [nb],$$
$$\sigma_{W^-}^{tot} \cdot BR(W \to e\nu) = 4.191 \pm 0.020(sta) \pm 0.085(sys) \pm 0.142(lum) \pm 0.084(acc)\ [nb],$$

B.2 Differential cross section results

η	$\Delta\sigma(W)/\Delta\lvert\eta\rvert$	$\Delta\sigma(W^+)/\Delta\lvert\eta\rvert$	$\Delta\sigma(W^-)/\Delta\lvert\eta\rvert$
0.00..0.21	$1057.9 \pm 15.0 \pm 22.5$	$607.0 \pm 11.2 \pm 13.7$	$450.6 \pm 9.7 \pm 9.1$
0.21..0.42	$1038.8 \pm 14.1 \pm 18.8$	$600.1 \pm 10.3 \pm 10.3$	$438.6 \pm 9.0 \pm 8.6$
0.42..0.63	$1076.1 \pm 14.1 \pm 18.2$	$620.3 \pm 10.3 \pm 10.0$	$455.7 \pm 9.0 \pm 9.3$
0.63..0.84	$1059.9 \pm 14.7 \pm 18.1$	$615.1 \pm 10.7 \pm 9.6$	$444.8 \pm 9.4 \pm 8.9$
0.84..1.05	$1078.2 \pm 14.7 \pm 20.3$	$650.7 \pm 10.9 \pm 12.8$	$427.6 \pm 9.1 \pm 8.3$
1.05..1.37	$1075.1 \pm 12.2 \pm 20.2$	$644.5 \pm 9.1 \pm 11.4$	$430.5 \pm 7.5 \pm 9.1$
1.37..1.52			
1.52..1.74	$1010.5 \pm 14.1 \pm 18.9$	$623.3 \pm 10.6 \pm 11.6$	$387.1 \pm 8.9 \pm 7.6$
1.74..1.95	$1036.1 \pm 15.5 \pm 19.7$	$652.0 \pm 11.6 \pm 12.1$	$384.2 \pm 9.1 \pm 7.9$
1.95..2.18	$1008.0 \pm 14.8 \pm 21.6$	$651.9 \pm 11.4 \pm 13.2$	$356.4 \pm 8.1 \pm 8.8$
2.18..2.47	$914.8 \pm 14.7 \pm 18.5$	$588.5 \pm 11.0 \pm 11.8$	$326.6 \pm 7.8 \pm 7.4$

Table B.1: Differential $W \to e\nu_e$ cross-sections in the fiducial volume. All cross-sections are given in pb [98] [21].

Appendix C

δC_W and δA_W

The statistical uncertainty on the efficiencies C_W and A_W can be derived considering $N_{MC,rec}$ and $N_{MC,gen,cut}$ in terms of successes of the binomial distribution for $N_{MC,gen,cut}$ and $N_{MC,gen,all}$ number of trials respectively:

$$P\left(N_{MC,rec}; C_{W,true}, N_{MC,gen,cut}\right) = \\ = \binom{N_{MC,gen,cut}}{N_{MC,rec}} C_{W,true}^{N_{MC,rec}} \left(1 - C_{W,true}\right)^{N_{MC,gen,cut} - N_{MC,rec}}$$

$$P\left(N_{MC,gen,cut}; A_{W,true}, N_{MC,gen,all}\right) = \\ = \binom{N_{MC,gen,all}}{N_{MC,gen,cut}} A_{W,true}^{N_{MC,gen,cut}} \left(1 - A_{W,true}\right)^{N_{MC,gen,all} - N_{MC,gen,cut}}$$

with expectation values $N_{MC,rec} = C_{W,true} \cdot N_{MC,gen,cut}$ and $N_{MC,gen,cut} = A_{W,true} \cdot N_{MC,gen,all}$ and variance $var\left(N_{MC,rec}\right) = C_{W,true} \cdot N_{MC,gen,cut}\left(1 - C_{W,true}\right)$ and $var\left(N_{MC,gen,cut}\right) = A_{W,true} \cdot N_{MC,gen,all}\left(1 - A_{W,true}\right)$
hence the corresponding standard deviations are:

$$s_{N_{MC,rec}} = \sqrt{var\left(N_{MC,rec}\right)} = \sqrt{C_{W,true} \cdot N_{MC,gen,cut}\left(1 - C_{W,true}\right)}$$

$$s_{N_{MC,gen,cut}} = \sqrt{var\left(N_{MC,gen,cut}\right)} = \sqrt{A_{W,true} \cdot N_{MC,gen,all}\left(1 - A_{W,true}\right)}$$

This can be expressed in terms of estimates for the efficiencies C_W and A_W which yields the equations Equation 7.4.

Appendix D

RooEllipse

The 2-dimensional ellipse [105] centered at (σ_{W-},σ_{W+}) represents the 68% confidence level contour for a measurement with (statistical and systematic) uncertainties ($\delta\sigma_{W-}$,$\delta\sigma_{W-}$) and the coefficient of linear dependence between the uncertainties ρ. The correlation coefficient is simply Pearson product-moment correlation coefficient:

$$\rho_{\delta\sigma_{W+},\delta\sigma_{W-}} = \frac{cov(\delta\sigma_{W+},\delta\sigma_{W-})}{s_{\delta\sigma_{W+}} \cdot s_{\delta\sigma_{W-}}} = \frac{\overline{\delta\sigma_{W+}\delta\sigma_{W-}} - \overline{\delta\sigma_{W+}} \cdot \overline{\delta\sigma_{W-}}}{\sqrt{\overline{\delta\sigma_{W+}^2} - \left(\overline{\delta\sigma_{W+}}\right)^2}\sqrt{\overline{\delta\sigma_{W-}^2} - \left(\overline{\delta\sigma_{W-}}\right)^2}}$$

where $\overline{X} = \sum_i X_i$ for $X = \delta\sigma_{W+}$, $\delta\sigma_{W-}$ The resulting curve is defined as the unique ellipse passing through the following points:

$$\left(\sigma_{W-} + \rho \cdot \delta\sigma_{W-}, \sigma_{W+} + \delta\sigma_{W+}\right), \left(\sigma_{W-} - \rho \cdot \delta\sigma_{W-}, \sigma_{W+} - \delta\sigma_{W+}\right),$$
$$\left(\sigma_{W-} + \delta\sigma_{W-}, \sigma_{W+} + \rho \cdot \delta\sigma_{W+}\right), \left(\sigma_{W-} - \delta\sigma_{W-}, \sigma_{W+} - \rho \cdot \delta\sigma_{W+}\right)$$

and is described by:

$$\frac{\sigma_{W-}^2}{\delta\sigma_{W-}\delta\sigma_{W+}} - \frac{2\rho\sigma_{W-}\sigma_{W+}}{\delta\sigma_{W-}\delta\sigma_{W+}} + \frac{\sigma_{W+}^2}{\delta\sigma_{W-}\delta\sigma_{W+}} = 1 - \rho^2$$

Therefore, in case of fully correlated $\rho = 1$ (anti-correlated $\rho = -1$) uncertainties the result is a straight line and for uncorrelated case $\rho = 0$ the ellipse whose major and minor axes coincide with the Cartesian axes.

Bibliography

[1] **UA1** Collaboration, G. Arnison *et al.*, "Experimental observation of isolated large transverse energy electrons with associated missing energy at $\sqrt{s} = 540$ GeV," *Phys. Lett.* **B122** (1983) 103–116.

[2] **UA1** Collaboration, G. Arnison *et al.*, "Experimental observation of lepton pairs of invariant mass around 95 GeV/c^2 at the CERN SPS collider," *Phys. Lett.* **B126** (1983) 398–410.

[3] **The UA1** Collaboration, C. Albajar *et al.*, "Intermediate vector boson cross-sections at the cern super proton synchrotron collider and the number of neutrino types," *Phys. Lett.* **B198** (1987) 271.

[4] **UA2** Collaboration, M. Banner *et al.*, "Observation of single isolated electrons of high transverse momentum in events with missing transverse energy at the CERN $\overline{p}p$ collider," *Phys. Lett.* **B122** (1983) 476–485.

[5] **UA2** Collaboration, P. Bagnaia *et al.*, "Evidence for $Z^o \rightarrow e^+ e^-$ at the CERN $\bar{p}p$ collider," *Phys. Lett.* **B129** (1983) 130–140.

[6] **The UA2** Collaboration, J. Alitti *et al.*, "A measurement of the w and z production cross-sections and a determination of gamma (w) at the cern $\overline{p}p$," *Phys. Lett.* **B276** (1992) 365–374.

[7] **CDF** Collaboration, F. Abe *et al.*, "Measurement of $\sigma \cdot B(W \rightarrow e\nu)$ and $\sigma \cdot B(Z^0 \rightarrow e^+e^-)$ in $p\bar{p}$ collisions at $\sqrt{s} = 1.8$ TeV," *Phys. Rev. Lett.* **76** (1996) 3070–3075, `arXiv:hep-ex/9509010`.

[8] **CDF** Collaboration, F. Abe *et al.*, "Measurement of Z^0 and Drell-Yan production cross section using dimuons in $\bar{p}p$ collisions at $\sqrt{s} = 1.8$ TeV," *Phys. Rev.* **D59** (1999) 052002.

[9] **CDF** Collaboration, A. Abulencia *et al.*, "Measurements of Inclusive W and Z Cross-sections in $p\bar{p}$ Collisions at $\sqrt{s} = 1.96$ TeV," *J. Phys.* **G34** (2007) 2457–2544, `arXiv:hep-ex/0508029`.

[10] **The D0** Collaboration, B. Abbott *et al.*, "Measurement of W and Z boson production cross sections," *Phys. Rev.* **D60** (1999) 052003, `arXiv:hep-ex/9901040`.

[11] **The D0** Collaboration, B. Abbott *et al.*, "Extraction of the width of the W boson from measurements of $\sigma(p\bar{p} \to W + X) \times B(W \to e\nu)$ and $\sigma(p\bar{p} \to Z + X) \times B(Z \to ee)$ and their ratio," *Phys. Rev.* **D61** (2000) 072001, `arXiv:hep-ex/9906025`.

[12] **The D0** Collaboration. D0 conference notes: 4403-CONF, 4750-CONF.

[13] J. Kubar and F. E. Paige, "Gluon Corrections to the Drell-Yan Model," *Phys. Rev.* **D19** (1979) 221.

[14] G. Altarelli, R. K. Ellis, and G. Martinelli, "Large Perturbative Corrections to the Drell-Yan Process in QCD," *Nucl. Phys.* **B157** (1979) 461.

[15] J. Kubar, M. Le Bellac, J. L. Meunier, and G. Plaut, "QCD Corrections to the Drell-Yan Mechanism and the Pion Structure Function," *Nucl. Phys.* **B175** (1980) 251.

[16] P. J. Rijken and W. L. van Neerven, "Order α_s^2 contributions to the Drell-Yan cross- section at fixed target energies," *Phys. Rev.* **D51** (1995) 44–63, arXiv:hep-ph/9408366.

[17] R. Hamberg, W. L. van Neerven, and T. Matsuura, "A Complete calculation of the order α_s^2 correction to the Drell-Yan K factor," *Nucl. Phys.* **B359** (1991) 343–405.

[18] W. L. van Neerven and E. B. Zijlstra, "The $\mathcal{O}(\alpha_s^2)$ corrected Drell-Yan K factor in the DIS and MS scheme," *Nucl. Phys.* **B382** (1992) 11–62.

[19] R. V. Harlander and W. B. Kilgore, "Next-to-next-to-leading order Higgs production at hadron colliders," *Phys. Rev. Lett.* **88** (2002) 201801, arXiv:hep-ph/0201206.

[20] C. Anastasiou, L. J. Dixon, K. Melnikov, and F. Petriello, "High precision QCD at hadron colliders: Electroweak gauge boson rapidity distributions at NNLO," *Phys. Rev.* **D69** (2004) 094008, arXiv:hep-ph/0312266.

[21] **ATLAS Collaboration** Collaboration, G. Aad *et al.*, "Measurement of the inclusive W+- and Z/gamma cross sections in the electron and muon decay channels in pp collisions at sqrt(s) = 7 TeV with the ATLAS detector," *Phys.Rev.* **D85** (2012) 072004, arXiv:1109.5141 [hep-ex].

[22] M. Aharrouche *et al.*, "Double differential Z, W cross sections and their ratios in the electron channels," Tech. Rep. ATL-PHYS-INT-2011-081, CERN, Geneva, Oct, 2011.

[23] S. D. Drell and T.-M. Yan, "Massive Lepton Pair Production in Hadron-Hadron Collisions at High-Energies," *Phys. Rev. Lett.* **25** (1970) 316–320.

[24] **H1 and ZEUS Collaboration** Collaboration, F. Aaron *et al.*, "Combined Measurement and QCD Analysis of the Inclusive e+- p Scattering Cross Sections at HERA," *JHEP* **1001** (2010) 109, arXiv:0911.0884 [hep-ex].

[25] **H1** Collaboration, F. D. Aaron *et al.*, "A Precision Measurement of the Inclusive ep Scattering Cross Section at HERA," *Eur. Phys. J.* **C64** (2009) 561–587, arXiv:0904.3513 [hep-ex].

[26] P. M. Nadolsky *et al.*, "Implications of CTEQ global analysis for collider observables," *Phys. Rev.* **D78** (2008) 013004, arXiv:0802.0007 [hep-ph].

[27] S. M. T. Sjostrand and P. Skands, "Brief Introduction to PYTHIA 8.1," *Comput. Phys. Comm.* **178** (2008) 85, arXiv:0710.3820v1 [hep-ph].

[28] S. Frixione and B. R. Webber, "Matching NLO QCD computations and parton shower simulations," *JHEP* **06** (2002) 029, arXiv:hep-ph/0204244.

[29] S. Frixione, P. Nason, and C. Oleari, "Matching NLO QCD computations with Parton Shower simulations: the POWHEG method," *JHEP* **11** (2007) 070, arXiv:0709.2092 [hep-ph].

[30] S. Frixione and B. R. Webber, "The MC@NLO 3.4 Event Generator," arXiv:0812.0770 [hep-ph].

[31] A. Sherstnev and R. S. Thorne, "Different PDF approximations useful for LO Monte Carlo generators," arXiv:0807.2132 [hep-ph].

[32] A. D. Martin, W. J. Stirling, R. S. Thorne, and G. Watt, "Parton distributions for the LHC," *Eur. Phys. J.* **C63** (2009) 189–285, arXiv:0901.0002 [hep-ph].

[33] S. Catani, G. Ferrera, and M. Grazzini, "W boson production at hadron colliders: the lepton charge asymmetry in NNLO QCD," *JHEP* **05** (2010) 006, arXiv:1002.3115 [hep-ph].

[34] C. P. O. . J. 2011), "*CERN announces LHC to run in 2012.*" http://press.web.cern.ch/press/PressReleases/Releases2011/PR01.11E.html.

[35] **ATLAS** Collaboration, G. Aad *et al.*, "The ATLAS Experiment at the CERN Large Hadron Collider," *JINST* **3** (2008) S08003.

[36] **ATLAS** Collaboration, A. Airapetian *et al.*, "ATLAS calorimeter performance,". CERN-LHCC-96-40.

[37] **ATLAS Collaboration** Collaboration, G. Aad *et al.*, "Readiness of the ATLAS Liquid Argon Calorimeter for LHC Collisions," *Eur.Phys.J.* **C70** (2010) 723–753, arXiv:0912.2642 [physics.ins-det].

[38] **ATLAS Collaboration** Collaboration, "ATLAS first level trigger: Technical design report,".

[39] **ATLAS Collaboration** Collaboration, "ATLAS high-level trigger, data acquisition and controls: Technical design report,".

[40] **The ATLAS** Collaboration, G. Aad *et al.*, "Atlas public results,". https://twiki.cern.ch/twiki/bin/view/AtlasPublic/WebHome.

[41] **ATLAS** Collaboration, "Updated luminosity determination in pp collisions at $\sqrt{s} = 7$ tev using the atlas detector," Tech. Rep. ATLAS-CONF-2011-011, CERN, Geneva, Mar, 2011.

[42] ATLAS, "Luminosity determination in pp collisions at $\sqrt{s} = 7$ tev using the atlas detector at the lhc," *The European Physical Journal C -*

Particles and Fields **71** (2011) 1–37. http://dx.doi.org/10.1140/epjc/s10052-011-1630-5. 10.1140/epjc/s10052-011-1630-5.

[43] A. P. Group, "*Data Periods.*" https://twiki.cern.ch/twiki/bin/viewauth/AtlasProtected/DataPeriods#2010_Data_Periods_for_pp_running.

[44] E. group, "Good run lists recomenndations." https://svnweb.cern.ch/cern/wsvn/atlasgrp/Physics/StandardModel/WZPhysics/Common/GRL/#path_Physics_StandardModel_WZPhysics_Common_GRL_.

[45] S. Jadach, J. H. Kuhn, and Z. Was, "TAUOLA: A library of Monte Carlo programs to simulate decays of polarized tau leptons," *Comput. Phys. Commun.* **64** (1990) 275–299.

[46] M. Jezabek, Z. Was, S. Jadach, and J. H. Kuhn, "The tau decay library TAUOLA, update with exact O(alpha) QED corrections in tau $\to$ mu. (e) neutrino anti-neutrino decay modes," *Comput. Phys. Commun.* **70** (1992) 69–76.

[47] S. Jadach, Z. Was, R. Decker, and J. H. Kuhn, "The tau decay library TAUOLA: Version 2.4," *Comput. Phys. Commun.* **76** (1993) 361–380.

[48] Z. Was, "TAUOLA, TAUOLA universal interface PHOTOS and MC-TESTER: Status Report," *Nucl. Phys. Proc. Suppl.* **189** (2009) 43–48.

[49] N. Davidson, G. Nanava, T. Przedzinski, E. Richter-Was, and Z. Was, "Universal interface of tauola technical and physics documentation," Tech. Rep. arXiv:1002.0543. IFJPAN-IV-2009-10, Feb, 2010. Comments: 1+44 pages, 17 eps figures.

[50] J. M. Butterworth, J. R. Forshaw, and M. H. Seymour, "Multiparton interactions in photoproduction at HERA," *Z. Phys.* **C72** (1996) 637–646. See `http://projects.hepforge.org/jimmy/`.

[51] P. Golonka and Z. Was, "PHOTOS Monte Carlo: A Precision tool for QED corrections in Z and W decays," *Eur.Phys.J.* **C45** (2006) 97–107, `arXiv:hep-ph/0506026 [hep-ph]`.

[52] N. Davidson, Z. Was, and J. Kretzschmar, "Validation of the Athena PHOTOS interface to PYTHIA/Herwig/MC@NLO using MC-TESTER." Talk, September, 2009. MC Generator Meeting, `http://indico.cern.ch/getFile.py/access?contribId=1&resId=0&materialId=slides&confId=68579`.

[53] P. Golonka and Z. Was, "Next to leading logarithms and the PHOTOS Monte Carlo," *Eur. Phys. J.* **C50** (2007) 53–62.

[54] E. Barberio, B. van Eijk, and Z. Was, "PHOTOS: A universal Monte Carlo for QED radiative corrections in decays," *Comput. Phys. Commun.* **66** (1991) 115–128.

[55] E. Barberio and Z. Was, "PHOTOS: A universal Monte Carlo for QED radiative corrections. Version 2.0," *Comput. Phys. Commun.* **79** (1994) 291–308.

[56] B. P. Kersevan and E. R. Was., "Processing generated events with tauola and photos using the athena interface:." `http://atlas-sw.cern.ch/cgi-bin/viewcvs-atlas.cgi/offline/Generators/Tauola_i/doc/athena_TauolaPhotos.ps?revision=1.4`.

[57] **GEANT4** Collaboration, S. Agostinelli *et al.*, "GEANT4: A simulation toolkit," *Nucl. Instrum. Meth.* **A506** (2003) 250–303.

[58] **ATLAS** Collaboration, G. Aad *et al.*, "The ATLAS Simulation Infrastructure," *Eur. Phys. J.* **C70** (2010) 823–874, arXiv:1005.4568 [physics.ins-det].

[59] K. Melnikov and F. Petriello, "Electroweak gauge boson production at hadron colliders through $\mathcal{O}(\alpha_s^2)$," *Phys. Rev.* **D74** (2006) 114017, arXiv:hep-ph/0609070.

[60] K. Melnikov and F. Petriello, "The W boson production cross section at the LHC through $\mathcal{O}(\alpha_s^2)$," *Phys. Rev. Lett.* **96** (2006) 231803.

[61] R. Gavin, Y. Li, F. Petriello, and S. Quackenbush, "FEWZ 2.0: A code for hadronic Z production at next-to-next-to-leading order," *Comput.Phys.Commun.* **182** (2011) 2388–2403, arXiv:1011.3540 [hep-ph]. FEWZ pre-released V2.1.

[62] J. Butterworth, E. Dobson, U. Klein, B. Mellado Garcia, T. Nunnemann, J. Qian, D. Rebuzzi, and R. Tanaka, "Single boson and diboson production cross sections in pp collisions at sqrts=7 tev," Tech. Rep. ATL-COM-PHYS-2010-695, CERN, Geneva, Aug, 2010.

[63] **Atlas Collaboration** Collaboration, G. Aad *et al.*, "*Measurement of the* $W \to l\nu$ *and* $Z/\gamma^* \to ll$ *production cross-sections in proton-proton collisions at* $\sqrt{s} = 7$ TeV *with the ATLAS Detector*," *JHEP* **1012** (2010) 060, arXiv:1010.2130 [hep-ex].

[64] M. Dobbs, S. Frixione, E. Laenen, K. Tollefson, H. Baer, *et al.*, "Les Houches guidebook to Monte Carlo generators for hadron collider physics," arXiv:hep-ph/0403045 [hep-ph].

[65] J. M. Campbell, J. Huston, and W. Stirling, "Hard Interactions of Quarks and Gluons: A Primer for LHC Physics," *Rept.Prog.Phys.* **70** (2007) 89, arXiv:hep-ph/0611148 [hep-ph].

[66] **Particle Data Group** Collaboration, K. Nakamura *et al.*, "Review of particle physics," *J. Phys.* **G37** (2010) 075021.

[67] T. Sjostrand, S. Mrenna, and P. Z. Skands, "PYTHIA 6.4 Physics and Manual," *JHEP* **05** (2006) 026, arXiv:hep-ph/0603175. http://projects.hepforge.org/pythia6/.

[68] R. Bonciani, S. Catani, M. L. Mangano, and P. Nason, "NLL resummation of the heavy-quark hadroproduction cross- section," *Nucl. Phys.* **B529** (1998) 424–450, arXiv:hep-ph/9801375.

[69] S. Moch and P. Uwer, "Theoretical status and prospects for top-quark pair production at hadron colliders," *Phys. Rev.* **D78** (2008) 034003, arXiv:0804.1476 [hep-ph].

[70] M. Beneke, M. Czakon, P. Falgari, A. Mitov, and C. Schwinn, "Threshold expansion of the $gg(q\bar{q}) \to q\bar{Q} + x$ cross section at order α_s^4," *Phys. Lett.* **B690** (2010) 483–490, arXiv:0911.5166 [hep-ph].

[71] G. Corcella *et al.*, "HERWIG 6.5: an event generator for Hadron Emission Reactions With Interfering Gluons (including supersymmetric processes)," *JHEP* **01** (2001) 010, arXiv:hep-ph/0011363.

[72] "Performance of primary vertex reconstruction in proton-proton collisions at $\sqrt{s}$ =7 tev in the atlas experiment," Tech. Rep. ATLAS-CONF-2010-069, CERN, Geneva, Jul, 2010.

[73] **The ATLAS** Collaboration, "*Electron and photon reconstruction and identification in ATLAS: expected performance at high energy and results at* $\sqrt{s} = 900$ GeV," Tech. Rep. ATLAS-CONF-2010-005, CERN, Geneva, Jun, 2010.

[74] **The ATLAS** Collaboration, G. Aad *et al.*, "Expected performance of the ATLAS experiment - detector, trigger and physics," `arXiv:0901.0512 [hep-ex]`.

[75] "Expected electron performance in the atlas experiment," Tech. Rep. ATL-PHYS-PUB-2011-006, CERN, Geneva, Apr, 2011.

[76] W. Lampl *et al.*, "Calorimeter clustering algorithms: Description and performance," `ATL-LARG-PUB-2008-002`.

[77] T. Barillari *et al.*, "Local hadronic calibration,".

[78] E. group, "Electrons energy direction." `https://twiki.cern.ch/twiki/bin/view/AtlasProtected/ElectronsEnergyDirection`.

[79] J. group, "How to clean jets." `https://twiki.cern.ch/twiki/bin/view/AtlasProtected/HowToCleanJets`.

[80] "Data-quality requirements and event cleaning for jets and missing transverse energy reconstruction with the atlas detector in proton-proton collisions at a center-of-mass energy of *sqrts* = 7 tev," Tech. Rep. ATLAS-CONF-2010-038, CERN, Geneva, Jul, 2010.

[81] S. Migas. PhD thesis, University of Liverpool (in preparation).

[82] **The ATLAS** Collaboration, G. Aad *et al.*, "Electron efficiency measurements using ATLAS 2010 data at $\sqrt{s} = 7$ TeV: Supporting note for the 2010 egamma paper." ATL-COM-PHYS-2011-322, Mar, 2011.

[83] J. T. Childers, R. Stamen, A. Tricoli, and M. Wielers, "Performance of the Electron and Photon Trigger in pp Collisions at sqrt(s) = 7 TeV," Tech. Rep. ATL-COM-DAQ-2011-008, CERN, Geneva, Jan, 2011.

[84] **ATLAS Collaboration** Collaboration, G. Aad *et al.*, "Electron performance measurements with the ATLAS detector using the 2010 LHC proton-proton collision data," *Eur.Phys.J.* **C72** (2012) 1909, arXiv:1110.3174 [hep-ex].

[85] E. group, "*Official electron efficiencies and scale factor recommendation.*" https://twiki.cern.ch/twiki/bin/viewauth/AtlasProtected/EfficiencyMeasurements.

[86] E. group, "*Official electron energy scale and resolution corrections recommendation.*" https://twiki.cern.ch/twiki/bin/view/AtlasProtected/EnergyScaleResolutionRecommendations.

[87] **The ATLAS** Collaboration, G. Aad *et al.*, "Studies of the performance of the ATLAS detector using cosmic-ray muons," *Eur.Phys.J.* **C71** (2011) 1593, arXiv:1011.6665 [physics.ins-det].

[88] S. Whitehead, P. H. Beauchemin, and K. Lohwasser, "*"Etmiss vs Iso" method to determine QCD background to Wenu events*," Tech. Rep. ATL-COM-PHYS-2010-287, CERN, Geneva, May, 2010.

[89] **The ATLAS** Collaboration, "*Evidence for prompt photon production in p p collisions at* $\sqrt{s} = 7$ TeV *with the ATLAS detector*," Tech. Rep. ATLAS-CONF-2010-077, CERN, Geneva, Jul, 2010.

[90] M. Aharrouche *et al.*, "W $\to l\nu$ *and* Z $\to ll$ *cross-sections measurements in proton-proton collisions at* $\sqrt{s} = 7$ TeV *with the ATLAS Detector*," Tech. Rep. ATL-COM-PHYS-2011-178, CERN, Geneva, Feb, 2011.

[91] **The ATLAS** Collaboration, "*Measurement of the production cross section of* $W\gamma$ *and* $Z\gamma$ *production in proton-proton collisions at* $\sqrt{s} = 7$ TeV *with the ATLAS Detector*,". [hep-ex].

[92] **The ATLAS** Collaboration, "*Background Estimation for Inclusive SUSY Searches - The Tiles Method*," Tech. Rep. ATL-PHYS-PUB-2009-077. ATL-COM-PHYS-2009-250, CERN, Geneva, May, 2009.

[93] J. Hartert and I. Ludwig, "*Electron isolation in the ATLAS experiment*," Tech. Rep. ATL-PHYS-INT-2010-052, CERN, Geneva, May, 2010. ATL-PHYS-INT-2010-052.

[94] **The ATLAS** Collaboration, G. Aad *et al.*, "Measurement of the $W \to \tau\nu_\tau$ cross section in pp collisions at $\sqrt{s} = 7$ tev with the atlas experiment. oai:cds.cern.ch:1382039,". Comments: 8 pages (20 including author list), 10 figures, 4 tables, submitted to Phys. Lett. B.

[95] A. Sherstnev and R. S. Thorne, "Parton Distributions for LO Generators," *Eur. Phys. J.* **C55** (2008) 553–575, `arXiv:0711.2473 [hep-ph]`.

[96] "Measurement of the $W \to \ell\nu$ and $Z/\gamma^* \to \ell\ell$ production cross sections in proton-proton collisions at $\sqrt{s} = 7$ TeV with the ATLAS detector," *JHEP* **12** (2010) 060, `arXiv:1010.2130 [hep-ex]`.

[97] Q. Buat, F. Polci, and R. Ishmukhametov, "*Systematic uncertainties for dead OTX cut.*" `https://indico.cern.ch/getFile.py/access?contribId=6&resId=0&materialId=slides&confId=116188`.

[98] M. Aharrouche *et al.*, "Total and differential $W \to \ell\nu$ and $Z \to \ell\ell$ cross-sections measurements in proton-proton collisions at $\sqrt{s} = 7$ tev with the atlas detector," Tech. Rep. ATL-COM-PHYS-2011-751, CERN, Geneva, Jun, 2011.

[99] S. Alekhin, J. Blumlein, S. Klein, and S. Moch, "The 3-, 4-, and 5-flavor NNLO Parton from Deep-Inelastic- Scattering Data and at Hadron Colliders," *Phys. Rev.* **D81** (2010) 014032, `arXiv:0908.2766 [hep-ph]`.

[100] S. Alekhin, J. Blumlein, and S.-O. Moch, "Update of the NNLO PDFs in the 3-, 4-, and 5-flavour scheme," *PoS* **DIS2010** (2010) 021, arXiv:1007.3657 [hep-ph].

[101] **H1 and ZEUS** Collaboration, V. Radescu, "Hera Precision Measurements and Impact for LHC Predictions," arXiv:1107.4193 [hep-ex]. H1prelim-11-042, ZEUS-prel-11-002, Proceedings of Moriond 2011.

[102] P. Jimenez-Delgado and E. Reya, "Dynamical NNLO parton distributions," *Phys. Rev.* **D79** (2009) 074023, arXiv:0810.4274 [hep-ph].

[103] S. Catani and M. Grazzini, "An NNLO subtraction formalism in hadron collisions and its application to Higgs boson production at the LHC," *Phys. Rev. Lett.* **98** (2007) 222002, arXiv:hep-ph/0703012.

[104] S. Catani, L. Cieri, G. Ferrera, D. de Florian, and M. Grazzini, "Vector boson production at hadron colliders: A Fully exclusive QCD calculation at NNLO," *PRLTA* **103** (2009) 082001, arXiv:0903.2120 [hep-ph]. DYNNLO version 1.1.

[105] "Roofit." http://root.cern.ch/root/html/RooEllipse.html.

List of Figures

List of Tables